DOPAMINERGIC REGULATION OF INSULIN SECRETION INVESTIGATED BY FLUORESCENCE FLUCTUATION SPECTROSCOPY

by

Brittany Catherine Caldwell

Dissertation

Submitted to the Faculty of the

Graduate School of Vanderbilt University

in partial fulfillment of the requirements

for the degree of

DOCTOR OF PHILOSOPHY

in

Biomedical Engineering

May, 2016

Nashville, Tennessee

Approved by:

Professor David Piston

Professor Melissa Skala

Professor John Gore

Professor Hassane Mchaourab

Professor Anne Kenworthy

ACKNOWLEDGEMENTS

I am very thankful to my advisor, Dave Piston, who provided me with challenging problems to solve and the methods with which to solve them. Going to the lab even on a challenging day was exciting with the lab environment Dave created. My committee members, Melissa Skala, John Gore, Hassane Mchaourab, and Anne Kenworthy provided me with excellent feedback that helped develop and strengthen my project. I am grateful for their time and patience.

Working in the Piston Lab was a wonderful experience. I am thankful for all the current and previous lab members who made the lab a fun place to go each day. I owe most of my molecular biology knowledge to Alessandro Ustione who is a fantastic mentor and wonderful friend. I also want to thank Amy Elliott, Chris Reissaus, Troy Hutchens, and Zeno Lavagnino who provided helpful feedback and many laughs during my time in the Piston Lab.

I am blessed with four parents who have supported me on this journey. Most importantly though, I must thank my mother who has always encouraged education, not just by words, but also by example. One of my earliest memories is dragging my children's books over to the dining table where I watched her study so that I could be like her. Mom, without your influence, I would most certainly would not be where I am today. Thank you.

Last, I want to thank my husband who has given me infinite support and encouragement on this journey. There are no words to describe how thankful I am for

your support as we lived apart so that I could achieve my goals. This accomplishment would not have been possible without you. Thank you.

Table of Contents

LIST OF FIGURES

Figure Page

LIST OF TABLES

Table Page

CHAPTER 1

PHYSIOLOGY INTRODUCTION

Introductory Comments

This dissertation investigates the protein signaling chain in the dopamine-mediated negative feedback pathway of pancreatic β cells. In the presence of dopamine, a reduction in the influx of calcium occurs, mediating the inhibition of glucose stimulated insulin secretion. The signaling cascade that occurs after stimulation of the dopamine receptor, causing calcium channels to close, is currently unknown; however, it can be hypothesized from other dopamine receptor pathways which signal through the Gβγ complex to activate G-protein coupled inwardly-rectifying potassium channels (GIRK). GIRK activation causes the membrane to become hyperpolarized which causes voltage gated calcium channels to close. I hypothesize that activation of GIRK, through the Gβγ complex, occurs after stimulation of the dopamine receptor in β cells. To test this hypothesis, I measured protein interactions with fluorescence fluctuation spectroscopy (FFS). FFS is a single molecule imaging technique capable of detecting diffusion rates and heteromerization between proteins. This first chapter introduces the anatomical and physiological background essential to understanding the biological question.

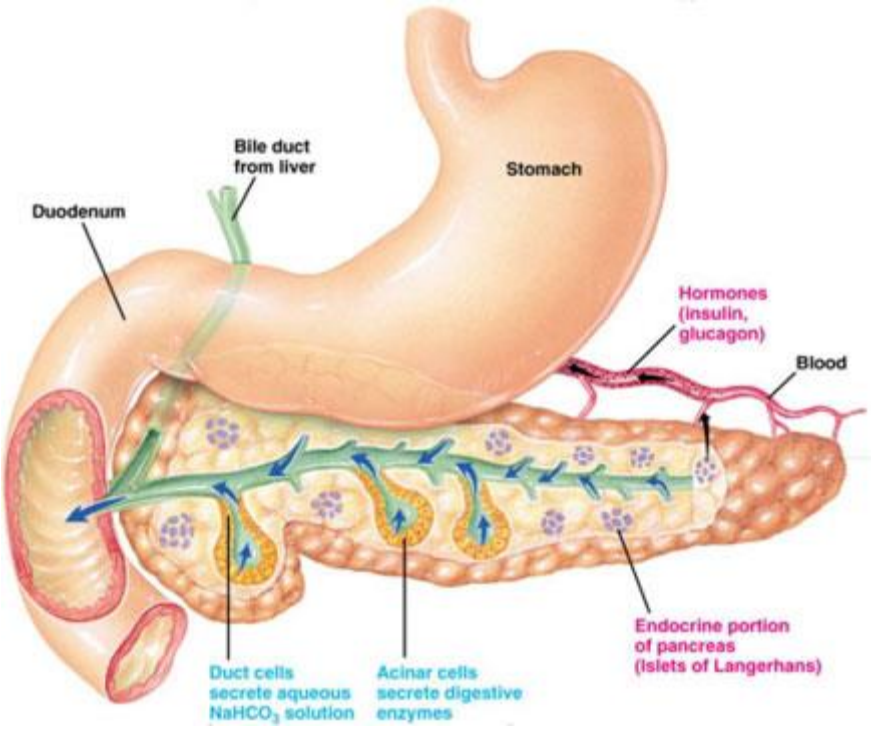

Figure 1 Anatomy of pancreas and its relation to duodenum and arteries. (from (1)**)**

Physiology of Endocrine Pancreas

Pancreas Physiology

The pancreas is an organ located behind the stomach, with a portion touching the first part of the small intestine, or duodenum as illustrated in figure 1. It performs two main functions, aiding digestion and regulating blood glucose (2–5). While one organ, the pancreas is made up of two portions, an exocrine and an endocrine portion. The exocrine pancreas, 95% of the pancreas, produces enzymes which aid in digestion, such as proteases to digest proteins, amylase to digest sugars, and lipase to digest fat (6). These digestive enzymes are released into ducts which join to form the pancreatic duct and then onto the ampulla of Vater which releases the digestive enzymes into the duodenum (2, 3). The endocrine pancreas is composed of small micro-organs called

islets of Langerhans. The cells composing the islets are responsible for the production and secretion of hormones by the pancreas, including insulin and glucagon. The islets of Langerhans, while dispersed throughout the pancreas, are highly vascularized allowing for efficient release of hormones into the arteries (7).

Islets of Langerhans

The Islets of Langerhans, hereafter referred to as islets, are micro-organs consisting of α, β, δ, and pancreatic polypeptide (also labeled γ cells), and ε cells (8). These cells produce and secrete glucagon, insulin, somatostatin, pancreatic polypeptide hormone, and ghrelin, respectively, into the bloodstream. While their specific cell functions are conserved, the makeup and distribution of each cell type of murine and human islets differ. Murine islets, commonly used for lab studies, are composed of roughly 80% β, 15% α cells and less than 5% of δ, γ, and ε cells (9, 10). They are formed by a central cluster of β cells surrounded by a layer of α and δ cells (11). In comparison, human islets are composed of roughly 60% β cells, 30% α cells, and 10% of δ, γ, and ε cells (12, 13). Previously, it was thought that these cell types were distributed homogenously throughout the islet; however, the current structure, accepted by the community, is more complex. A human islet is now considered to be structured as a cluster of small cell groupings, each of which is composed of a collection of β, α, δ, γ, and ε cells. Thus, together these small clusters of islet cell groupings form the whole human islet (10, 14)The differing cell compositions are seen after staining an islet for glucagon (α cells), insulin (β cells), and somatostatin (δ cells) as shown in figure 2. In addition to composition, human and mouse islets differ also in their size; a human islet is 50 ± 29 μm in diameter versus a wild-type mouse islet which measures 116 ± 80 μm

(10). While murine and human islets do have differences, they are similar in how they regulate blood glucose homeostasis (10)

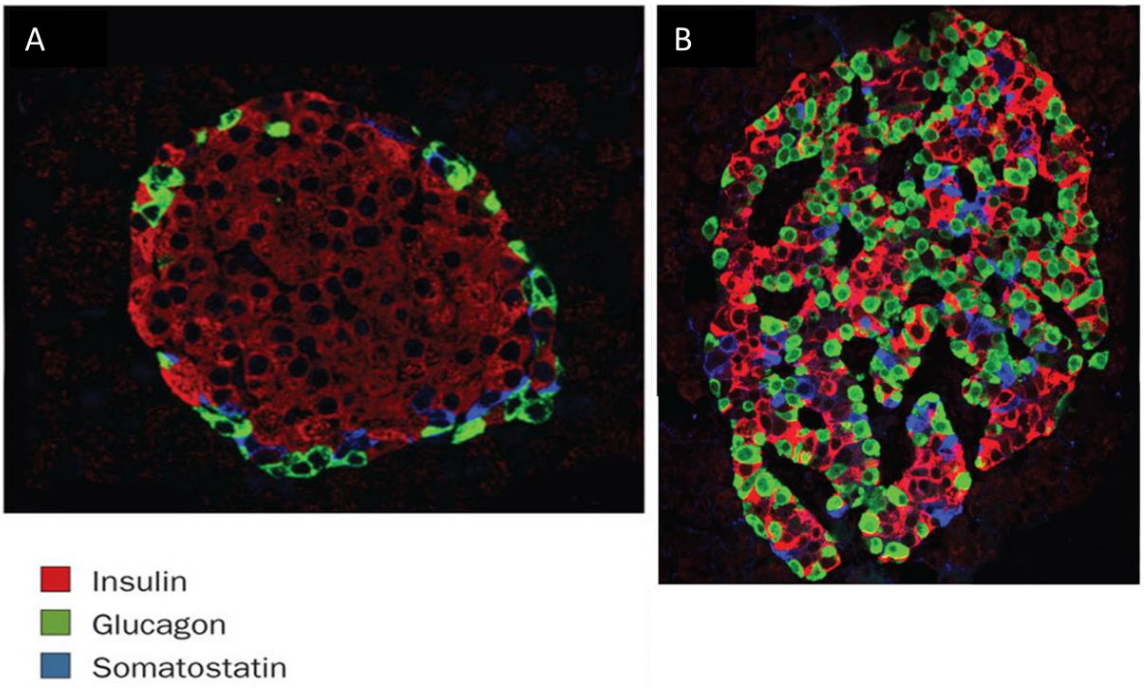

Figure 2 Insulin, glucagon, and somatostatin staining of islet from mouse (A) and human (B). In the mouse islet, a β-cell core is surrounded by α and δ cells. In contrast, the human islet is composed of small clusters of cells grouped together to form the larger islet. (from (11)**)**

The importance of islet structure is further seen when cell to cell communication is disrupted, via gap junctions. Gap junctions are small channels between cells which allow the passing of small molecules and ions. Through gap junctions, cells are able to equilibrate membrane potential between neighboring cells. Studies performed on intracellular calcium levels show islets have an oscillatory response pattern in response to high glucose. To achieve a complex response pattern like this requires high levels of coordination (15). The loss of connexin 36, a gap junction protein found in islets,

disrupts the oscillatory response (16–19). The importance of islet architecture is additionally shown when islet cells are dispersed changing the amount of insulin and glucagon secreted compared to whole islets (9, 20–22).

In the pancreas, islets are highly vascularized with separate capillaries for endocrine and exocrine functions (7). Endocrine capillaries have thin walls and over 70% more fenestrae in the capillary walls than exocrine capillaries, facilitating rapid molecule exchange (7). Additionally, islets are highly innervated by parasympathetic, sympathetic, and sensory nerves (9, 10, 23). Parasympathetic stimulation increases the secretion of insulin, glucagon, somatostatin, and pancreatic polypeptide from islet cells (23–28). For example, parasympathetic nerve stimulation is responsible for the steep increase in insulin at the start of a meal. Thus, insulin can be increased before an increase in blood glucose is detectable. Parasympathetic nerves have likewise been shown to control glucagon secretion during hypoglycemia (29–31). In contrast to parasympathetic stimulation, sympathetic neurons also control islet function by inhibiting insulin secretion and stimulating glucagon secretion. For example, norepinephrine is known to block insulin secretion and activate glucagon secretion (23, 30, 32). Furthermore, the neuropeptides released from neurons can directly activate G-protein coupled receptors (GPCRs) on the membrane. Acetylcholine, for instance, stimulates β cells to secrete insulin by directly activating the muscarinic acetylcholine receptors (23). Neural stimulation provides a secondary regulation of islet secretion to tightly control islet functions beyond blood glucose levels.

Blood Glucose Regulation

After a meal, blood glucose increases stimulating pancreatic β cells to secrete insulin. The presence of insulin causes cell tissues including adipose, muscle, and liver to uptake glucose in order to lower blood glucose levels (33, 34). In periods of starvation, or low blood glucose, pancreatic α cells secrete glucagon into the bloodstream. Glucagon acts mainly on the liver to stimulate glycogenolysis, the breakdown of glycogen to glucose. Increased production of glucose returns blood glucose to normal levels (33–35). While other factors additionally help regulate insulin and glucagon secretion, blood glucose concentration is the central driver illustrated in figure 3. Blood glucose severely below normal, hypoglycemia, and severely above normal, hyperglycemia, are severe health concerns (34). Through the secretion of insulin and glucagon, the body is able to achieve a narrow range of glucose in the bloodstream.

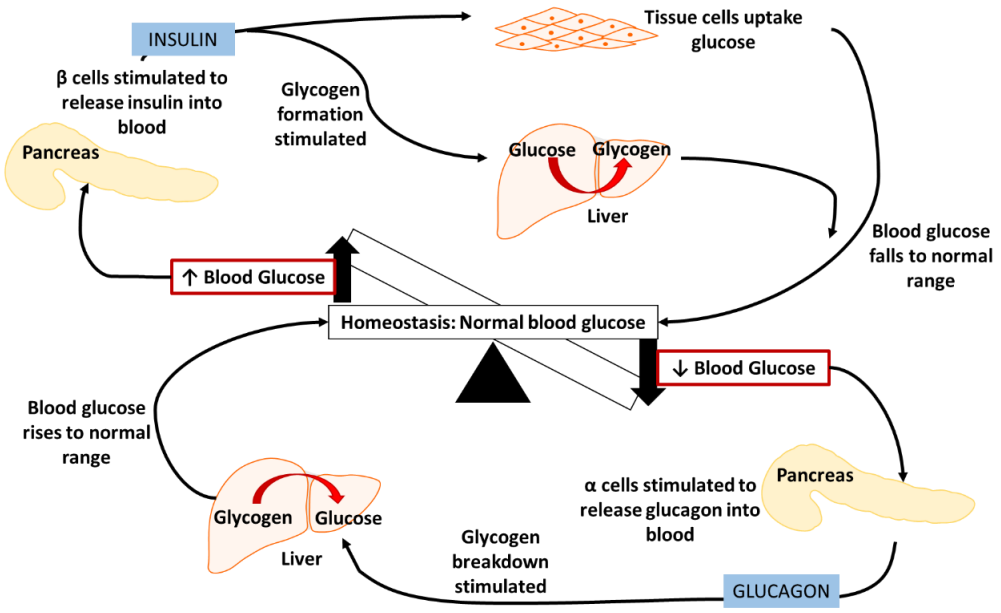

Figure 3 Diagram showing blood glucose regulation. Adapted from Pearson Education, Inc. 2004

Insulin and glucagon do not work independently; but concurrently to achieve normal blood glucose levels. To achieve glucose homeostasis faster after a meal, insulin secretion is increased and glucagon secretion is decreased. Conversely, during starvation glucagon secretion is increased and insulin secretion is decreased. Figure 4 shows the levels of insulin and glucagon in the plasma and their effect on blood glucose levels after a meal. As blood glucose rises the amount of insulin secreted also increases, followed shortly thereafter by a decrease in glucagon secretion. Both the increase in insulin and decrease in glucagon allow the body to finely regulate the amount of glucose taken into the tissue. Thus, too much glucose taken into the tissue, resulting in hypoglycemia, does not occur. As blood glucose begins to decrease, insulin and glucagon return to their resting levels (36).

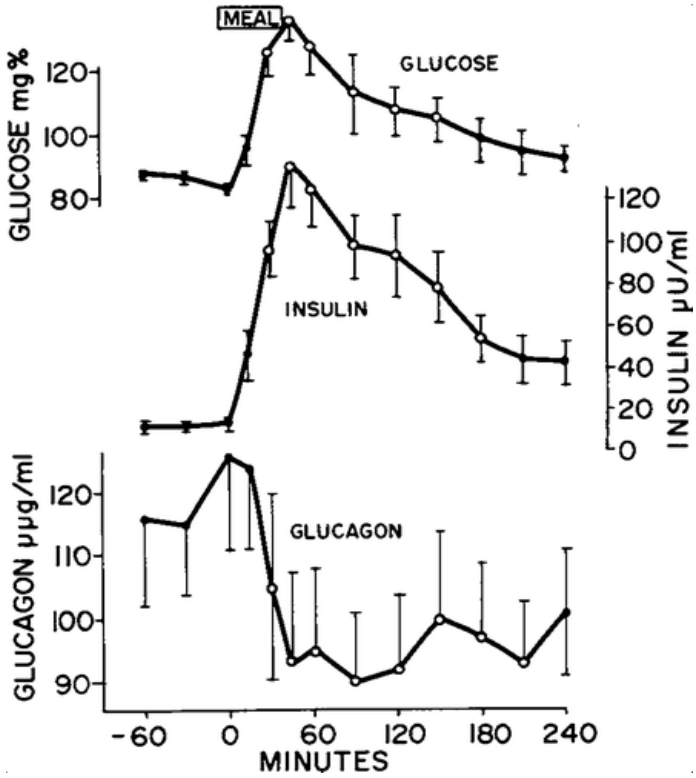

Figure 4 Plasma glucose, insulin, and glucagon levels after a meal. (from (36)**)**

Diabetes Mellitus

Diabetes Mellitus is characterized by chronic hyperglycemia, or high blood glucose. The name diabetes mellitus comes from syphon and sweet, noting the large amount of urination and high concentration of sugar in the urine of those with uncontrolled diabetes (2). Traditionally, diabetes has been divided into two broad classes, which are often thought of as different diseases as they are the result of different causes (2, 37).

Type 1

Type 1 diabetes mellitus (T1DM) is a chronic autoimmune disorder where the body attacks β cells, destroying insulin production (37, 38). T1DM is most often diagnosed in children and young adults and is therefore often termed juvenile-onset diabetes although diagnosis can be at any age (37, 38). Since the body's sensitivity to insulin is unchanged in T1DM, exogenous insulin is used to manage blood glucose levels (32).

Type 2

In contrast to T1DM, type 2 diabetes mellitus (T2DM) is a chronic metabolic disorder characterized by insensitivity to insulin due to insulin resistance (39, 40). While not always the reason, increased caloric intake and decreased exercise, together, are the leading cause of insulin resistance. To compensate for the body becoming resistant to insulin, β cells begin to overproduce insulin to try to maintain normal blood glucose levels resulting in hyperinsulinemia. Continued stress on the β cells trying to produce large amounts of insulin leads to exhaustion and eventually β cell death (39, 41, 42).

The combination of decreased insulin sensitivity and insufficient production of insulin results in chronic hyperglycemia or T2DM.

Treating T2DM with insulin alone is sub-optimal as the body is insulin resistant. Therefore, one of the most effective therapies is weight loss and a reduced carbohydrate diet (40). Additionally, both oral and injectable pharmacological therapies have been developed to help manage T2DM. Meglitinides and sulfonylureas work by stimulating the release of insulin and are therefore often taken prior to meals (43). Thiazolidinediones work by improving the body's sensitivity to insulin in muscle and fat tissue and like biguanides (Metaformin) also decrease the amount of glucose produced by the liver (43, 44). Dipeptidyl-peptidase 4 (DPP-4) inhibitors work by inhibiting the breakdown of incretins which in turn stimulates the release of insulin and inhibits the release of glucose from the liver (45). Furthermore, alpha-glucosidase inhibitors reduce the breakdown of starches and sugars while sodium glucose transporter 2 (SGLT2) inhibitors block glucose from bring reabsorbed in the kidneys (46, 47). Last, amylin mimetics and incretin mimetics can be injected into the body to stimulate the release of insulin. While the list of treatments for T2DM is lengthy, each of these treatments is not without side effects and only serve to manage blood glucose levels, not treat the disease. Thus, further understanding of insulin regulation leading to better T2DM treatments is desirable.

G Protein Coupled Receptor Regulation of Insulin

Introduction

G protein-coupled receptors (GPCR) are the largest family of membrane proteins with over 800 GPCR sequences being found in the human genome (48). Their function is to transmit signals outside the cell inwards so that the cell may respond appropriately (49). Due to their ability to transmit signals into the cell, GPCRs are targeted for many therapeutics in a variety of ailments (50). It is estimated that fifty percent of current clinical drugs target a GPCR (51, 52). The ligands of GPCRs vary broadly, including ions, odorants, peptides and proteins, lipids, organic molecules (nucleotides, amines, fatty acids), and photons (48, 53). Just as varied as their ligands, the functions of GPCRs range from embryonic development, memory, vision, taste, and energy homeostasis to name a few (8, 54). Due to their diversity, two main classification systems exist. One methodology is the GRAFS system which groups receptors by a phylogenetic system: rhodopsin, adhesion, frizzled/taste, glutamate, and secretion (48). The second methodology is based on sequence homology and like-function forming 6 classes, A-F: rhodopsin-like, secretion, metabotropic glutamate, fungal mating pheromone, cyclic AMP, and frizzled/smoothened (54).

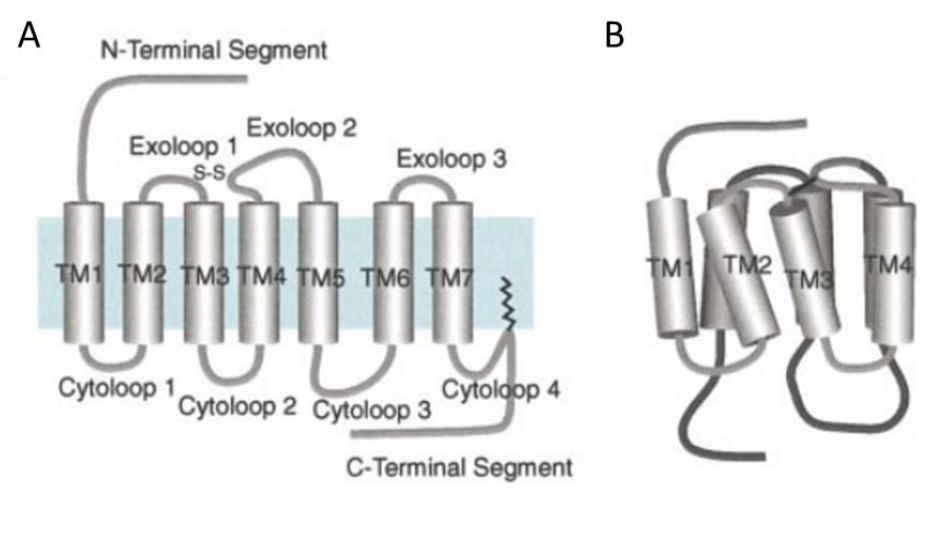

Figure 5 Structure of GPCR (A) folded (B) (from (55)**)**

G Protein-Coupled Receptor Structure

Characterized by their unique structure, GPCRs include seven hydrophobic transmembrane components structured in a counterclockwise arrangement to form a receptor. The transmembrane portions are between 20-28 amino acids and form α helices perpendicular to the membrane (56). The N terminus is located in the extracellular space, while the C terminus is intracellular (57). Three extracellular and three intracellular loops connect the seven transmembrane components as shown in figure 5. The extracellular loops and amino terminus are the most un-conserved sequence in GPCRs, contain glycosylation sites, and serve to control receptor actions (52, 56). A disulfide bond between the cysteines in the second and third extracellular loops promotes folding of the GPCR and regulates binding affinity (56). Conversely, the intracellular loops serve as binding sites for proteins including kinases and scaffolding proteins. The most conserved regions of GPCRs are the second and third intracellular loops which are known to be the binding sites of heterotrimeric G-proteins (58). Upon

the selected ligand binding, a conformational change of the receptor occurs, changing which amino acids can interact with proteins inside the cell (50, 57, 59). For efficient signal transduction, GPCRs exist in a dynamic equilibrium between inactive and active states (50, 59). Activation of the GPCR allows heterotrimeric G-proteins to disassociate where they in turn activate an intracellular signaling cascade.

Heterotrimeric G-Proteins

Furthermore, GPCRs interact with heterotrimeric guanine nucleotide binding proteins, or G-proteins, to signal changes within the cell (48, 58). A heterotrimeric G-protein is formed from three subunits: G_α, G_β, and G_γ. In the inactivate state, the G_α subunit binds to both the GPCR and the G_β subunit. The G_β subunit is then bound to the G_γ subunit which is anchored to the membrane. The $G_{\beta\gamma}$ functions to regulate G_α by increasing the affinity of G_α for GDP. The G_γ subunit additionally serves to enhance the interaction between the G_α subunit and the GPCR. When a ligand binds, a conformational change of the GPCR occurs and a guanosine diphosphate (GDP), bound to the G_α, is exchanged for a guanosine triphosphate (GTP).The bound GTP changes the conformation of the G_α causing it to disassociate from the GPCR and G_β. The GTP-G_α initiates signaling of the cyclic AMP pathway while the G_β and G_γ subunits stay attached as the $G_{\beta\gamma}$ complex and signal to downstream targets, as shown in figure 6 (60, 61).

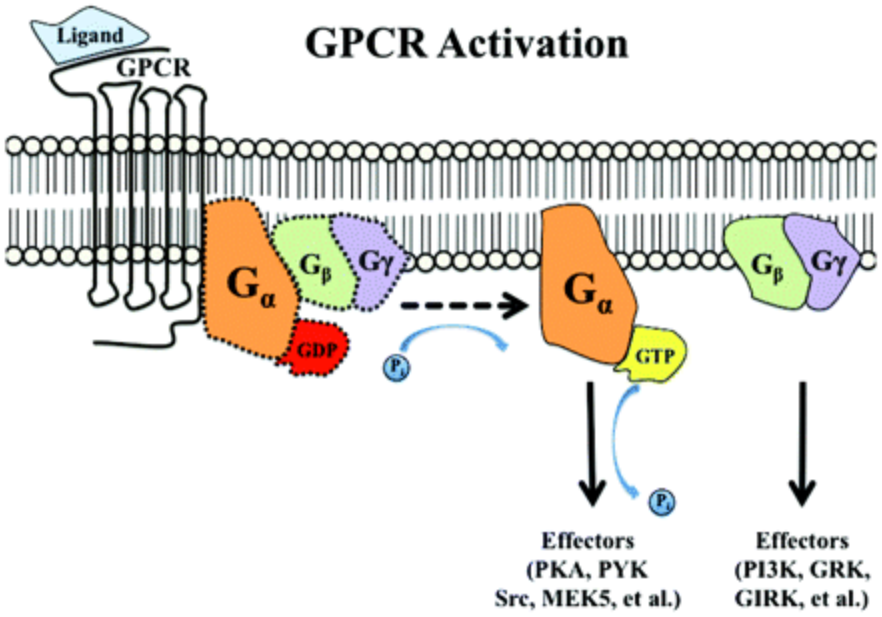

Figure 6 GPCR activation diagram. When a ligand binds, the conformational state of the GPCR changes, causing the conversion of GDP -> GTP and releasing the G_α subunit from the GPCR and $G_{\beta\gamma}$ complex. G_α then signals to downstream target proteins in the cyclic AMP pathway while the Gβγ complex activates a different set of target proteins. (from ((62)**)**

Compared to the large number of GPCRs, there are relatively few G-proteins; 21 G_α subunits, 6 G_β subunits, and 12 G_γ subunits exist in humans (63, 64). Heterotrimeric complexes are often categorized by the sequence of the G_α subunit: $G_{\alpha s}$, $G_{\alpha i}$, $G_{\alpha q}$, and $G_{\alpha 12}$ (63). Post-translational modifications regulate membrane localization and protein-protein interactions (65, 66). The G_β subunit has a propeller structure formed by seven blades wrapped around a central axis as shown in figure 7. The N terminus of the G_β has an alpha-helix which coils with the N terminus of the G_γ subunit. Additionally, the C terminus of the G_γ subunit binds to blades 5 and 6 of G_β (67–69). This unique structure forms a bond between the G_β and G_γ subunits so strong it is broken only by protein denaturing (60). Most of the G_β and G_γ subunits have been shown to couple together and can interact with different G_α subunits (70).

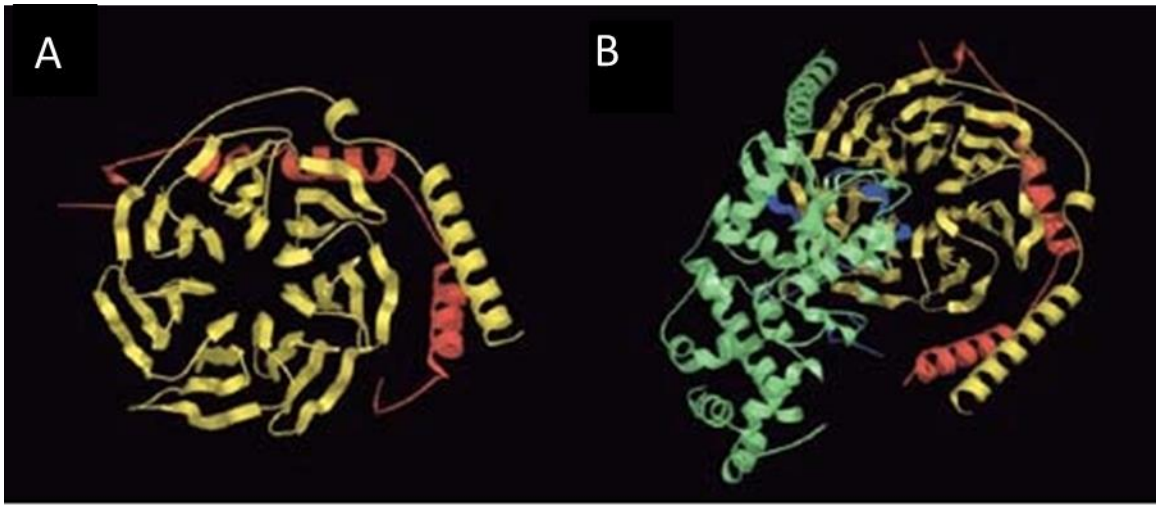

Figure 7 Cartoon of crystalline structure of $G_{\beta 1\gamma 1}$ complex (A). 7 blade propeller structure of G_{β} in yellow with N terminus α helix attached to G_{γ} subunit (red). G_{γ} subunit also bound to blades 5 and 6 of G_{β}. The heterotrimer crystalline structure (B) where G_{α} (green) is bound to the $G_{\beta 1\gamma 1}$ complex with the switch regions (blue) that allow conformational change and the release of the $G_{\beta 1\gamma 1}$ complex. (from (71)**)**

GPCR in Islets (β-cell)

293 non-odorant GPCRs have been found to be expressed in human islets (53). Neurotransmitters, neuropeptides, and other ligands regulate islets by binding to cell surface receptors, oftentimes GPCRs, which then regulate islet functions (53, 72). The effect of many of these GPCRs are still unknown; GPCRs have been shown to have inhibitory and stimulatory effects on the secretion of insulin, glucagon, and somatostatin (53, 72).

Dopamine

Introduction

Dopamine is a neurotransmitter connected to emotional responses and rewards; however, it functions in a variety of signaling pathways (73). Dopamine plays a primary

role in the nigrostriatal (movement), mesolimbic (reward), mesocortical (cognitive control, emotional response), and tuberoinfundibular (lactation) systems of the brain (74–77). Due to its involvement in multiple brain pathways, many disorders have been linked to dopaminergic dysfunctions including schizophrenia, bipolar disorder, Parkinson's disease, post-traumatic stress disorder, autism spectral disorder, alcohol dependency, nicotine dependency, impulsivity and violent behavior, attention deficit hyper disorder, and anxiety (78–90). As drugs to treat these disorders are developed, it is important to target specific receptor types and/or receptors in specific locations and pathways as to not disrupt other dopamine pathways.

The amino acid tyrosine is the precursor to catecholamines, figure 8, which include dopamine, norepinephrine, and epinephrine (91). Tyrosine hydroxylase adds an additional hydroxyl to tyrosine, creating L-Dopa, the predecessor to dopamine. Upon the removal of a carboxylic acid chain by L-Aromatic amino acid decarboxylase, dopamine is formed. Dopamine β-hydroxylase removes a hydroxyl group from dopamine to then form norephinephrine which can then be methylated to form epinephrine by phenylethanolamine N-methyltransferase (91). All three catecholamines are neurotransmitters which are released at axon terminals of nerve cells (2, 92).

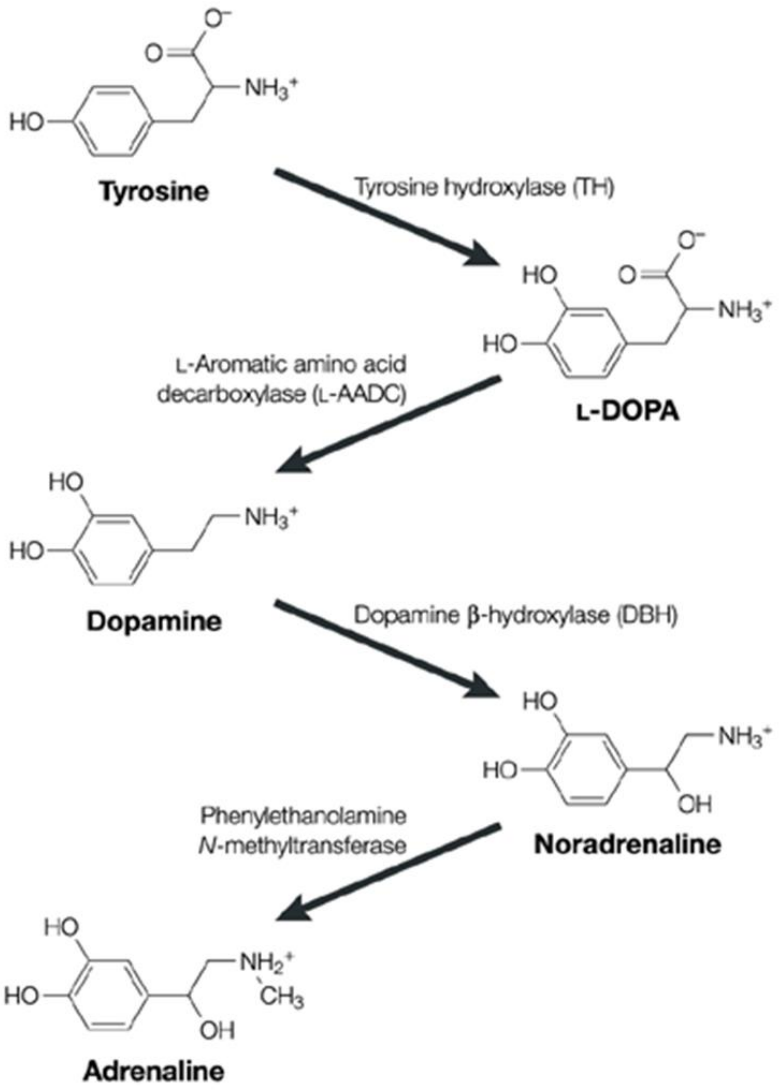

Figure 8 The catecholamine biosynthetic pathway (from (91)**)**

Dopamine Receptors

Dopamine receptors are G-protein coupled receptors separated into two groups, D1-like and D2-like. The D1-like receptors are part of the rhodopsin alpha family and the D2-like are beta-adrenergic receptors (48). The D1-like receptors, D1 and D5, work to regulate adenylyl cyclase activity by increasing cyclic AMP (73). In contrast, the D2-like family, composed of D2, D3, and D4, regulate adenylyl cyclase activity by decreasing

production of intracellular AMP (73). In contrast to the D1-like receptors, D2-like receptors contain introns which provide the ability for splice variants. Six introns are located in the gene encoding the D2 receptor, 5 in the D3 receptor gene, and 3 introns are in the D4 receptor gene (93). Two functional D2 receptors exist, a short ($D2_S$) and a long ($D2_L$) variant due to alternative splicing of the exon between the fourth and fifth introns. The D2 isoforms differ by the presence of an additional 29 amino acids in the third intracellular loop of the $D2_L$ (94). Multiple splice variants exist for the D3 dopamine receptor; however the physiological roles of the variants have yet to be studied (78, 93, 95). Variants due to a 48 base-pair repeat in the third intracellular loop have been reported for the D4 receptor. These receptors are believed to be related to schizophrenia as changes in their affinity for the antipsychotic drug clozapine has been reported (96, 97).

Within the D2-like family, the D2 and D3 receptors have 78% of their genetic code conserved, making it difficult to find a receptor specific agonist/antagonist (98, 99). Differences in the third intracellular loop cause the D3 receptor to have a higher affinity for some agonists compared to the D2 receptor (78, 100). However, due to their similarities, at times both receptors have similar pharmacological properties (78). This is not always the case as it has been shown that activation of the D3 receptor decreases locomotive activity whereas activation of the D2 receptor increases locomotive activity (78). Some currently prescribed drugs for schizophrenia, olanzapine, clozapine, and risperidone have been shown to block both the D2 and D3 receptors, at times causing major side effects (98, 101, 102). While there are newer drugs which block only the D3 receptor in animal models, they haven’t been tested in clinical trials due to their toxicity

(98). The crystalline structure of the D3 dopamine receptor is shown with an agonist in figure 9.

In humans, the D2, D4, and D5 dopamine receptors are expressed in islets (53, 103, 104). Furthermore, the GPR143 receptor, which is activated by the dopamine precursor L-Dopa, has also been shown to be expressed in human islets (53).

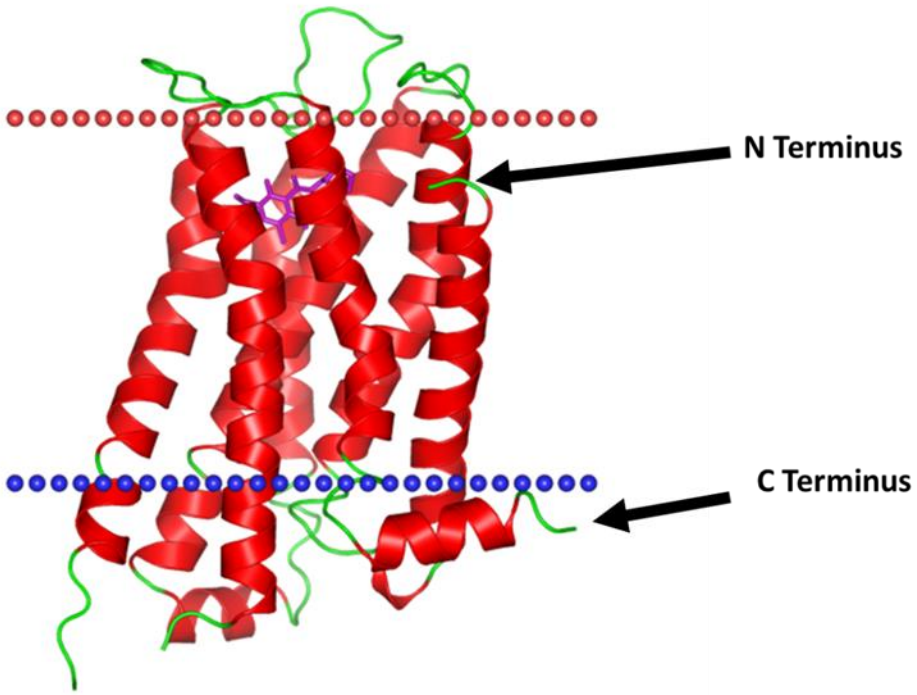

Figure 9 Dopamine D3 receptor crystalline structure with antagonist eticlopride (purple)(from (105)**, Protein Data Bank ID 3pbl)**

Dopamine Mediated Negative Feedback Pathway

Glucose Stimulated Insulin Secretion

In the presence of high glucose, pancreatic β cells secrete insulin into the bloodstream, signaling to tissues to uptake glucose and to the liver to increase glycogen

formation. At the cellular level of the β cell, shown in figure 10, glucose is taken up by glucose transporters (106) and then metabolized by the cell, resulting in an increase in the ATP to ADP ratio. One glucose molecule results in the net production of 36 ATP molecules. ATP sensitive potassium channels (K_{ATP}) close due to the change in the ATP/ADP ratio, depolarizing the membrane (8, 106). The depolarized membrane leads to the opening of L-type voltage gated calcium channels, triggering an increased influx of calcium. The increased intracellular calcium ($[Ca^{2+}]_i$) leads to the fusion of insulin granules to the plasma membrane for exocytosis (8, 106). The amount of glucose taken up by glucose transporters scales to the amount of insulin exocytosed by the β cell (106).

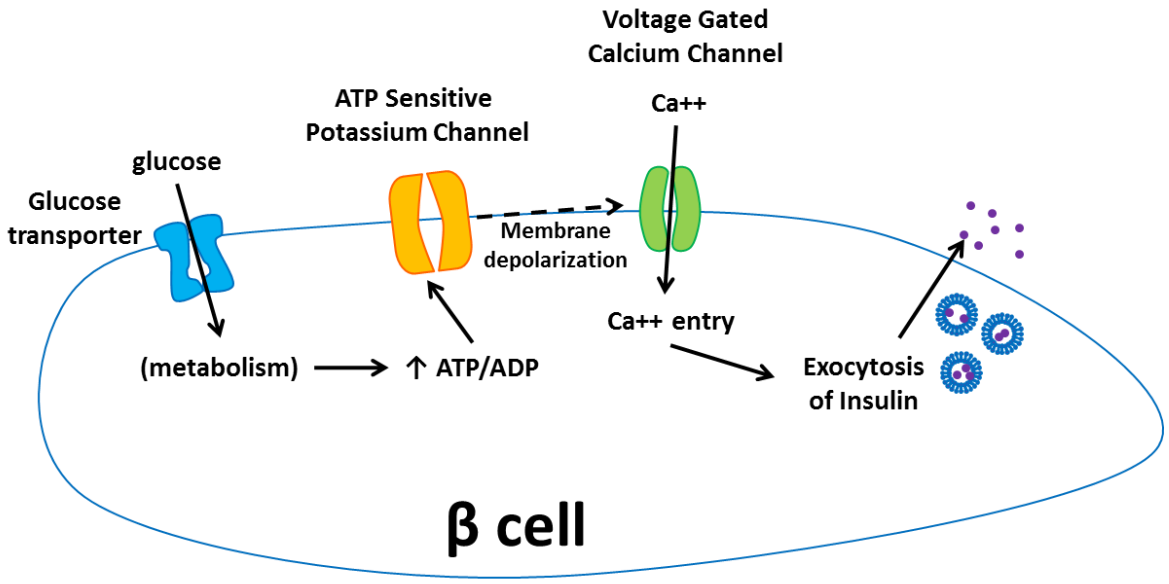

Figure 10 Glucose stimulated insulin secretion (GSIS) pathway.

Dopamine in Islets

In 1963, Falck and Hellman discovered catecholamines in the islets through formaldehyde-induced fluorescence (107). Subsequent studies investigated dopamine

and the actions of other cathecholamines upon islets and insulin secretion; however the results were inconclusive as certain studies showed insulin inhibition while others report increased insulin secretion in the presence of dopamine (108–112). In 1979, Zern et. al, showed that the effect of L-dopa to inhibit insulin secretion was due to the conversion of L-dopa to dopamine (113). Conflicting experiments reported L-dopa itself inhibited insulin secretion while dopamine was contained in secretory granules (114, 115). The origination of the dopamine, if not from the conversion of L-dopa, was not reported No dopaminergic neurons have been shown to innervate islets (4, 23, 24, 31, 116) and dopamine from the brain cannot cross the blood-brain barrier, therefore it was not clear from where this dopamine originated (117). Dopamine circulates in the blood stream, but the concentrations are too low to activate receptors in the islets (117–119). Two recent papers report the inhibition of GSIS in the presence of dopamine, one in mouse and one in human islets, and show that islets convert L-dopa to dopamine (120, 121). Furthermore, both papers report the co-secretion of dopamine and insulin (120, 121). In the human islet study, the authors show the presence of the D2 receptor in β cells and relate the inhibition of GSIS to its stimulation (121). However, in the murine islets studied, it was shown that the D3 dopamine receptor is the modulator of GSIS inhibition and not the D2 receptor, even though the D2 subtype is also present in murine β cells (120). It was further shown that reduced intracellular calcium ($[Ca^{2+}]_i$) oscillations following dopamine stimulation leads to decreased insulin secretion. These combined results support the proposed dopamine mediated negative feedback pathway to regulate insulin secretion which is further studied in this work.

Proposed Dopamine Mediated Negative Feedback Pathway

The published data shows that decreased frequency and amplitude of $[Ca^{2+}]_i$ oscillations inhibits insulin secretion. Thus, we are interested in understanding the molecular signals that connect D3 dopamine receptor activation to the changes in $[Ca^{2+}]_i$. Unpublished work from our lab by Dr. Jacobson and Dr. Ustione, has shown that hyperpolarization after dopamine stimulation results from activation of a potassium channel other than the K_{ATP} channel. We hypothesize dopamine stimulation causes activation of G-protein inwardly rectifying potassium channels (GIRK) by signaling through the $G_{\beta\gamma}$ complex of the G-proteins. In this model, movement of potassium out of the cell would result in plasma membrane hyperpolarization, causing voltage gated calcium channels to close. $[Ca^{2+}]_i$ would thus be reduced in the cell and insulin secretion inhibited. A cartoon representation of GSIS and the proposed dopamine hypothesis is shown in figure 11. Because the islet can synthesize dopamine from L-dopa, dopamine can act as a method of regulating insulin secretion when both are secreted together (120, 121). In this work, I investigated this hypothesis by experiments focused on the heteromerization of the dopamine receptors and $G_{\beta\gamma}$ complex before and after dopamine stimulation. Additionally, I studied the relationship between the $G_{\beta\gamma}$ complex and hypothesized downstream target, GIRK.

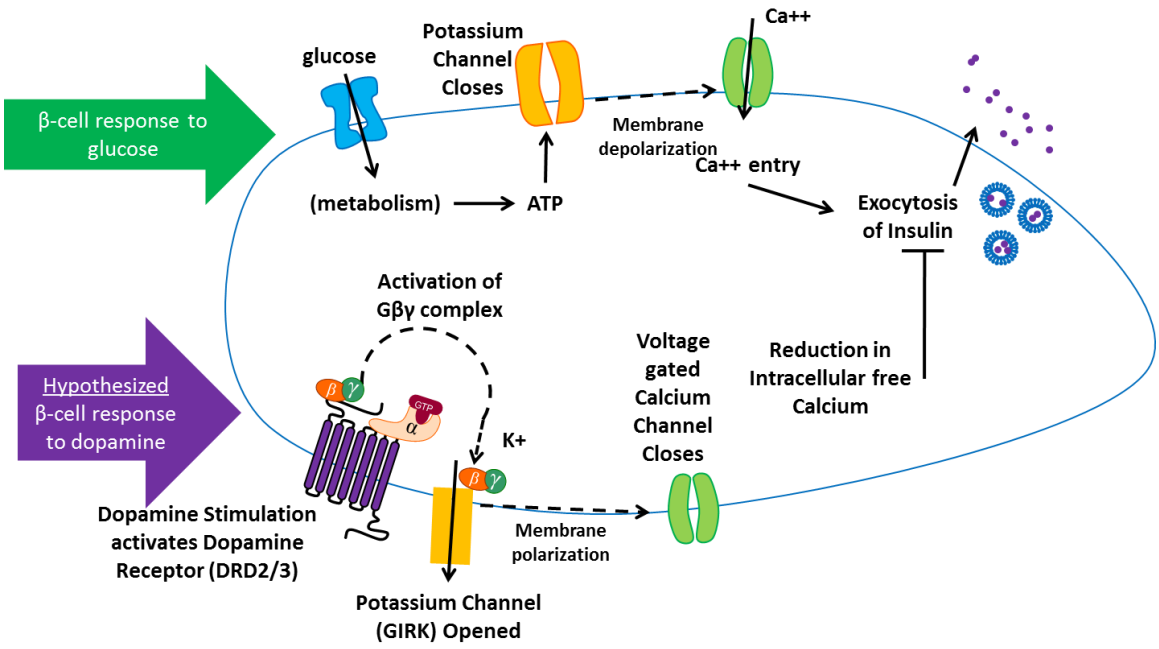

Figure 11 Proposed Dopamine Mediated Negative Feedback Pathway

This dissertation is organized as follows: Theory and current applications of fluorescence fluctuations spectroscopy are presented in the second chapter. In the third chapter, I present the methodologies used in this work. I present experimental results of interactions between the dopamine receptors and G-proteins in the fourth chapter and interactions between G-proteins and the proposed target channel, GIRKs in the fifth chapter. This dissertation is concluded with the relation of this work to current literature and future directions.

CHAPTER 2

FLUORESCENCE FLUCTUATION SPECTROSCOPY

Tools for Understanding Protein–protein Interactions

There are many techniques to measure protein-protein interactions, some of the most popular are protein affinity chromatography, co-immunoprecipitation, and yeast two-hybrid screening. Protein affinity chromatography uses a column containing immobilized proteins. Cell extract proteins are then passed through the column. Proteins that do not interact with the immobilized proteins immediately flow through while those proteins that do interact are retained. Multiple ligands can be tested with a single receptor in protein affinity chromatography; however, proteins are out of their native cell environment and by using cell extracts, cells must be destroyed to perform protein affinity chromatography (122, 123). Similar to chromatography, immunoprecipitation can determine protein interactions by incubating cell extracts and an antibody. The antigen is then precipitated and the proteins eluted so they can be analyzed. Immunoprecipitations are often used as they are easy to perform and allow the testing of a whole cell extract at once (122). Both protein affinity chromatography and immunoprecipitation do not discriminate between two proteins interacting directly versus indirectly and require the cell to be lysed (122). In yeast two-hybrid screening, a bait and fish method is used to determine if two proteins are interacting. The protein of interest (the bait) is attached to the DNA binding domain of a transcription factor for the host, typically yeast. The proposed receptor (the fish) is bound to the activation domain

of the transcription factor. If the two bind together, a HIS reporter gene will be transcribed. If the two do not bind together the HIS reporter gene will not be transcribed and a new receptor (fish) is tried. Yeast two-hybrids are easy to perform, but they result in a high rate of false positives. Lastly, the reaction must be able to happen in yeast, often a non-native environment for the proteins of interest (124, 125).

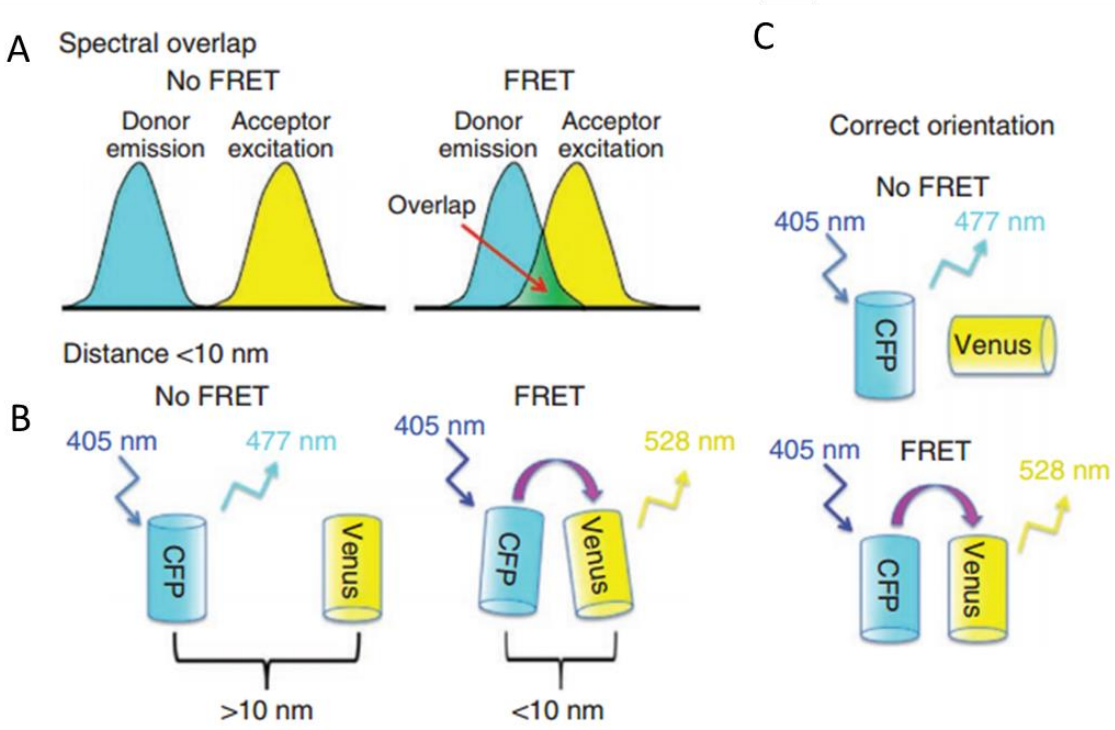

Figure 12 Three conditions must be met for FRET to occur. A. The donor fluorophore's emission spectrum must overlap with the acceptor fluorophores excitation spectrum. B. The fluorophores must be in close proximity of each other, 10 nm apart, for the energy transfer between the two fluorophores to occur. Last, the two fluorophores must be oriented for dipole-dipole coupling to occur. (from (126)**)**

In vivo and in situ methods, while more difficult to implement, have been developed to overcome the difficulties of in vitro protein interaction approaches. Unlike the in vitro methods, screening protein interactions are not easily performed within the cell and therefore these methods are not used to test many protein interactions at once.

Förster resonance energy transfer (FRET) measures the transfer of energy from one donor fluorophore in its excited state to an acceptor fluorophore through dipole-dipole coupling. FRET is commonly used in situ to measure protein interactions and biochemical reactions. Due to its popularity, many FRET sensors have been developed for easier application of the technique (127–129). However, FRET is not without drawbacks as it is often limited by low signal to noise ratios. Furthermore, both fluorophores must be properly aligned and within close proximity (<10 nm apart) to each other, shown in figure 12, resulting in high frequency of false negatives, even between two proteins which are known to interact (130). Like FRET, FFS detects weak and transient protein interactions in situ; however, FFS does not depend on the fluorophore proximity or orientation of the two fluorophores. Furthermore, the signal to noise ratio depends on the quantum efficiency of the fluorophores and the sensitivity of the detector. Current laser-scanning microscopes allow FFS measurements without specialized equipment which was previously required. Although artifacts from bleaching and intersystem crossing to the triplet state must be avoided, robust analysis procedures have been developed and are easy to implement on FFS data sets which are discussed below (131–135).

Historical Background

In 1972, Magde, Elson, and Webb published the first papers on fluorescence fluctuation spectroscopy (FFS) (136–138), where they presented the technique that they called Fluorescence Correlation Spectroscopy (FCS) which was derived from dynamic light scattering. FCS was preferential to dynamic light scattering to measure particle

motion because fluorescent moieties could easily be attached to the molecules of interest and fluorescence is more chemically selective than light scattering (135). The optical setup from these early experiments is shown in figure 13. In 1976, Hirschfeld published the first application of fluorescence microscopy to detect single molecules; while not directly related to the FCS experiments, his work would lead to the development of modern FCS. Without the development of detectors with higher quantum efficiency and stable lasers, FCS was not immediately applied until the early 1990s when Rigler's group showed a confocal microscope could excite and measure fluorescence fluctuations (135). Confocal microscopy reduced the excitation volume; which in turn reduced the quantity of backscattered light which hindered early FCS experiments. The decreased noise from backscattered light additionally reduced integration times needed to quantify the fluctuations in a sample. Last, with the use of confocal microscopy based FCS, single photon counting methods could be for autocorrelation measurements. Due to the advancements made by Rigler's group, FCS developments and applications greatly increased thereafter (139, 140).

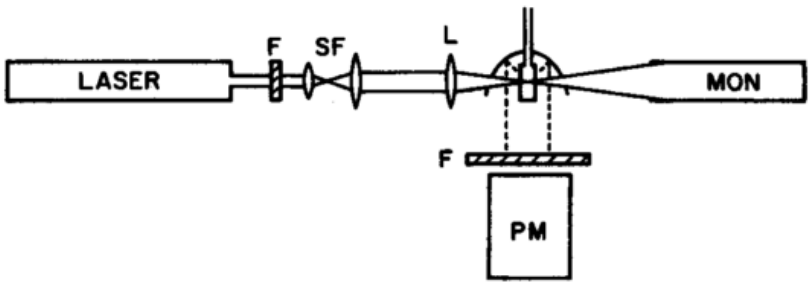

Figure 13 Schematic of optical setup from first FCS experiments. Excitation light from the laser passes through a colored filter (F), two spatial filters (SF) and through a lens (L) before exciting the sample. A laser intensity monitor (MON) measures the intensity at the sample. Emitted fluorescence is collected from a parabolic fluorescence-collecting mirror, passed through a filter and collected by a photomultiplier. (from ((137)**)**

The next significant advancement in FCS was the development of two-color fluorescence cross-correlation spectroscopy (2cFCCS). Single color FCS can only detect binding between two molecules if the change in molecular size is increased or decreased by 10 times or more. Translational diffusion, D, is related to the size of a molecule as shown in equation 1 where k is Boltzmann's constant, η is the viscosity of the solution, T is the temperature, and r is the hydrodynamic radius of the molecule.

$$D = \frac{kT}{6\pi\eta r}$$

Equation 1

The radius of the molecule, r, is related to its molecular weight, MW, by equations 2 and 3 where $\bar{\upsilon}$ is the specific gravity and V is the volume.

$$V = (MW)\bar{\upsilon} = \frac{4}{3}\pi r^3$$

Equation 2

$$r = \left(\frac{3MW\bar{\upsilon}}{4\pi}\right)^{1/3}$$

Equation 3

A tenfold increase in the molecular weight results in only a 2.15-fold change in the diffusion coefficient. Thus, without large changes in molecular size when two molecules bind together, no detectable change in diffusion is measured by FCS. 2cFCCS tracks both molecules when they are bound and unbound and therefore can detect the presence of lack of interactions between both molecules independent of changes in molecular weight. 2cFCCS can be performed with one excitation beam; however, many of the original experiments performed with single photon excitation used two lasers to excite the two different fluorescent molecules (131, 141–144). When two beams are

used, both beams are overlapped to create the excitation volume. Each beam excites a different fluorophore, traditionally one green and one red (131, 141–144). Emission is collected and the two bandwidths are separated and detected independently. The intensity fluctuations in the two bandwidths are then cross-correlated and the probed interactions then analyzed. In this procedure, the cross-correlation curve is only a function of the fluctuations of both channels, not those of each channel independently. Because FCS measurements can be used to quantify the number of molecules in an excitation volume, 2cFCCS measurements quantify the number of bound molecules in relation to the unbound molecules of each channel (131, 141–144). While still implemented, one drawback of this technique is the need for two lasers with two imperfectly overlapping excitation volumes. Two-photon excitation provides the ability to excite two fluorophores of different emission wavelengths with one laser and therefore one excitation volume (145, 146).

Brightness analysis methods provided an additional technique to analyze fluorescence fluctuations. Fluorescence intensity distribution analysis (FIDA) and the photon counting histogram (PCH) were the first methods used to analyze the brightness of the fluctuating fluorophores (147, 148). Both methods, developed independently, analyze the moments of the fluorescence intensity distributions to determine the molecular brightness. With two component PCH, a heteromerization brightness component can be determined, relating to the extent to which two fluorophores are interacting with each other. A newer brightness analysis technique developed by Müller was a time-integrated fluorescent cumulant analysis (TIFCA) which uses the factorial

cumulants of the moments of fluorescence intensity distributions to resolve the compositions of heterogeneous mixtures (149–151).

To better probe samples, specifically biological samples, FFS has been combined with other microscopy imaging techniques. For example, image correlation spectroscopy (ICS) and Raster image correlation spectroscopy (RICS) measure particle movements by detecting fluorescence changes in successive images so that multiple spatial points can be tested in parallel (152, 153). ICS and RICS have been used to probe slow moving molecules in cells where single particle movement would be difficult and time consuming (152–156). Another recent application is scanning FCS (sFCS) where the excitation volume moves at a set rate on a predefined path during integrations. sFCS has been frequently applied to membrane measurements where localization of the membrane can be difficult. Because protein diffusion is slower at the membrane than cytoplasm the slowest diffusion rate coincides to the scanning of membrane bound proteins (157–160). These three techniques, while not an exhaustive list of the recent developments, highlight the improvements allowing better FFS measurements of biological samples.

FFS Theory

In FFS, a small excitation volume of ~1 femtoliter excites fluorophores to a excited state. As molecules move into the excitation volume, fluorescence increases, and as they move out, fluorescence decreases. The fluctuations in the fluorescence is then collected, figure 14.

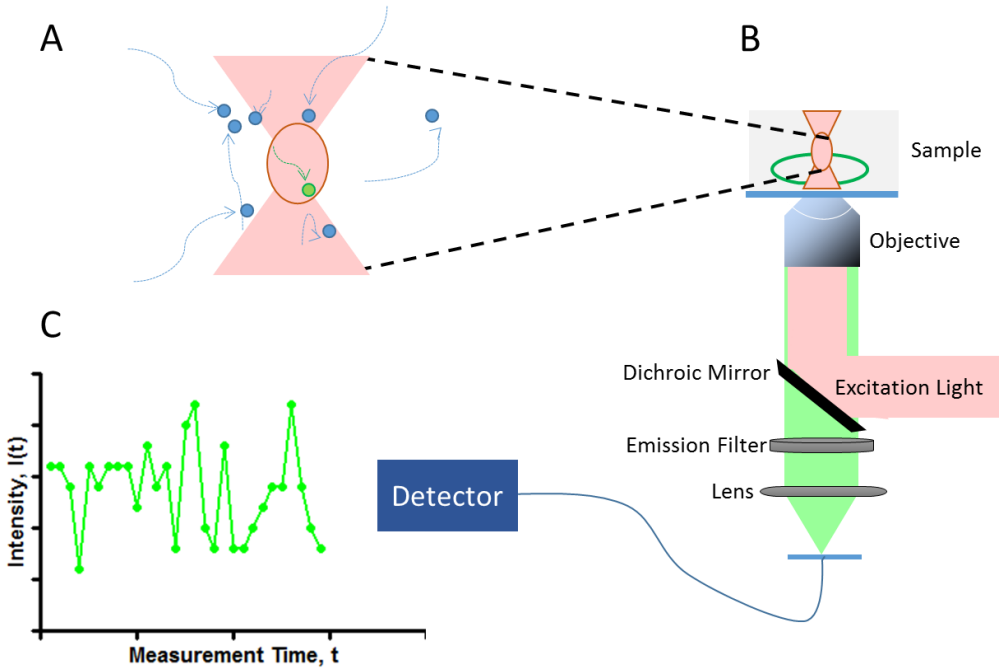

Figure 14 Schematic of FFS measurement. As molecules move in and out of the excitation volume, fluorescence will increase or decrease, respectively (A). Emitted fluorescent light is collected and a detector measure the intensity over time (B). C Intensity counts over time have small fluctuations, due to the movement of molecules in and out of the excitation volume, but a stable average count rate.

The probability of a population of, n, being present in the excitation volume with the average number of molecules, N, is described by a Poisson distribution (161, 162).

$$P(n,N) = \frac{N^n}{n!}e^{-N}$$

Equation 4

If molecules are diffusing at a high speed, the number of molecules within the excitation volume will also change rapidly. Molecules moving at a slow speed will enter and leave the excitation volume at a slower speed as shown in figure 15.

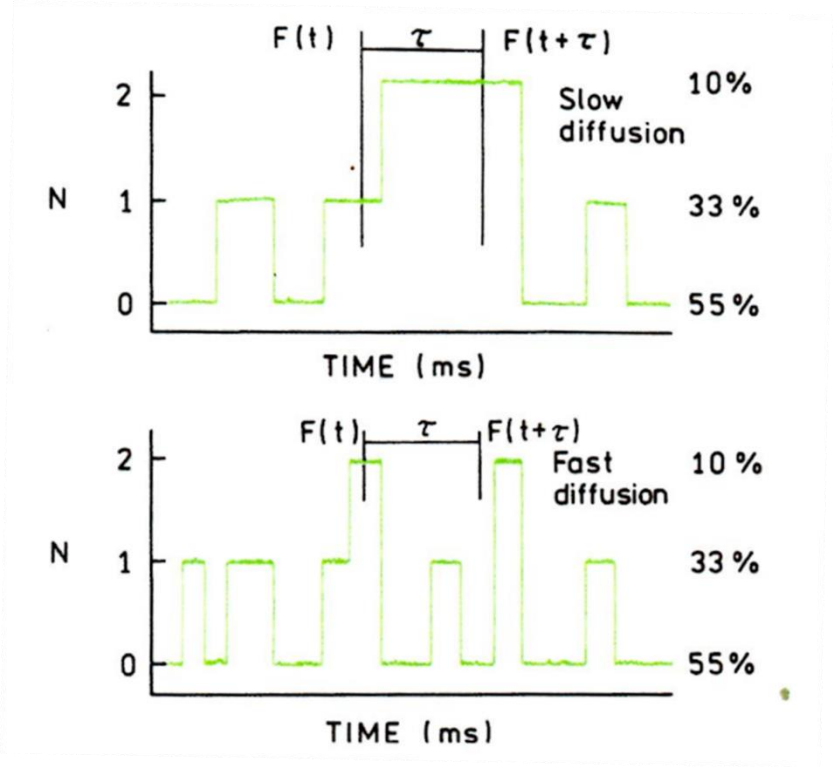

Figure 15 Schematic showing the differences between a slow diffusing molecule and a fast diffusing molecule. In the slow diffusing molecule, for a set lag time (τ) one count change has happened over the time frame. However, for the fast diffusing molecule, over the same lag time 3 count changes have occurred. The autocorrelation function for the slow diffusion data would result in a wider curve indicating slower diffusion time whereas the faster fluctuations would result in a narrower autocorrelation curve indicating faster diffusion. (from (161)**)**

FCS Theory

In FCS, two time points are denoted as t and t+τ to indicate the time difference, or lag time, between the two points. As τ approaches 0, fewer molecular diffusions occur and therefore the two time points should be strongly correlated. As τ increases, more molecules have entered and exited the excitation volume and therefore the two time points are expected to be less correlated. This is the central theory of autocorrelation, explained mathematically in Equation 5 (163).

$$\langle b(t)b(t)\rangle \leq \langle b(t)b(t+\tau)\rangle$$

Equation 5

Two variables which are correlated will change together whereas two uncorrelated variables will change independently of each other. In FFS, one is interested in the changes in fluorescent signals from a sample containing fluorescent fluorophores. FFS fluctuations can be from chemical reactions, enzymatic reactions, translational diffusion, rotational diffusion, and photophysical transactions (135, 161, 164, 165). The fluorescence fluctuations occurring from a sample over time relate to the reaction happening in the excitation volume. At short lag times, less changes in the excitation volume have happened so fluctuations are dependent on each other. At long lag times, more fluctuations have occurred and we expect fluorescent counts to be independent of each other. Equation 5 can be normalized to obtain a value relating the amount of correlation between the time points (163).

$$g = \frac{\langle b(t)b(t+\tau)\rangle}{\langle b(t)b(t)\rangle}$$

Equation 6

If g is a measure of the correlation between the two time points, g will be greater than 1 when variables are correlated, equal to 1 when uncorrelated, and 0 when anti-correlated (163). This is extended to fluorescence fluctuation counts as shown in Equation 7 (161, 163).

$$G(\tau) = \frac{\langle F(t+\tau)F(t)\rangle}{\langle F(t+\tau)\rangle\langle F(t)\rangle} = \frac{\langle F(t+\tau)F(t)\rangle}{\langle F(t)\rangle^2}$$

Equation 7

It is assumed that there are no changes over time to the statistical process occurring so that the average counts at both lag times are equal.

$$\langle F(t+\tau)\rangle = \langle F(t)\rangle$$

Equation 8

Oftentimes, the autocorrelation function is written as the difference or change in fluctuations from the mean (161, 163).

$$\delta F(t) = F(t) - \langle F\rangle$$

$$G(\tau) = \frac{\langle F(t+\tau)F(t)\rangle}{\langle F(t)\rangle^2} = \frac{\langle(\delta F(t+\tau) + \langle F\rangle)(\delta F(t) + \langle F\rangle)\rangle}{\langle(\delta F(t) + \langle F\rangle)\rangle^2} = \frac{\langle \delta F(t+\tau)\delta F(t)\rangle + \langle F\rangle^2}{\langle F\rangle^2}$$

$$= \frac{\langle \delta F(t+\tau)\delta F(t)\rangle}{\langle F(t)\rangle^2} + 1$$

Equation 9

As shown above, there is only the additive difference of one between the two equations. The difference in fluorescent counts from the mean can be equated to the focal volume times the changes in concentration of the fluorescent probe within the volume (164).

$$\delta F(\vec{r}, t) = \phi(\acute{r})\delta C(\vec{r}, t)$$

Equation 10

Integrating over the focal volume defines the fluorescence signal itself (163, 164).

$$F(t) = \int \phi(\vec{r})\delta C(r, t)d^3r$$

Equation 11

The average fluorescence signal can then be derived to be (162)

$$\langle F(t)\rangle = \langle C(t)\rangle \int \phi(\vec{r})d^3r$$

Equation 12

Inserting Equation 10 and Equation 12 into Equation 9 results in the autocorrelation function written as (161, 162, 164)

$$G(\tau) = \frac{\iint \phi(\acute{r})\phi(\vec{r}')\langle \delta C(\vec{r},t)\delta C(\vec{r}',t+\tau)\rangle d^3r d^3r'}{[\langle C(t)\rangle \phi(\acute{r}) d^3r]^2}$$

Equation 13

where $\langle \delta C(\vec{r},t)\delta C(\vec{r}',t+\tau)\rangle$ is the correlation function of a concentration fluctuation at point ŕ at time t and a concentration fluctuation at point $\vec{r}'$ and time t+τ (164). As $\tau \to 0$, Equation 13 reduces to the shape function ($\gamma = \sqrt[2]{2}$ for 2-photon excitation) divided by the number of molecules in the excitation volume (161, 162).

$$G(0) = \gamma \frac{\langle \delta C(t)^2 \rangle}{\langle C(t)\rangle^2} = \gamma \frac{1}{\overline{N}}$$

Equation 14

For a data set, the autocorrelation function is computed in Fourier space as follows (162)

$$Corr\{I(t), I(t+\tau)\} \leftrightarrow I(f)I^*(f)$$

Equation 15

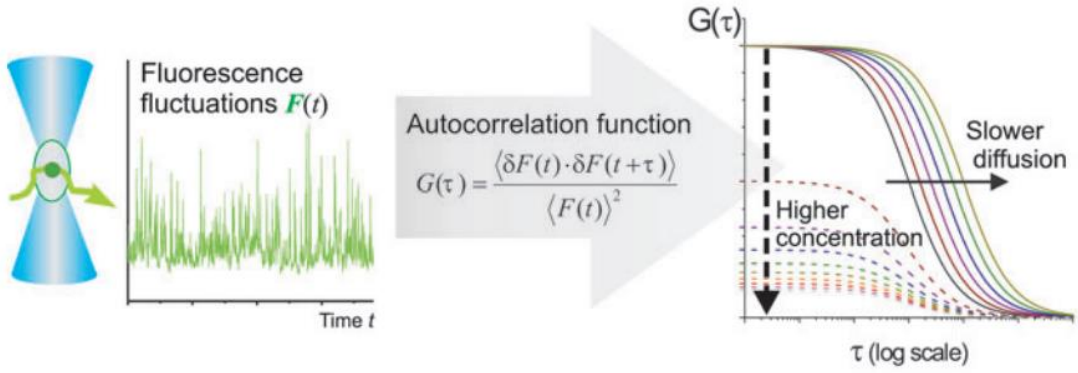

Figure 16 Fluorescence fluctuations can be used to calculate the autocorrelation curve. The higher the concentration of fluorescent molecules, the lower the y-intercept (G(0)). Additionally, the width of the autocorrelation function relates to the diffusion rate of the fluorophore. The faster the diffusion, the narrower the autocorrelation curve will be. The slower the diffusion of the molecule, the wider the autocorrelation curve will be. (from (166)**)**

From the autocorrelation curve, diffusion rate and fluorophore concentration can be calculated from fitting the curve. Equation 14 relates the inverse of the y-intercept of the autocorrelation function (G(0)) to the number of fluorescent molecules. In the autocorrelation curve, a higher concentration of fluorophores results in a lower y-intercept. The autocorrelation function also holds valuable information about the diffusion rate of the fluorescent molecule. A fast diffusing molecule that undergoes many changes for long lag times, as shown in figure 16, results in a narrower autocorrelation curve. Conversely, molecules diffusing slower in the excitation volume result in a wider autocorrelation curve.

PCH Theory

Photon counting histogram (PCH) analysis and fluorescence intensity distribution analysis (FIDA) both examine the fluctuations of fluorescence as molecules diffuse in and out of the small excitation volume (147). They differ only in the model used to describe the excitation volume, but both perform essentially the same analysis and therefore arrive to the same conclusions. PCH has become the more popular of the two methods and is the methodology used in this dissertation. In Equation 4, I related the probability of a population of fluorophores, n, being in the excitation volume to a Poisson distribution. By definition, in a Poisson distribution the variance is equal to the mean.

$$\langle \Delta n^2 \rangle = \langle n \rangle$$

Equation 16

This is the case for a stable excitation source; however, any fluctuations in intensity causes the variance to grow larger than the mean. Fluorescence intensity at a detector is therefore equal to the point spread function of the excitation volume, $\overline{PSF}(\vec{r})$, the

intensity at the origin, I_o, and a coefficient relating to quantum yield and efficiency of the detector and microscope, β (148).

$$I_D = I_o \beta \overline{PSF}(\vec{r})$$

Equation 17

The Poisson distribution can thus be written with $N = \eta_I I_D$ where η_I is proportional to detection efficiency (148, 162).

$$P(n) = \int_0^\infty \frac{\eta_I I_D{}^n e^{-\eta_I I_D}}{n!} p(I_D) dI_D = \int_0^\infty Poi(n, \eta_I I_D) p(I_D) dI_D$$

Equation 18

For the case of a single particle where $\varepsilon = \beta \eta_I I_o$ (molecular brightness), Equation 18 can be written as Equation 19 (148).

$$p^{(1)}(k; V_o, \varepsilon) = \int_0^\infty Poi(n, \overline{\varepsilon PSF}(\vec{r})\,) p(\vec{r}) d\vec{r}$$

Equation 19

Because the particle must be confined within the volume V_o to be detected, Equation 19 can be rewritten as Equation 20 (148).

$$p^{(1)}(k; V_o, \varepsilon) = \frac{1}{V_o} \int_{V_o} Poi(n, \overline{\varepsilon PSF}(\vec{r}))\ d\vec{r}$$

Equation 20

Extending this case for multiple independent particles as shown in Equation 21 (148).

$$p^{(N)}(k; V_o, \varepsilon) = \int \dots \int Poi(n, \sum_{i=1}^{N} \varepsilon_i \overline{PSF}(\vec{r_i})\, p(\vec{r_1}) \dots p(\vec{r_N})\, d\vec{r}_1 \dots d\vec{r}_N$$

Equation 21

While this equation looks difficult to evaluate, it is simplified by the fact that the probability distribution for a sum of statistically independent variables is the convolution

of the probability distribution of those variables (148, 167). Equation 21 can therefore be simplified to Equation 22. Thus, PCH is the convolution of the average number of single particles within the volume (148).

$$p^{(N)}(k; V_o, \varepsilon) = \frac{\{p^{(1)}(k; V_o, \varepsilon) \otimes \ldots \otimes p^{(1)}(k; V_o, \varepsilon)\}}{N - times} = \langle p^{(N)}(k; V_o, \varepsilon) \rangle_N$$

Equation 22

FFS Measurements

Instrumentation

Modern FFS setups are based on the confocal instrumentation introduced by Rigler (139, 140, 163, 165), shown in figure 17. The main requirements for FFS measurements are an excitation source, excitation mode, and a detection mode (137, 163). The excitation source is a low power laser with low beam divergence and Gaussian spatial mode. It is important to have low laser power in FFS studies so that the fluorophore emission is in its linear range in proportion to excitation power. While single photon excitation (SPE) is still popular for FFS studies, many researchers are moving towards two photon excitation (TPE). TPE uses a pulsed infrared laser which is more costly than SPE lasers; however, TPE allows deeper penetration and causes less bleaching in the sample (143, 168, 169).

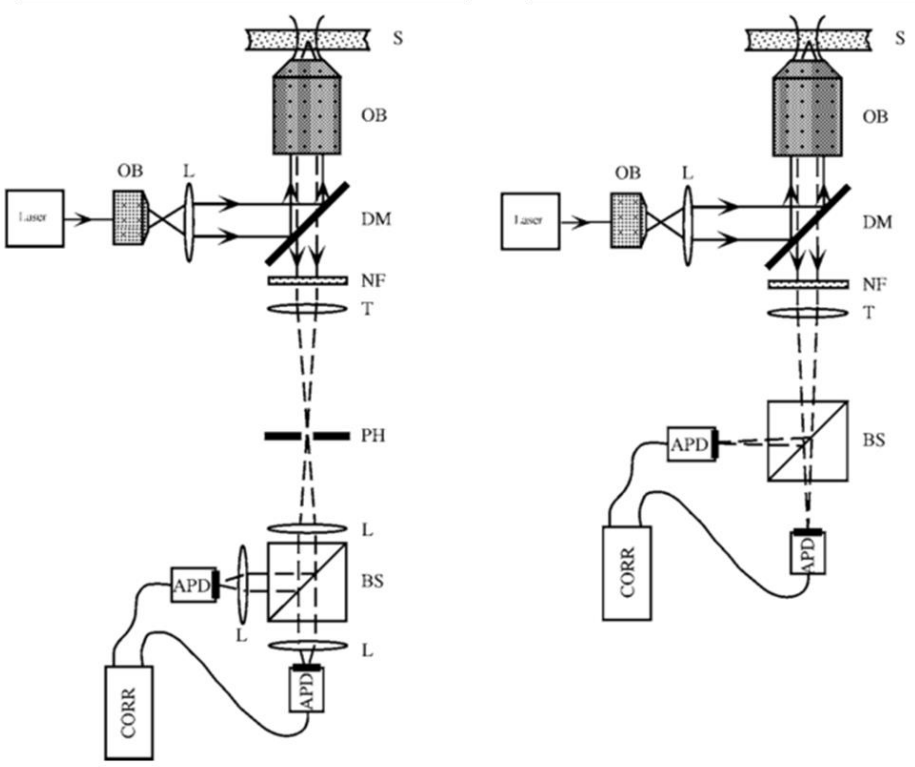

Figure 17 Optical setup based on the confocal instrumentation introduced by Rigler. Single photon excitation (left) and two photon excitation (right) S indicates the sample, OB objective lens; L lens; DM dichroic mirror; NF notch filter; T tube lens; PH pinhole; BS beamsplitter; APD avalanche photodiode; CORR correlator. (from (165)**)**

To excite a sample, laser light is focused into a high magnification microscope objective. High numerical apertures are necessary for FFS experiments to obtain a diffraction limited focal volume and high fluorescence emission collection (165). Oil immersion objectives with a high NA can be used; however, with deep aqueous solutions, optical aberrations occur (165). Therefore, water immersion objectives are generally preferred. The same objective lens is also used to collect fluorescence. For SPE, a pinhole is placed at the confocal plane to remove fluorescence due to out-of-focus light. Photomultiplier tubes (PMT), avalanche photodiodes (APD), complementary metal-oxide-semiconductor (CMOS) and electron multiplying charge-coupled device

cameras (EMCCD) have all been used to detect fluorescent counts in FFS experiments. When selecting a detector, the detection rate must be higher than the expected diffusion rate of the molecule. Thus, it is necessary that detectors have high quantum efficiency to optimize signal-to-noise at high detection rates. Historically, APDs have been the preferred detector; however, new GaAsP PMT detectors are recently becoming the common FFS detector, figure 18 (165).

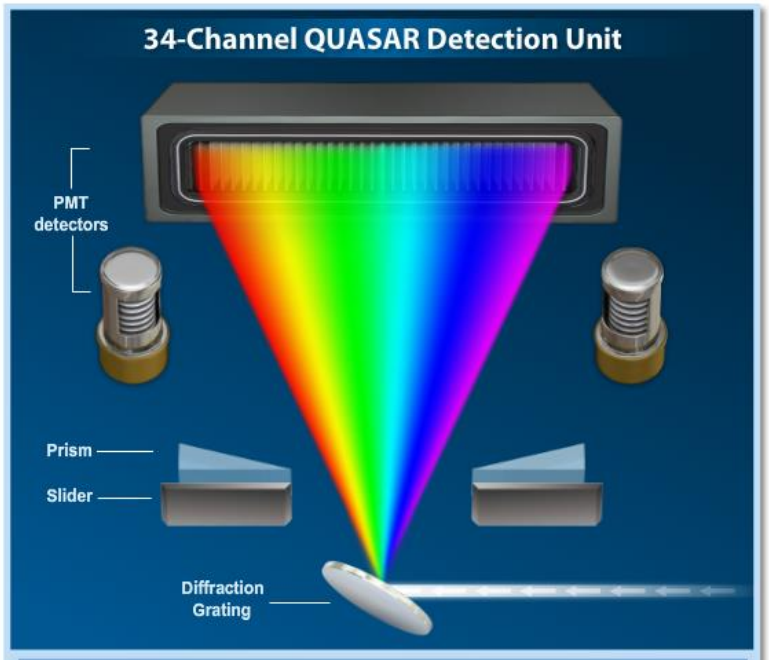

Figure 18 Detector setup for Zeiss LSM 780. Emission beam paths is spectrally separated with a diffraction grating and detected by PMT detectors or an array of GaAsP detectors (from (170)**)**

In this dissertation, a Ti:Sapphire laser was chosen to excite samples at 1000nm which excites both the green and red fluorophores. Light was focused the sample with a 40X, 1.2NA, water immersion objective. Emitted fluorescence was collected with the same objective and spectrally separated. 34 GaAsP detectors collected the light in 10 nm bins (171).

To optimize the FFS signal, the following properties of the selected fluorescent tag, dye or protein, are of greatest significance: high quantum yield, high photostability, and low singlet-to-triplet state quantum yield. The signal for FFS depends on the brightness of a few excited fluorophores, therefore it is important to choose fluorophores with high emission per molecule. Photobleaching can cause molecules to appear that they are diffusing faster than they are; thus fluorophores with high photostability are preferred in FFS experiments (172). Last, fluorophores with low singlet-to-triplet quantum yield is desirable as triplet state emission can distort the correlation function.

Single Component Measurements

In single component FFS measurements, one fluorescent probe is used to monitor fluctuations in the system. Even with a single fluorescent marker, a significant quantity of information can be gained about the system, in addition to fluorophore concentration and diffusion rate (135, 161, 164). Boukari studied the formation of tubulin aggregation with FFS. When cryptophycin, a protein that promotes tubulin aggregation, was added to the sample, the diffusion rate decreased 250%, indicating homerization of tubulin particles (173).

FFS can also be used to study protein binding through changes in the diffusion rate of the labeled molecule. However, to adequately detect changes in solution due to the interaction of molecules, the molecular weight must increase ~10 times for the change in diffusion to be seen. Pack and colleagues studied the interactions between a partially denatured protein α-Lactalbumin with a chaperonin protein GroEL which promotes protein folding (174). The denatured α-Lactalbumin has a molecular weight of 14,000 whereas the GroEL's molecular weight is 840,000. Therefore, the binding of α-

Lactalbumin to the GroEL will result in molecular weight increase larger than ten times. Pack showed the binding of GroEL altered the diffusion rate of α-Lactalbumin, which indicates the GroEL was promoting proper folding of α-Lactalbumin (174). Most single component FFS studies measure changes in diffusion or homerization; however, with the development of unique sensors other applications have been performed. For example, Webb's lab developed a pH sensor with FFS. At low pH levels EGFP becomes quenched due to an ionized hydroxyl group and thus a portion of EGFP molecules become quenched faster than they diffuse in and out of the volume. These molecules therefore look to be diffusing faster than they really are. Webb's lab showed the portion of molecules diffusing at a perceived faster rate is proportional to the pH level (146).

FCS is most commonly used to probe translational diffusion of molecules. Correlation in three dimensions with two-photon excitation is calculated by (161)

$$\langle \delta C(\vec{r},t)\delta C(\vec{r}',t+\tau)\rangle = \bar{C}(8\pi Dt)^{3/2}\exp[-|\vec{r}-\vec{r}'|^2/8Dt]$$

Equation 23

Inserting into Equation 13 results in Equation 24 which can easily be fitted to the autocorrelation points of the experimental data (164, 165, 175).

$$G(\tau) = G(0)\left(1+\frac{8Dt}{w_x^2}\right)^{-1}\left(1+\frac{8Dt}{w_z^2}\right)^{-1/2}$$

Equation 24

In the special case where two diffusion rates exist for a single probe (bound and unbound protein for example), the autocorrelation function is additive of each constituent (165, 175).

$$G(\tau) = \frac{1}{N^2}[N_1 D_1(\tau) + N_2 D_2(\tau)]$$

Equation 25

The last important fitting model is for lateral diffusion, for example, protein diffusion upon a membrane. In this case, only the 2D component is necessary from Equation 24 (175–178).

$$G(\tau) = G(0)\left(1 + \frac{8Dt}{w_x^2}\right)^{-1}$$

Equation 26

Through the combinations of Equations 24-26, many autocorrelation curves can be adequately fitted to determine diffusion rates and molecular concentration.

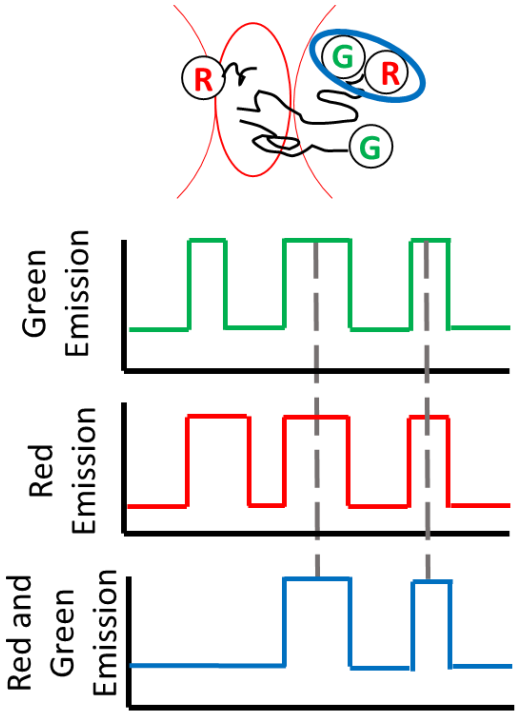

Figure 19 Schematic showing emission counts from both the green and red channel are independent from each other as molecules are independently labeled with the fluorophores. Molecules diffusing together however, will change the counts simultaneously. The cross-correlation is the co-diffusion of green and red labeled molecules diffusing together. (adapted from (161)**)**

Two-Color Cross-Correlation Measurements

In two-color FFS, two fluorescent probes label two separate fluorescent labels. Due to the weak relation between molecular weight and diffusion, many heteromerization processes cannot be detected by probing a system with a single fluorophore. However, with the invention of two-color FFS, heteromerizations that are not caused by a large change in molecular weight can be detected (179, 180). Traditionally, 2cFFS is performed with a green and red fluorophore, relating to the green and red channels, respectively (131, 181). Fluctuations of each channel are measured independently and therefore, two autocorrelation curves are formed. Because the green and red labeled proteins are independent of each other, different time-dependent fluctuations will occur in each channel independently of each other (figure 19). Changes that occur simultaneously relate to the co-dependence of both labeled molecules (131, 181). Thus, the measured cross-correlation is dependent upon the relation between fluctuations in the green and red channel upon each other. The cross-correlation function can therefore be defined as Equation 27, where G represents the green channel and R represents the red channel (131, 146).

$$G_{CC}(\tau) = \frac{\langle F_G(t+\tau)F_R(t)\rangle}{\langle F_G(t)\rangle\langle F_R(t)\rangle}$$

Equation 27

In figure 20, two autocorrelation curves and their cross-correlation curve are shown. As with the y-intercept of autocorrelation curves, G(0) of the cross-correlation curve also relates to the number of molecules present in the system. A change in the amount of interacting particles can therefore be determined by the ratio of cross-correlated particles to the independent species (131, 141, 182, 183).

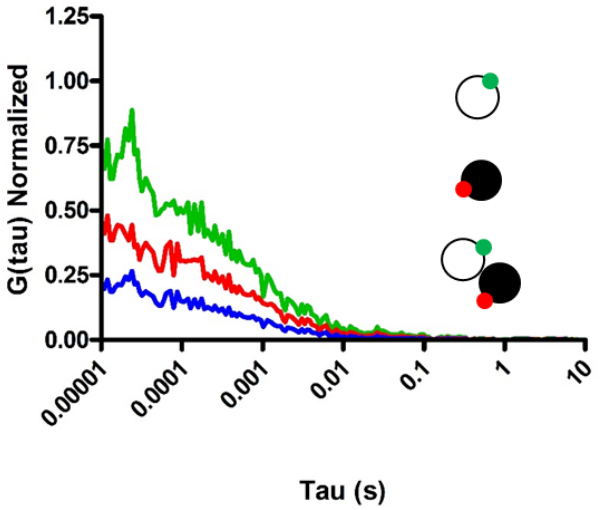

Figure 20 Autocorrelation curves (green, red) and their cross-correlation curve showing the interaction of green and red molecules diffusing together.

Historically, many 2cFFS measurements have been performed with two different excitation lasers, one to excite the green channel and one to excite the red channel (131). The introduction of two lasers causes two point spread functions that do not perfectly overlap, leading to increased calibrations and analysis to determine cross-correlation parameters (131, 183). The use of a single, two-photon excitation path removes these difficulties as a single laser is able to excite both channels at the same time.

Photon Counting Histogram

Single Component PCH

PCH analysis uses the same fluorescent fluctuation data which is gathered to derive an autocorrelation curve. A histogram is made by plotting the occurrence against the number of photon counts in each time bin, as show in figure 21. Oftentimes, as

shown in the insert, the PCH is plotted on a semi-logarithmic scale to see the differences in the super-Poisson distribution formed by PCH as compared to a Poisson distribution. The histogram is then fit to the model (Equation 22) to determine the molecular brightness and sample concentration.

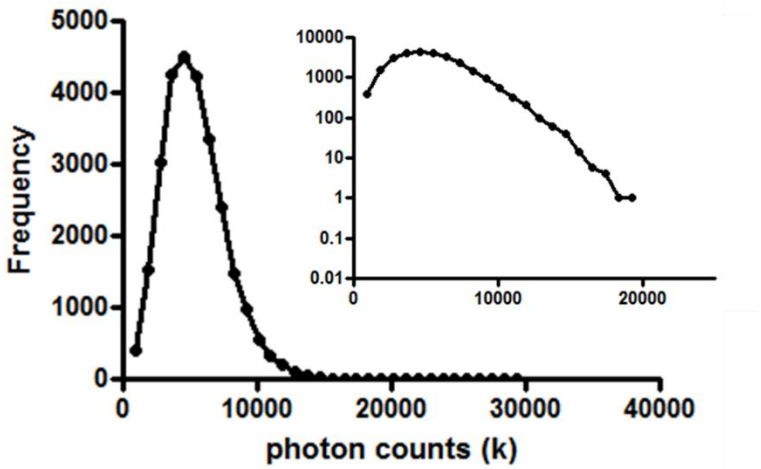

Figure 21 Photon Counting Histogram

An advantage of PCH analysis over FCS is the ability to resolve two species with similar diffusion coefficients from differences in their molecular brightness. For example, Kask and colleagues were able to separate Rhodamine 6G and tetramethylrhodamine (TMR) and their proportions in a mixture through brightness analysis (147). Since both are rhodamine derivatives, their diffusion rates are similar and therefore are inseparable as a mixture by FCS. TMR is much dimmer than Rhodamine 6G (37kcpsm vs 107kcpsm) which allows the ability to distinguish and quantify both constituents by brightness analysis.

Current studies using PCH analysis have examined homerization of proteins in cells. A current hypothesis for some GPCR proteins is their diffusion on the membrane together. Herrick-Davis used PCH analysis to examine the homerization of the

Serotonin 5-Hydroxytryptamine 2C receptor and determined the protein diffuses in dimers on the membrane (184). Another report show the use of PCH to determine how the ABCG2 subunits combine into tetramers to form a functional transporter (185). While single component PCH analysis continues to be used to analyze homerization, a derivation of the technique developed by Paul Wiseman's group called spatial intensity distribution analysis (SpIDA) has simplified histogram analysis. SpIDA resolves protein oligomerization from single fluorescence microscopy images through histogram analysis (186–188). The technique is innovative as it can be applied to measure protein interactions from confocal images without the additional need of FFS equipment. Additionally, it is open source code and given as a Matlab graphical user interface for easy application. With the advent of this technique, histogram analysis has become more accessible to labs without FFS equipment.

Two Component PCH

Two-component PCH allows for the detection of heteromerization between two different fluorescently labeled molecules (132, 134, 189). As shown in figure 22, a 3 dimensional histogram is created to show the photon counts from the red and green channel. The heteromerization of the two channels is determined by their interaction, shown by high counts in the diagonal of the 3 dimensional histogram. The heteromerization brightness component can be calculated (independently of sampling time) by Equation 28.

$$\langle \varepsilon_{gr} \rangle = \frac{\sigma^2{}_{gr}}{\gamma \sqrt{I_g I_r}}$$

Equation 28

The most common application of dual-color histogram analysis is for the probing of protein oligomerizaton. For example, the Giese lab uses 2d-FIDA to examine aggregation of the protein a-synuclein with lipid vesicles in the pathogenesis of Parkinson's disease. Both, the a-synuclein and lipid particles, form homo-oligomers before combining together, making the heteromerization difficult to study with other protein-protein interaction detection methods (190, 191).

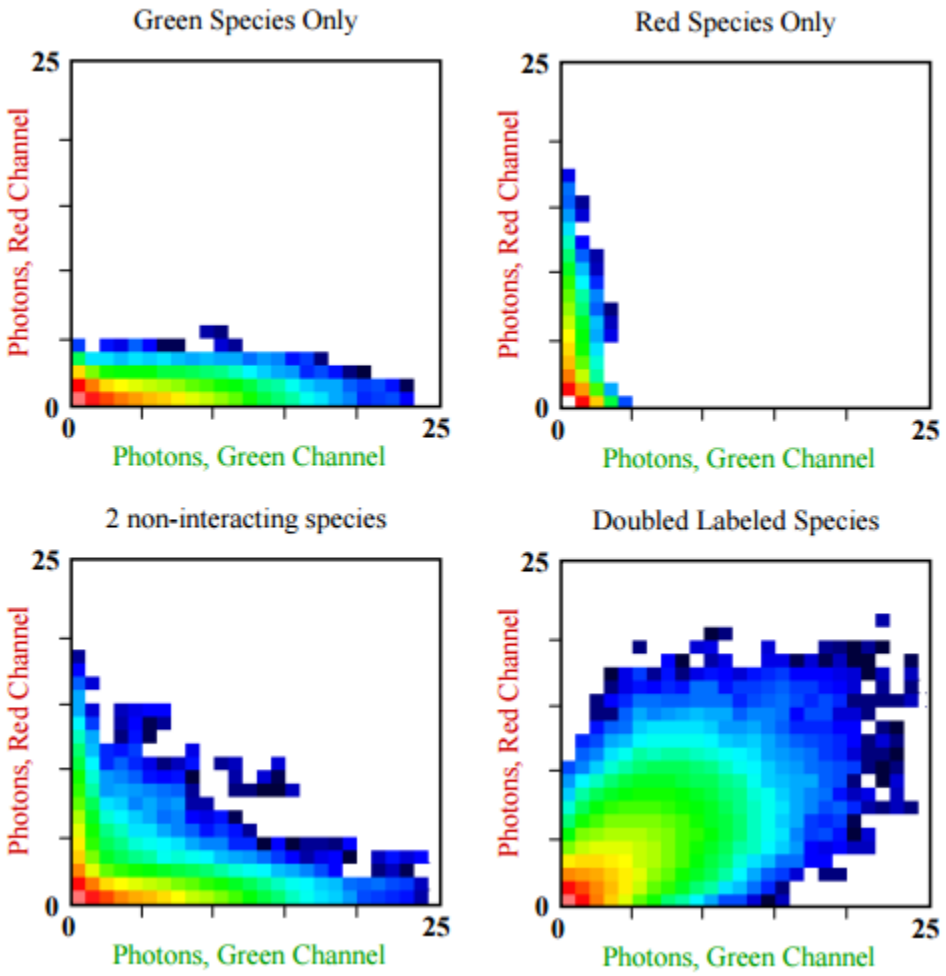

Figure 22 Two component histograms showing the counts from the red channel on the vertical access and counts from the green channel on the horizontal axis. In single component measurements, counts are distinctly shown to be from that channel only. For non-interacting species, the heat map shows counts from both channels, but independent of each other. For two interacting species (doubled labeled) the histogram is centered in the diagonal, between the two channels. (from (192)**)**

In this dissertation FFS is used to study the signaling between a GPCR, G-proteins, and a downstream target channel. Using two-photon excitation, one excitation volume can be used to excite two channels simultaneously. The autocorrelation curves from FFS measurements are used to calculate protein diffusion rates. Additionally, the cross-correlation curve formed provides information on the heteromerization between the two proteins being studied. Two proteins diffusing together on the membrane should have a higher cross-correlation component than two proteins diffusing apart. As a secondary analysis method, the heteromerization brightness component from dual-color PCH analysis is also calculated. To our knowledge, this is the first time FCCS and PCH have been used together to quantify protein oligomerization.

CHAPTER 3

METHODOLOGY

Introduction

In this chapter, I detail my procedures for taking FFS measurements. Proper cell preparation and instrument alignment are necessary each time measurements are taken. With FFS, the fewer molecules you can excite, the easier changes in fluctuations can be determined (175, 193). For example, it is easier to notice a change of 1 from 10 than 1 from 100. When looking for changes in fluctuations, it is easier to detect small changes in fluorescence with small average counts than small changes in fluorescence with large average counts. In solution studies, dilutions are easy to perform so that fewer molecules are within the excitation volume. For cells, one cannot easily dilute the amount of proteins expressed. Therefore, it is oftentimes the dimmest cells which FFS measurements can be performed on. In addition to expression levels, calibration of the microscope and proper alignment are essential to obtaining good measurements. If the beam does not properly fill the back aperture of the objective, the actual excitation volume will differ from the expected beam shape used to calculate diffusion rates. Each time FFS measurements are performed, alignment should be checked. With proper cell expression and instrument alignment, FFS measurements can be performed.

In this chapter, I first describe the chosen cell line, culture protocols, and transfection procedures. Next, I describe the instrument experiments were performed on and alignment methods followed by explanations of the modifications I made to plasmid

constructs which I used in this dissertation. Following, I detail the first experiments which I performed measuring protein diffusion in solution and in the cell. Last in this chapter, I present diffusion measurements of membrane proteins taken by FFS in comparison to those previously reported by fluorescence recovery after photobleaching (FRAP) (194).

Cell Preparation

MIN6 Cell Line

Primary cells are often a preferred method to study biological processes in vitro as the only significant modification made to the cell is removing them from the organism. In comparison to immortalized cell lines which are often additionally modified genetically or virally, the behavior of primary cells is expected to be closer to that of in vivo. However, primary cells are more difficult to maintain than an immortalized cell line. For the purpose of this dissertation, the MIN6 cell line was selected for all experiments due to its retained response to secrete insulin under high glucose conditions and not during low glucose (195, 196). From previous research, we know that under glucose stimulated insulin secretion (GSIS) the treatment dopamine inhibits insulin secretion (120). Since the inhibition of insulin secretion by dopamine is further studied in this dissertation, it is essential that the β cell line chosen retains its response to secrete insulin under high glucose conditions.

Cell Media and Culturing

Cells were maintained in a sodium bicarbonate Dulbecco's modified Eagle's medium (DMEM) with 25mM glucose, 1mM sodium pyruvate, and 4mM L-glutamine. Additionally, Penicillin (100 units/ml), streptomycin (100µg/ml), 50µM of β-mercaptoethanol, and a final dilution of 10% heat-activated fetal bovine serum were added to the media.

Media was exchanged at a minimum of every three days for healthy growth and proper pH ranges. Cells were split at 60-80% confluency with 0.25% Trypsin. After media neutralization, cells were pipetted up and down vigorously to break up clustering. Cells were plated at a minimum of 30% confluency. Cells were cultured at 37° Celsius with 5% CO_2. Low passages of cells are preferred as they retain better response to glucose stimulated insulin secretion; therefore, cells were only passaged up to 40 times (197).

Cell Transfection Background

A chemical transfection method with effectene was initially used to transfect MIN6 cells. Chemical transfections are often preferred to other transfection methods because they produce high efficiency transfections, are easily reproducible, and require small amounts of nucleic acids (198, 199). Effectene forms non-liposomal, cationic lipids which deliver the nucleic acid plasmids to cells, shown in figure 1. The lipids formed by effectene are not disrupted by serum making it less toxic to cells than many other chemical transfections (199, 200). A typical transfection requires 1µL of DNA to 10µL of effectene and transfects one 10mm diameter imaging dish. However, by increasing the ratio of effectene to DNA, larger (and/or multiple) plasmids can be transfected in one

reaction. As I increased effectene to introduce the large dopamine receptor plasmids, I began to notice my cells exhibited cell rounding and were not as well attached to the imaging dish after transfection. Cell imaging dishes were coated with α-poly-l-lysine to increase cell adherence (201); however, this disrupted the effectene transfections and resulted in cells with high adhesion to the imaging dish, but with little to no transfected cells (201).

To combat the difficulties with chemical transfections, I chose the physical method of electroporation to transfect MIN6 cells. Electroporation uses an electric field to momentarily disrupt the membrane, as pictorially shown in figure 23. DNA in the surrounding solution can then enter the cell during these disruptions. I used a square wave electroporator which gave multiple, short electrical pulses to the cells. In contrast to chemical transfections, electroporation transfections can be difficult to implement as there are many variables which must be determined for an efficient transfection. These include pulse width, number of pulses, rest interval time, DNA concentration, cell density, and DNA to cell ratio. Additionally, electroporation requires a larger amount of DNA in comparison to the number of cells transfected than chemical transfections. However, transfecting multiple plasmids into the cells does not require additional alterations to a previously determined electroporation protocol. Furthermore, electroporation transfections result in cells expressing the plasmids at a range of expression levels which is beneficial for FFS studies which require cells with low levels of expression (198, 202). Furthermore I found the cells which survived the electroporation were adherent to the glass bottom of imaging dishes without the

requirement of secondary treatments. For these reasons, electroporation was chosen as the method of transient transfections in this dissertation.

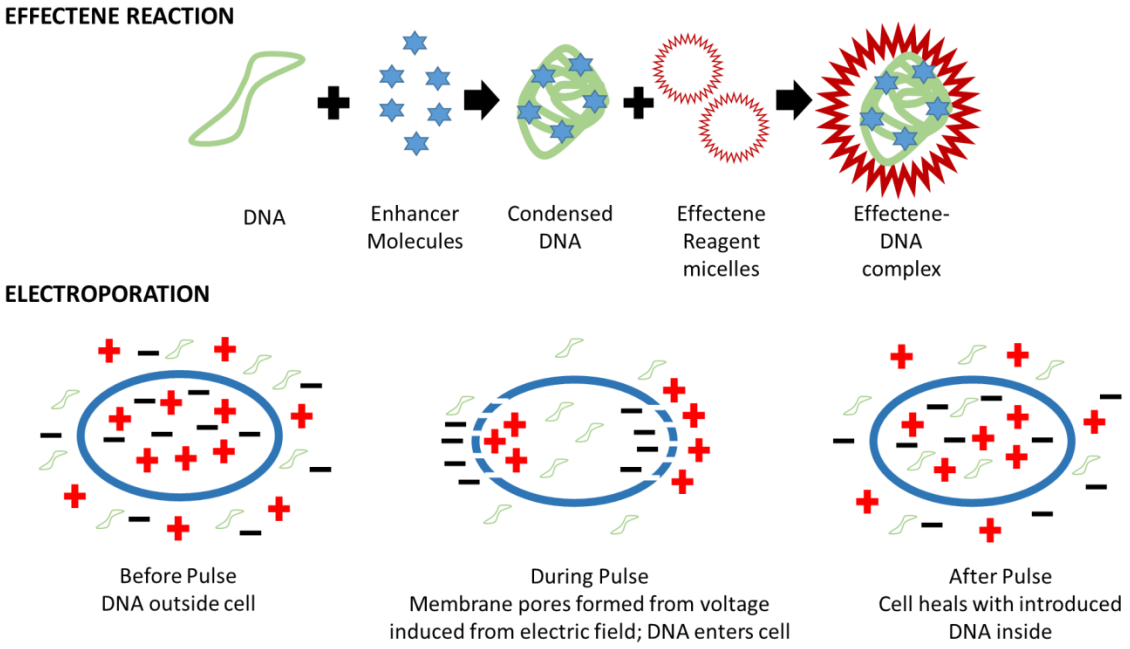

Figure 23 In an effectene reaction, an enhancer molecule is first mixed with DNA to condense the DNA. Condensed DNA is then mixed with the effectene reagent to form effectene-DNA complexes that the cell can endocytose. Conversely, in an electroporation reaction the electric field created from the applied voltage causes membrane pores to form. DNA can enter the cell through the pores formed during pulses. After the pulses, the cell membrane is healed and DNA that entered the cell during the pulses is inside the membrane. Cartoons adapted from Qiagen and BTX websites.

Cell Electroporation Transfection

One day prior to imaging, cells were detached from culturing flasks with trypsin. Once cells were detached, cell media was used to inhibit further trypsin activity. The cell suspension was placed in a 15mL conical centrifuge tube and transported on ice to a centrifuge. Cells were pelleted at 300 RPM (the lowest centrifuge speed) at 4°C for two to three minutes. Pelleted cells were removed from centrifuge and placed on ice. Media/Trypsin mixture was carefully removed and cells were re-suspended in PBS +

1mM $CaCl_2$ at 10^8 cells/ml. Forty microliters of the $CaCl_2$ cell suspension was transferred to a 2mm-gap cuvette. Ten micrograms of each plasmid, diluted in water to concentrations between 1,000-10,000 ng/ml, were placed in the cuvette. The cell/plasmid suspension was mixed by gently pipetting up and down prior to a 10 minute incubation period on ice. Cells were electroporated with a square wave electroporation system (BTX, Holliston, MA) for 10 pulses lasting 50 µs at 300 V (1500 V/cm) with 500ms intervals between each pulse. After electroporation, cells were diluted with warm media and plated on glass bottom dishes at a concentration of $1.5 \cdot 10^5$ cells/cm^2. Cells were incubated overnight and media was refreshed in the morning. Cells expressed plasmids properly for FFS measurements 24-48 hours after transfection.

Cell Imaging Buffer

Cell media was replaced with a Krebs-Ringer Bicarbonate Buffer (KRBH) with .1% bovine serum albumin (BSA) and 12 mM glucose for imaging. Cells were washed twice with KRBH buffer before imaging to remove phenol red. For cells treated with dopamine, dopamine hydrochloride was diluted to 100 µM with warm KRBH buffer. Due to the rapid degradation of dopamine in solution, new dopamine solution was every 4 hours.

Instrumentation and Calibration

General Overview

Cells were imaged on a LSM 780 confocal microscope (Zeiss). A tunable, mode-locked Ti:Sapphire laser was used to excite fluorescence. Excitation light was guided into the microscope and passed through a 760 nm long-pass dichroic beam splitter

before entering a 40X 1.2NA water immersion objective used to focus the beam at the excitation point. Fluorescence excited at the focal point of the objective was collected with the same objective. Collected fluorescence is again passed through the 760 beam splitter to separate excitation and emitted light. The emitted light is spectrally separated and 31 detectors collecting in wavelength bins of 10 nm collect the light. Detectors are GaAsP Quasar detectors which have almost double the quantum efficiency of PMT detectors in the visible range (Zeiss, Jena, Germany). The multiple detectors allows two channel detection, green and red, without the use of filters. Additionally, accepted wavelengths for each channel can be determined within 10nm ranges. Figure 24 shows the emission spectra for EGFP and mApple. Between 550 nm and 600 nm the spectral emissions for EGFP and mApple overlap and cannot be separated. To avoid EGFP emission bleeding into the mApple channel, mApple emission collected between 600-700 nm and EGFP emission was collected between 500-540 nm, shown in figure 24.

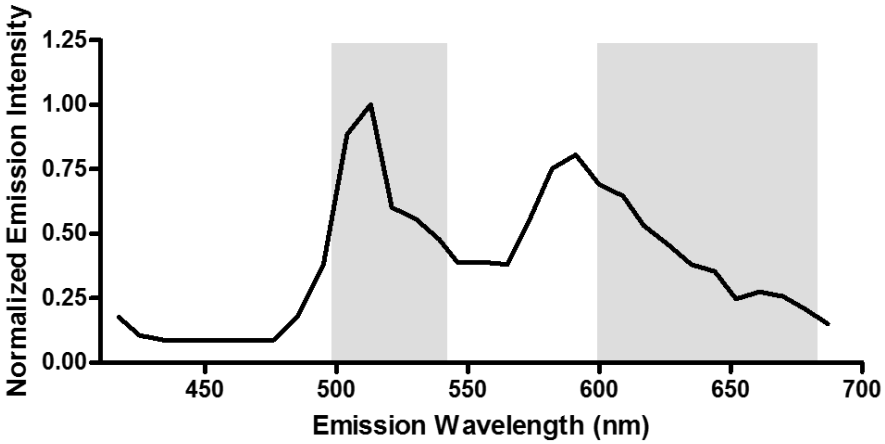

Figure 24 Normalized emission intensity of EGFP and mApple with the emission collection regions highlighted. To avoid cross-talk between the green and red channels fluorescence emission was only collected at wavelengths where EGFP and mApple emission did not overlap. EGFP emission was collected between 500 – 540 nm and mApple emission between 600 – 700 nm.

Alignment

Proper alignment of the microscope was verified from measurements of the point spread function (PSF) using images of submicron fluorescent beads of 100 nm diameter. Z-stacks of X-Y plane images show the point spread function in 3 dimensions. Non-ellipsoidal PSF images indicated the instrument was misaligned. X-Y planar images from the submicron beads were used to determine the beam width through ImageJ Java Script Point Spread Function Estimation Tool (MOSAIC Lab) (203).

Data Acquisition

FFS measurements require low average fluorescence count rates so that small changes in fluctuations can be determined. Preferred count rates are between 5-30 thousand counts per second. This expression level, while low, is ten times greater than that autofluorescence. Figure 25 shows the fluorescent counts of two cells used for FFS measurements with a count rate of 6 kcps and 6.2 kcps. Also shown is scattering (.2 kcps) and the autofluorescent counts from a cell not expressing the FP (.5 kcps).

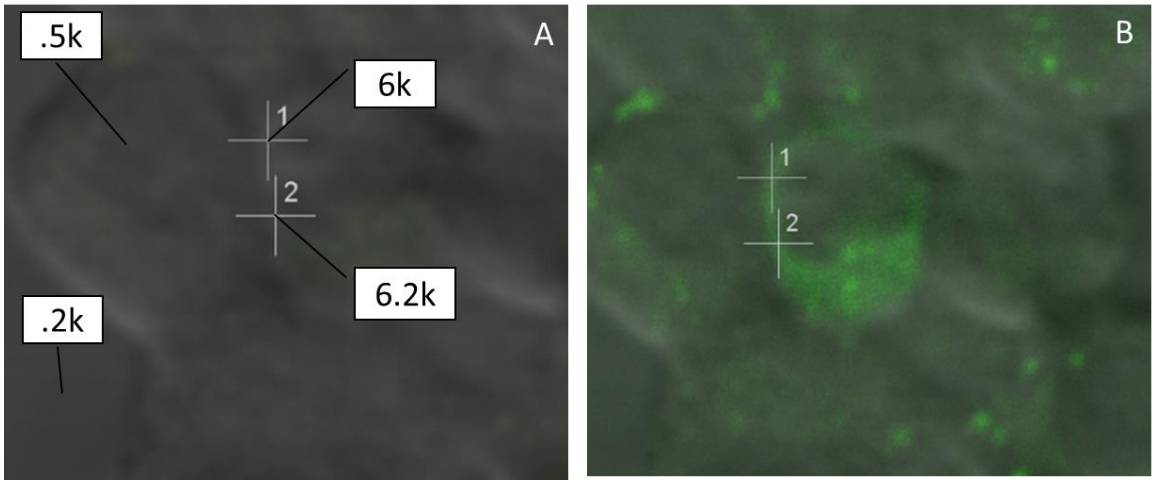

Figure 25 DIC and raster fluorescence image overlay of a cell properly expressing EGFP for FFS measurements (A) with contrast enhanced (B). At points 1 and 2, the count rate is within the range of 5-30 thousand counts per second. Also shown is the count rate for a cell not expressing EGFP (.5 kcps) and the count rate for the imaging buffer (.2 kcps).

Measurement times for FFS experiments vary from 10 seconds to 120 seconds depending on the diffusion rate of the sample. Molecules in solution are typically diffusing at a fast rate where slower measurement times are adequate to fully describe the fluctuations (193). Slow moving membrane bound molecules require longer measurement times to fully define the fluctuations occurring. Long cell measurement times can be difficult to obtain due to cell movement and mechanical/optical drift in the system. To compromise for the long measurement times needed to fully describe fluctuations of molecules at the membrane and cell movement and instrument drift, measurements were taken for 45 seconds. This timeframe provided enough time for well resolved correlation curves while being fast enough to obtain measurements without average fluorescence count changes.

Previous literature has shown at temperatures below 37 °C, protein diffusion rates decrease (194, 204). Microscope incubators, which are often used to keep cells warm while imaging, are not able to be used for FFS studies of cells because they cause small vibrations which moves the excitation volume causing inaccurate measurements of specific cellular locations. To keep the cells warm without vibrations, I used an objective heater which was kept at 37 °C. Additionally, each cell dish was imaged for no longer than one and a half hours. If cells exhibited rounding or detachment, the dish was immediately discarded.

Diffusion rates of membrane proteins are under 1 $\mu m^2/s$ (193, 194, 205–208). During the long measurement times used in my cell experiments, FPs that do not move in and out of the excitation volume are bleached. Bleaching reduces the average fluorescent counts at a slower rate than fluctuations occurring due to diffusion. The slow

change in counts produces an autocorrelation curve that emphasizes the slow change bleaching over the fast fluctuations of diffusing molecules. An example of bleaching and the autocorrelation curve produced is shown in Figure 26. To remove the artifact created by bleaching, an initial bleaching period is performed at the membrane before FFS measurements begin (175, 193). Once the slowly diffusing FPs are bleached, the average count rate is stable and fluctuations, occurring due to protein diffusion, can be measured.

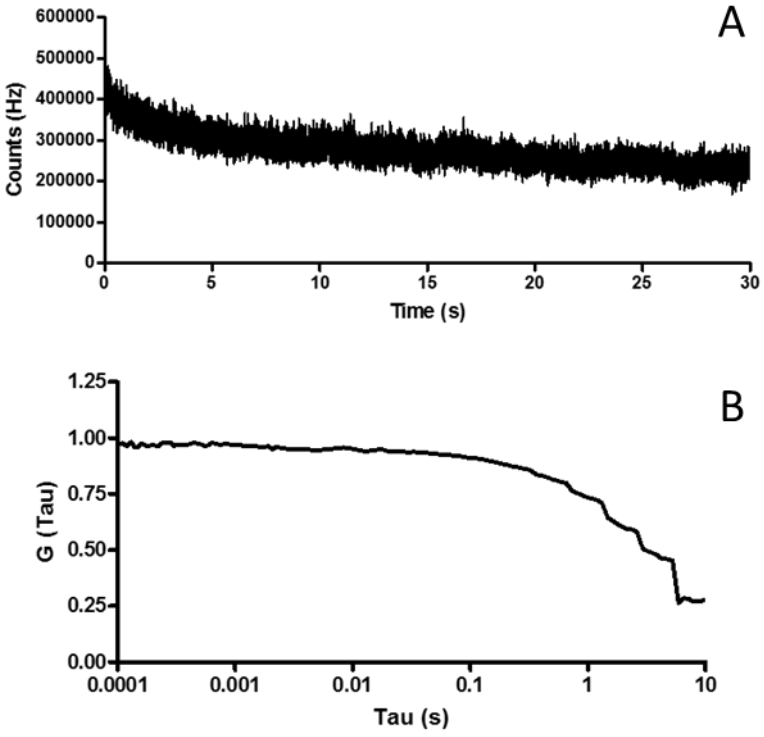

Figure 26 Average count rates during bleaching measurement (A) and the resulting FFS curve (B) which emphasizes the slow change in fluctuations due to bleaching instead of fluctuations due to protein diffusion.

Data Analysis

Raw fluctuation data was saved after measurement for each channel independently. Included in the hexadecimal code is the file identifier, measurement

identifier, position, kinetic index, repetition number, detector frequency, and the first pulse distance between detector clocks prior to measurement counts (209). From the raw data files, fluctuations were binned (50 μs) and the autocorrelation curve computed in Matlab as described in Equation 29.

$$G(\tau) = \frac{\langle \delta I(t) \delta I(t+\tau) \rangle}{\langle I(t) \rangle^2} = \frac{\langle I(t) I(t+\tau) \rangle}{\langle I(t) \rangle^2} - 1$$

Equation 29

The autocorrelation curve is then fit to determine the diffusion coefficient. Fluorescence fluctuation measurements in solution and the cytoplasm were fitted applying a standard 3D diffusion model.

$$G(\tau) = G(0) \frac{1}{\left(1 + \left({}^{\tau}/_{\tau_D}\right)\right)\left(1 + \left({}^{\omega_z}/_{\omega_{xy}}\right)^{-2} \left({}^{\tau}/_{\tau_D}\right)\right)^{1/2}} + G(\infty)$$

Equation 30

where ω denotes the beam dimensions. From the diffusion coefficient, τ_D, the diffusion rate can be determined.

$$\tau_D = \frac{\omega^2}{8D}$$

Equation 31

For membrane measurements, a two component 2D model was used to fit the data as detailed by Equation 32. The slow diffusion component describes the membrane molecules diffusing on a 2 dimensional plane formed by the membrane. The fast diffusion component is due to the excitation of fluorescent molecules in the cytoplasm

underneath the membrane. This component, while presented, was removed for further analysis since it does not describe membrane proteins.

$$G(\tau) = \frac{Af}{1 + {}^{\tau}/_{\tau_{D1}}} + \frac{A(1-f)}{1 + ({}^{\tau}/_{\tau_{D2}})}$$

Equation 32

To fit the measured autocorrelation curve, the least square curve fitting algorithm in Matlab was used. To determine protein interaction, the fluorescence cross-correlation component was determined, equation 33.

$$G_{CC} = \frac{G_{RG}}{G_G + G_R}$$

Equation 33

In addition to the cross-correlation, two component PCH was used to measure the heteromerization brightness component. Histograms of the fluctuations were formed by plotting the occurrence against the number of photon counts in each time bin. For a single particle excited by two-photon excitation, the PSF can be approximated by the square of a Gaussian-Lorentzian beam profile as define in equation 34 (148, 210) where I is the light intensity, I_o is the light intensity at the origin, and ω and z are the beam waist in the horizontal and axial directions, respectively.

$$\overline{PSF}_{2GL}(r,z) = \frac{I^2(r,z)}{I_o^2} = \frac{4w_o^2}{\pi^2\omega^4(z)} \exp\left[-\frac{4r^2}{\omega^2(z)}\right]$$

Equation 34

In Chapter 2, I showed the PCH for a single particle can be written as equation 35.

$$p^{(1)}(k; V_o, \varepsilon) = \frac{1}{V_o}\int_{V_o} Poi(n, \overline{\varepsilon PSF}(\vec{r}))\ d\vec{r}$$

Equation 35

Inserting equation 34 into 35, the PCH for a single particle in two-photon excitation can be determined (148) where γ is the incomplete gamma function.

$$p_{2GL}^{(1)}(k; V_o, \varepsilon) = \frac{1}{V_o}\frac{\pi^2 4w_o^2}{2\lambda k!}\int_0^\infty (1+x^2)\gamma\left(k, \frac{4\varepsilon}{\pi^2(1+x^2)^2}\right)dx$$

Equation 36

The experimental PCH is then fit to the convolution of the average number of single particles within the volume to determine the molecular brightness. The heteromerization brightness, two-color brightness, is determined by equation 37 (132).

$$\langle \varepsilon_{gr} \rangle = \frac{\sigma_{gr}^2}{\gamma\sqrt{\langle I_g \rangle \langle I_r \rangle}}$$

Equation 37

Constructs

Many of the constructs used in this work were combinations of plasmids. Below, I will detail the changes I have made to the major plasmids used to transfect cells in this study. There were multiple constructs which did not produce a functional linkage of the protein of interest and fluorescent protein; these constructs are not discussed.

EGFP and mApple Bacterial Expression Plasmids

For measurements in solution, both EGFP and mApple pQe-9 bacterial expression plasmids were used to obtain purified fluorescent protein. The Qe9 vector has an N-terminus His_6-tag used for protein purification and a selected resistance for Ampicillin through the β-lactamase (bla) gene. Plasmids were transformed into BL21 (DE3) competent Escherichia coli (E.coli) and plated on luria broth (LB) + ampicillin agar plates for overnight incubation at 37 °C. A single colony was picked and grown overnight at 37 °C while shaking in 5mL of LB with 5 mg/ml carbenicillin, an ampicillin analog with higher stability. A glycerol stock was made and frozen at -80 °C to remove the need for transformation and plating for each growth. One milliliter of overnight culture is grown in 50mL LB for 2-4 hours at 37 °C while shaking until an OD_{600} is reached. The colonies were then induced with Isopropyl β-D-1-thiogalactopyranoside (IPTG) and grown for 12-15 hours at 37°C while shaking. Many protocols instruct this last overnight growth to be at room temperature; however, I found no change in the amount of EGFP obtained and a reduction in the amount of mApple obtained when this last growth period was at room temperature compared to 37°C. After incubation cells were pelleted and frozen overnight before a His-tagged purification with Ni-NTA beads was performed to obtain purified proteins.

EGFP and mApple Mammalian Expression Plasmids

EGFP and mApple mammalian expression plasmids were from Clontech N1 and C1 vectors which are resistant to kanamycin. Plasmids were transformed into DH5α E. coli for plasmid production. Colonies were selected and grown in 5mL volumes as done for the bacterial expression vectors described above. One milliliter of overnight culture

was placed into 50mL of LB with kanamycin and grown overnight at 37°C while shaking. The culture was then pelleted and a midi-prep kit protocol (Qiagen, Hilden, Germany) was used to obtain plasmid DNA. DNA was concentrated using ethanol precipitation and then re-suspended in distilled water to concentrations between 1,000-10,000 ng/mL, the required DNA concentration for electroporation. The protocol explained above for plasmid production was reproduced for all mammalian expression cultures for transfections.

EGFP DRD3

The dopamine receptor D3 (DRD3) labeled with EGFP on its N terminus was purchased from Addgene (Product Number 24098). The receptor is of human species and properly traffics to the membrane through the use of a nicotinic receptor α7 subunit signaling peptide (211, 212). The plasmid is of pCEP4 and is encoded for ampicillin resistance.

EGFP DRD2

The D2 dopamine receptor (DRD2) labeled with EGFP on its N terminus was purchased from Addgene (Product Number 24099). Like the D3 receptor, the D2 is of human species and is properly trafficked to the membrane with the use of a nicotinic receptor α7 subunit signaling peptide (211, 212). The plasmid is in a pcDNA3.1+/Hygro backbone and is encoded for ampicillin resistance.

mApple $G_{\gamma 2}$ Subunit

The guanine nucleotide binding protein gamma-2 ($G_{\gamma 2}$ or GNG2) was purchased as cDNA of mammalian origin from GE Life Sciences (product number MMM1013-

7513168) and placed into a mApple C1 vector from Clontech between the restriction sites NheI (592) and BsrGI (1323). This GNG2 sequence has been used in many previous studies and has been shown to pair with the $G_{\beta 1}$ subunit to form a $G_{\beta\gamma}$ complex (213–215). The plasmid encodes for kanamycin resistance.

mApple Linked to EGFP construct

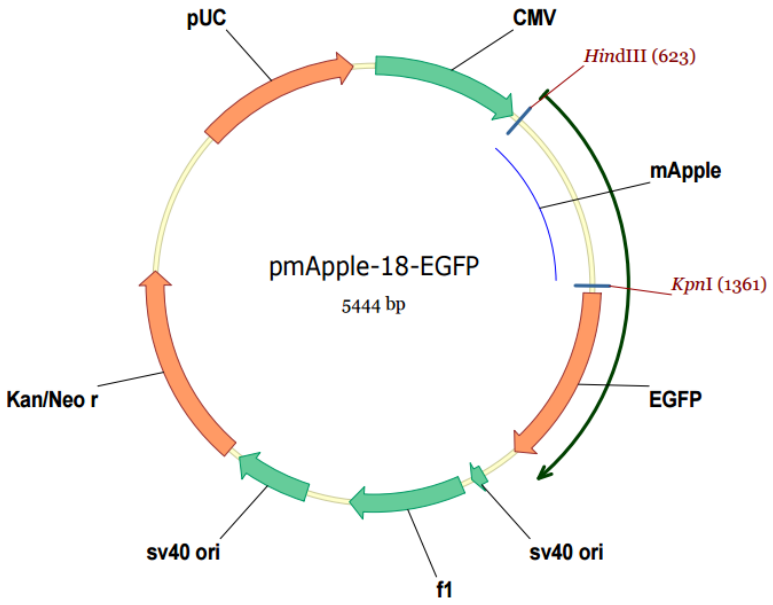

Figure 27 mApple-EGFP plasmid from mApple C1 inserted into an EGFP N1 vector. The resulting construct has 18 amino acids separating the two fluorescent proteins.

As a positive control for FFS studies of interacting proteins, I constructed a mApple-18aa-EGFP construct where mApple and EGFP formed linked together by 18 amino acids. PCR was used to amplify a mApple C1 insert between HindIII (623) and a KpnI restriction site added in the antisense primer (1361 added placement). EGFP N1 and the mApple insert were digested at the indicated restriction sites and then ligated with T4 DNA Ligase. A final plasmid map is shown in figure 27.

mCerulean $G_{\beta 1}$ Subunit

The guanine nucleotide binding protein beta-1 ($G_{\beta 1}$) subunit labeled with mCerulean at the N terminus was purchased from Addgene (product number 27810). This subunit is of human origination and has been well characterized to form functioning $G_{\beta\gamma}$ complexes with $G_{\gamma 2}$ (213–215).

EGFP G-protein Inwardly Rectifying Potassium Channel 3

The G-protein Inwardly Rectifying Potassium Channel subunit 3 (KCNJ9, Kir3.3, GIRK3) was purchased from OriGene (product number 004983) labeled with turbo green fluorescent protein (tGFP) on its C terminus. The vector is a pCMV6-AC-GFP with the GIRK3 subunit inserted between SgfI and MluI and encodes for ampicillin resistance.

mApple G-protein Inwardly Rectifying Potassium Channel 3

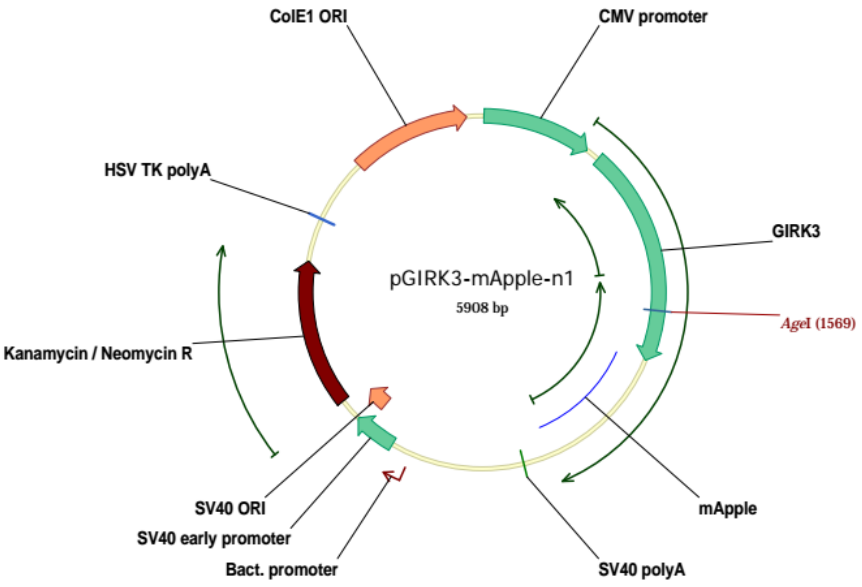

Figure 28 GIRK3-mApple plasmid map formed by performing an in-fusion HD cloning kit to insert the GIRK3 subunit into the mApple N1 vector linearized at the AgeI restriction site.

To measure interactions between the dopamine receptors and GIRK subunit, I used an in-fusion HD cloning kit to insert the GIRK subunit 3 sequence into a Clontech mApple N1 vector. For the reaction, the GIRK subunit was amplified by PCR and the mApple N1 vector linearized at the AgeI restriction site in the multiple cloning site. The final product formed was sequenced and its phenotype confirmed with a lambda scan, shown in Figure 28 with the full plasmid map.

Protein Characterization

As an initial experiment, FFS measurements of EGFP and mApple in solution were performed and their diffusion rates compared to those previously reported by FFS experiments. mApple measurements also characterized the diffusion rate and brightness of mApple which has not previously been used in two-photon FFS studies. The diffusion rates for EGFP and mApple in solution were determined to be 71.2 ± 7.7 $\mu m^2/s$ and 85.8 ± 15.8 $\mu m^2/s$, respectively. Results are shown in figure 29 along with the results from previous FFS studies of green and red fluorescent proteins in solution (216–218). The measured diffusion rates are in agreement with the expected values of proteins diffusing in solution.

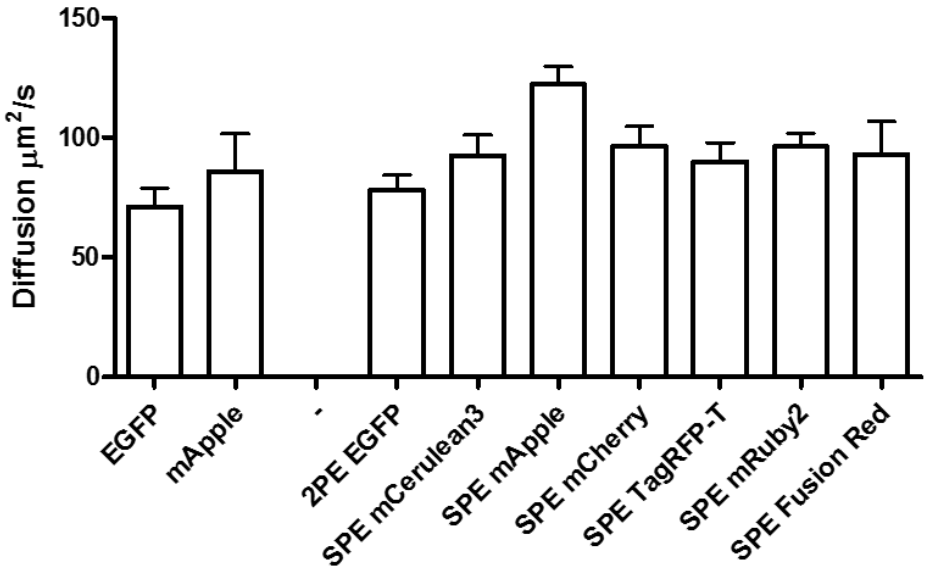

Figure 29 Comparison of diffusion rates determined for EGFP and mApple FPs versus those previously published (216–218)**. 2PE and SPE symbolize two-photon and single-photon excitation.**

EGFP and mApple N1 plasmids were also expressed in MIN6 cells as a control experiment to confirm the diffusion rate of FPs within the cytoplasm could be correctly measured. Diffusion rates for EGFP and mApple were determined to be 22.4 ± 3.9 $\mu m^2/s$ and 21.2 ± 4.8 $\mu m^2/s$, respectively. The results can be compared to previous reported diffusion rates from FFS in figure 30. Both the EGFP and mApple FPs diffuse within the expected diffusion rate of FPs in the cytoplasm.

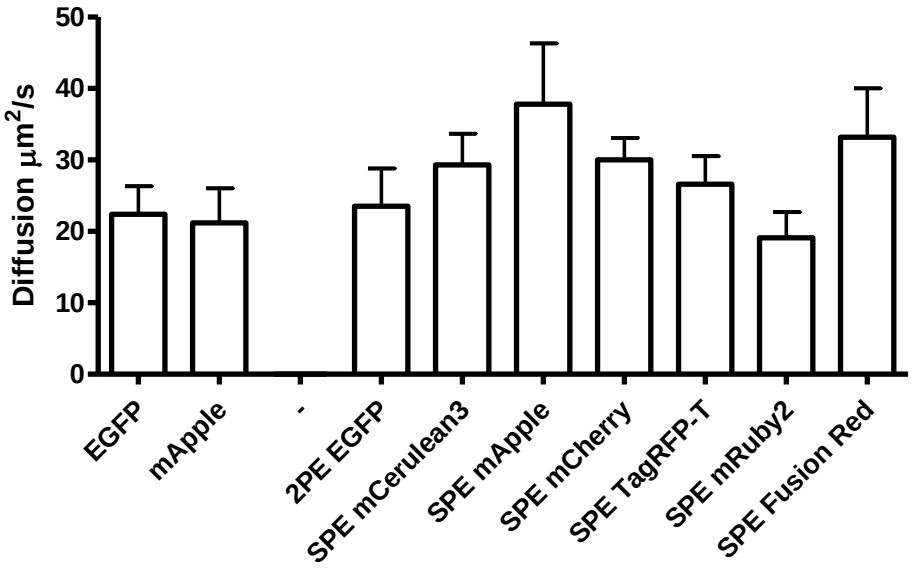

Figure 30 Diffusion rates of EGFP and mApple expressed within a cell versus previously published results of green and red FP diffusion rates in the cell.

As a control experiment to confirm the measurement of membrane proteins, two membrane proteins labeled with EGFP were measured in MIN6 cells and compared to previously reported diffusion rates of FRAP studies (194). The first of those proteins, transforming protein 21, or HRas, is an inner lipid protein used in signaling of the mitogen-activated protein kinases/extracellular signal-regulated kinases (MAPK/ERK) pathways (219, 220). HRas is similar to the G_{γ} subunit in that both are small, inner lipid proteins. The second control protein is VSVG3, a non-raft, transmembrane protein. FFS studies resulted in a diffusion rate of 0.90 ± 0.30 µm^2/s for HRas and 0.34 ± 0.13 µm^2/s for VSVG3, comparable to those found by FRAP (1.1 ± 0.40 µm^2/s and 0.2 ± 0.10 µm^2/s, respectively) as shown in figure 31 (194). Thus, the diffusion rates of membrane bound and transmembrane proteins were properly measured by FFS.

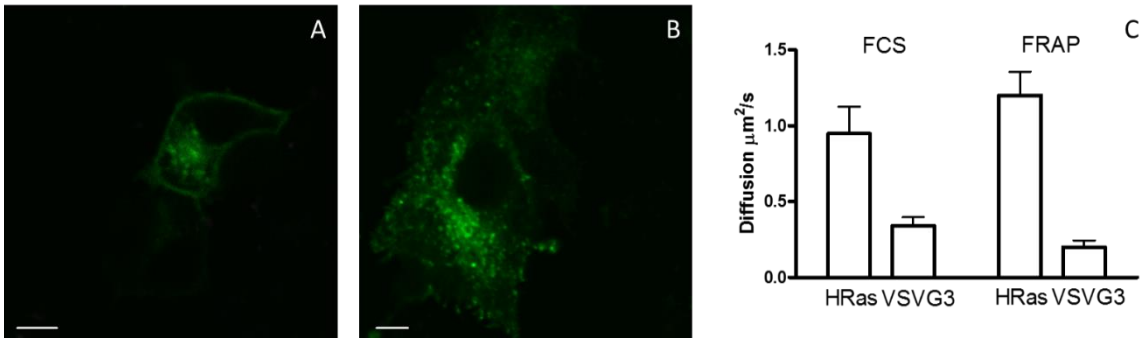

Figure 31 Raster fluorescence image of HRas (A) and VSVG3 (B) tagged with EGFP; scale bar 5 μm. Diffusion rates determined by FFS are 0.90 ± 0.30 μm^2/s for HRas and 0.34 ± 0.13 μm^2/s for VSVG3 compared to 1.2 ± 0.35 μm^2/s and 0.2 ± 0.10 μm^2/s for HRas and VSVG3 diffusion rates determined by FRAP (194) **(C).**

Summary

Detailed in this chapter are the methodologies used for this dissertation and background studies required before performing the experiments later detailed. As described above, it is essential the instrument is set up and aligned properly in order to correctly measure fluctuations for the determination of diffusion rates and heteromerization of proteins. All constructs used in the experiments of this dissertation have also been described in full detail and plasmid maps provided for altered plasmids. Thus far, I have shown the ability to measure the diffusion rates of EGFP and mApple with two-photon excitation in solution and within the cell. Due to the slow diffusion rate of membrane proteins, I used FFS measurements to determine the diffusion rates of an inner-leaflet and transmembrane protein. Results were comparable to those determined by fluorescence recovery after photobleaching (FRAP).

CHAPTER 4

DOPAMINE RECEPTOR SIGNALING THROUGH $G_{\beta\gamma}$ COMPLEX

Introduction

This chapter summarizes my studies of the signaling response by the dopamine receptor to the $G_{\beta\gamma}$ complex, after stimulation. It has been shown that circulating L-dopa is taken up by the β-cells, converted into dopamine, and co-secreted with insulin (120, 121). In the presence of dopamine, $[Ca^{2+}]_i$ is reduced, leading to decreased insulin secretion (120). This dopamine mediated negative feedback pathway regulates glucose stimulated insulin secretion (GSIS). Previous papers report the inhibition of GSIS by dopamine due to the D2 dopamine receptor subtype (120, 121, 221). However, in the presence of a D3 selective antagonist, insulin secretion is uninhibited while in the presence of a D2 selective antagonist, insulin secretion is predominantly inhibited (120). I hypothesize that the secreted dopamine is detected primarily by the dopamine receptor D3 subtype (DRD3), even though both the DRD2 and DRD3 subtypes are expressed in β-cells (120). Activation of the dopamine receptor leads to decreased $[Ca^{2+}]_i$, but the signaling pathway(s) from the receptor(s) to calcium activity remains unknown. It was shown that adenylyl cyclase activity in β-cells is largely unchanged by dopamine stimulation (221), so I expect DRD3 to signal through release of the $G_{\beta\gamma}$ complex. To explore this pathway and determine which receptor is involved in the dopamine mediated negative feedback pathway, I want to examine the interaction dynamics of the D3 and D2 dopamine receptors and the $G_{\beta\gamma}$ complex.

Recent FFS studies have investigated membrane proteins to measure signaling, disassociation constants, and clustering (222–226). I have used two-color FFS to examine the specific activation of dopamine receptor sub-types in a pancreatic β-cell model. Both cross-correlation and 2 component photon counting histogram analyses are applied to determine the dynamics of interactions between the DRD2 and DRD3 receptors with their heterotrimeric G-proteins. I show that both analysis methods yield the same results, which gives an internally consistent cross-check to the results.

Materials and Methods

Constructs and Cells

Enhanced green fluorescent protein (EGFP) and monomeric apple fluorescent protein (mApple) were expressed in MIN6 cells using Clontech N1 and C1 vectors (Clontech, Mountain View, CA). For control experiments, mApple C1 was inserted into the EGFP N1 vector to form a linked mApple –EGFP construct with 18 amino acids separating the two proteins, as described in chapter 3. EGFP-DRD3(211)**,** EGFP-DRD2 (211), and $G_{\beta 1}$-mCerulean(227) were obtained from Addgene (Cambridge, MA). The guanine nucleotide-binding protein subunit gamma-2 ($G_{\gamma 2}$) cDNA was obtained from GE Lifesciences (Pittsburgh, PA) and inserted into the multiple cloning site of a mApple C1 vector (Clontech, Mountainview, CA) as further described in chapter 3.

Transient transfections were performed on MIN6 β-cells (196) by electroporation using an Electro Square Porator ECM 830 (BTX, Holliston, MA) as detailed in Chapter 3. For FFS data acquisition, the cell media was replace with Krebs-Ringer Bicarbonate buffer containing 1% BSA and 12 mM glucose. Cells were warmed with an objective

heater maintained at 37 ºC. For some measurements, 100 µM of dopamine hydrochloride (Sigma-Aldrich, St. Louis, Missouri) was dissolved in the imaging buffer.

Instrumentation

Images and fluctuation measurements were performed on a LSM 780 using a 40X NA 1.2 C-Apochromat water immersion objective lens (Carl Zeiss, Jena, Germany). Fluorescence was excited with a Chameleon Ultra Ti:Sapphire laser (Cohernet, Santa Clara, CA) running at 1000nm to provide a single excitation volume for both green and red channels. Emission from GFP was collected between 500-540 nm and from mApple between 600-700 nm. The waist, ω_o, of the excitation volume was determined to be 270±10 nm by measuring 100 nm fluorescent beads. To determine the expression of cerulean, fluorescence was collected using an excitation wavelength of 850 nm.

Signal levels below one thousand counts per second were determined to be the baseline of autofluorescence. Typical FFS measurement of FP expression was between 10 to 50 thousand counts per second. A Z-scan of 0.1 µm steps was used to center the excitation volume at the cell membrane. FFS measurements were taken for 45 seconds, and the first measurement at each position was removed to exclude initial bleaching of immobile labeled proteins (175).

Theory and Data Analysis

Fluorescence fluctuation measurements in the cytosol were fit to a standard 3D diffusion model. For membrane measurements, a two component 2D model was used to fit the data. The results of the fast diffusion rate are shown, but these rates are not

consistent with the diffusion of membrane-bound constituents. Thus, the slow component was used for further analysis as this represents the membrane bound proteins. To determine protein interactions, the fluorescence cross-correlation component was determined (131, 228). In a parallel analysis of the raw FFS data, two-component photon counting histogram (PCH) analysis was used to evaluate the hetermoerized brightness component (132, 134). An un-paired t-test was used to determine significant differences (GraphPad Prism, La Jolla, CA), and p-values less than .05 were considered significant.

Cell images were acquired using the ZEN software (Carl Zeiss, Jena, Germany). Fitting and cross-correlation data analysis was performed using in-house written MATLAB programs (Mathworks, Natick, MA). Two-component PCH analysis was performed in ImageJ (NIH, Bethesda, MD) using a java script code modified for two-photon excitation volumes from Jay Unruh's source code (Stowers Institute, Kansas City, MO). All graphs and data reported show mean ± standard error of the mean.

Two-color FFS of Separate and Linked Fluorescent Proteins

To validate my measurements and analysis of the fluorescent protein labels used in these experiments, I first expressed each fluorescent protein label alone into MIN6 cells and measured the fluorescence fluctuations in the cytosol of cells within the sufficiently low expression level required for fluorescence correlation measurements. For the enhanced green fluorescent protein (EGFP), a single species fit resulted in a measured diffusion rate of 22.4 ± 3.9 $\mu m^2/s$, comparable with previous reported studies (216). mApple has not previously been used for two-photon excitation FFS studies, but

its diffusion rate is expected to be equivalent to those of EGFP and other fluorescent proteins. For mApple, the single species fits yields a diffusion rate of 21.2 ± 4.8 $\mu m^2/s$, in agreement with other fluorescent proteins (216, 217).

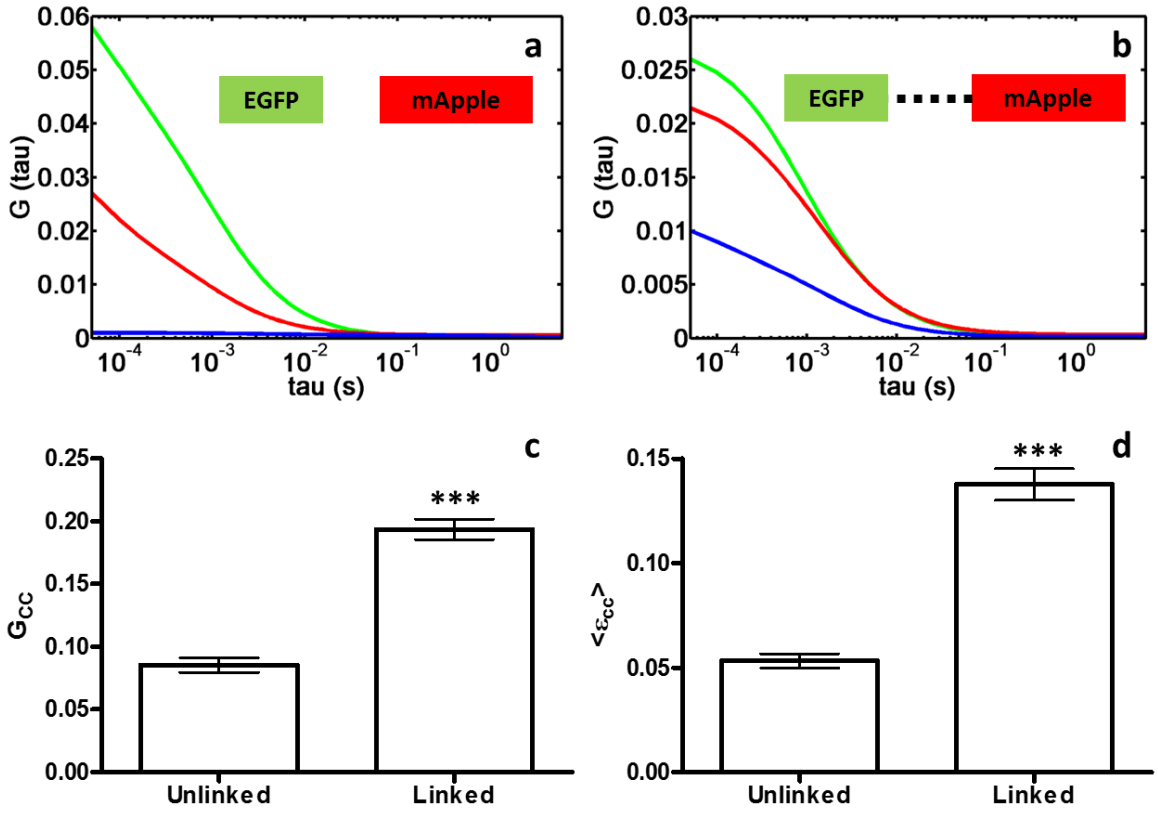

Figure 32 a. Autocorrelation curves from cells expressing separate EGFP (green) and mApple (red), and their cross-correlation (blue). b. Autocorrelation curves from cells expressing a linked EGFP (green)/mApple (red), with their cross-correlation (blue). Cross-correlation analysis (c) and two-component photon counting histogram analysis (d) quantifies the interaction of the unlinked and linked fluorescent proteins.

To establish the baseline cross-correlation between non-interacting proteins, separate EGFP and mApple plasmids were co-transfected into MIN6 cells. Two-color FFS measurements were acquired from the cytosol and the cross-correlation curve was calculated (Figure 32a). After fitting of the autocorrelation and cross-correlation curves, the interaction value, G_{cc}, was calculated. This interaction was verified by a parallel

two-component photon counting histogram analysis of the same original FFS data to determine a heteromerization brightness component, $<\varepsilon_{cc}>$ (Figure 32c,d).

To determine the maximal correlation between two fully interacting proteins, a plasmid was developed linking the two fluorescent proteins, EGFP and mApple, together with an 18 amino acid linker. The plasmid was transfected into MIN6 cells and two-color FFS measurements were made from the cytosol (Figure 32b). A cross-correlation curve was computed and the interaction values, G_{cc} and $<\varepsilon_{cc}>$, were determined (Figure 32c,d), both giving a ~2.5 fold difference in correlation between the unlinked and linked constructs.

Two-color FFS of Integral Membrane and Membrane Associated Proteins

Single Component Diffusion of Dopamine D3 Receptor and G_{γ} Subunit

To verify that the labeled proteins exhibit proper expression patterns and plasma membrane diffusion rates, I analyzed the FFS data to produce autocorrelation curves for labeled DRD3 and the Gγ subunit (GNG2). As detailed below, the plasma membrane component diffusion rate was determined by fitting each curve. The calculated diffusion rates for both of these constructs are comparable to other trans-membrane and inner leaflet proteins analyzed by FRAP and/or FFS (194, 205–208).

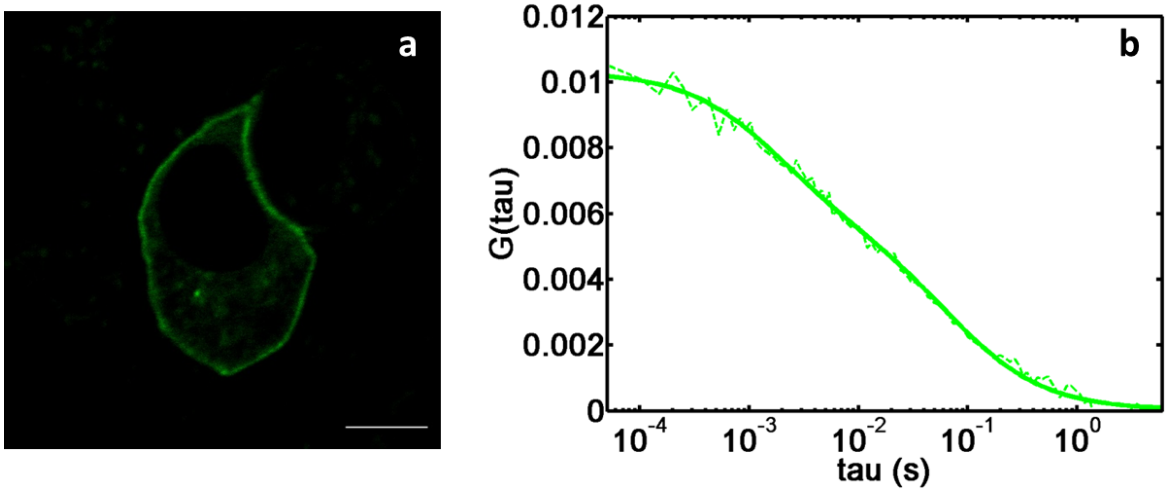

Figure 33 a. Fluorescence image of MIN6 cells expressing EGFP labeled DRD3 – both plasma membrane and intracellular labeling are visible. b. Experimental autocorrelation (dots) and two-component fit (solid line). Scale bar is 5 µm.

Two-photon fluorescence images of DRD3-EGFP were acquired to determine the expression patterns of the labeled protein (Figure 33a). The images show labeling both on the plasma membrane, and within the cytosol, putatively receptors located on intracellular membranes and recycling vesicles. FFS measurements were taken from a diffraction limited spot centered on the plasma membrane. A representative autocorrelation curve for DRD3-EGFP is presented in Figure 33b. Multiple algorithms were explored to fit the autocorrelation curve, including single component diffusion, two component diffusion, and single component diffusion with an anomalous component. The two-component model resulted in the lowest residual sum of squares, suggesting a faster moving intracellular component and a slower moving fraction on the plasma membrane. The slower diffusion rate of the plasma membrane, 0.120 ± 0.010 $\mu m^2/s$ component is in agreement with expected values (Figure 34). Upon stimulation with 100µM dopamine, I observed no protein expression changes in DRD3-EGFP, nor are

there any statistically significant differences in either its slow (0.108 ± 0.011 $\mu m^2/s$) or fast diffusion rates between before and after dopamine exposure (p-value of 0.4208).

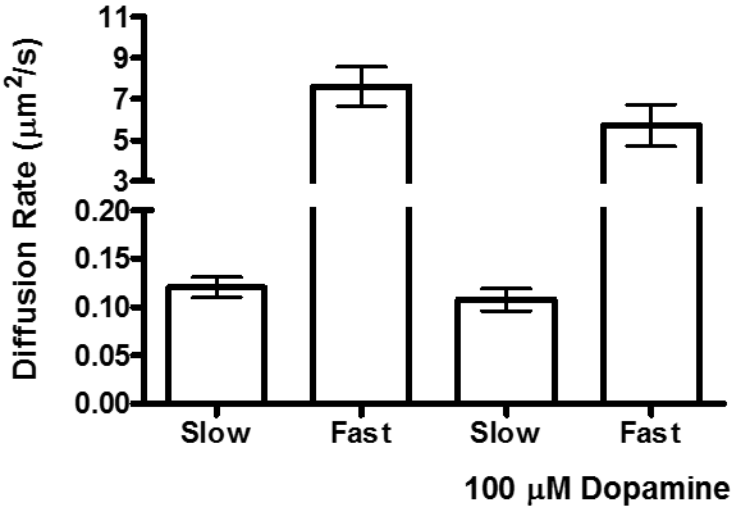

Figure 34 Calculated diffusion rates for EGFP-DRD3 before and after treatment with 100 μM dopamine (p = 0.4208).

The G_γ subunit is one part of the heterotrimeric G-protein complex, which is known to signal as a dimer with a G_β subunit (229). There is great promiscuity among the different G_β and G_γ subunits in the formation of dimers, and which complexes then form heterotrimeric G-proteins with different G-protein receptors. I chose to use the $G_{\gamma 2}$ subunit due to its previous characterization and use in similar studies (230, 231). The expressed G_γ subunit is expected to pair with intrinsic plasma membrane proteins in addition to the expressed DRD3.

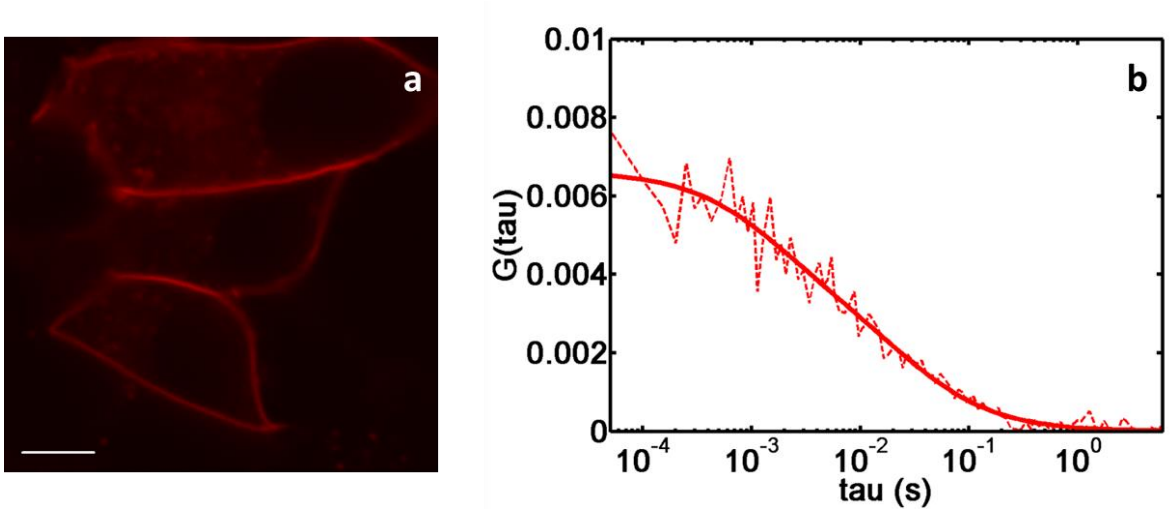

Figure 35 a. Fluorescence image of MIN6 cells expressing the mApple labeled G_γ subunit – predominantly plasma membrane labeling is seen. b. Experimental autocorrelation (dots) and two-component fit (solid line). Scale bar is 5 µm.

A representative fluorescence image of G_γ-mApple shows that the labeled subunits are largely membrane anchored, although a minor intracellular component is also observed (Figure 35a). Figure 35b shows an autocorrelation curve obtained from a membrane FFS point measurement of the G_γ subunit. A two-component fitting model was used to determine the diffusion rates. The slower diffusion rate determined for G_γ-mApple was 0.125 ± 0.016 $\mu m^2/s$, which as for DRD3-EGFP, is in agreement with previous studies of plasma membrane proteins. Since I expect the G_γ-mApple to be anchored to the plasma membrane, I did not expect to see significant changes in its diffusion upon dopamine stimulation, even if the G-proteins dissociate from the receptors. This was confirmed in the data as the slow diffusion component was determined to be 0.091 ± 0.014 $\mu m^2/s$ after dopamine stimulation (Figure 36). A t-test confirmed no statistical difference between the diffusion rates before and after treatment (p-value of 0.1195).

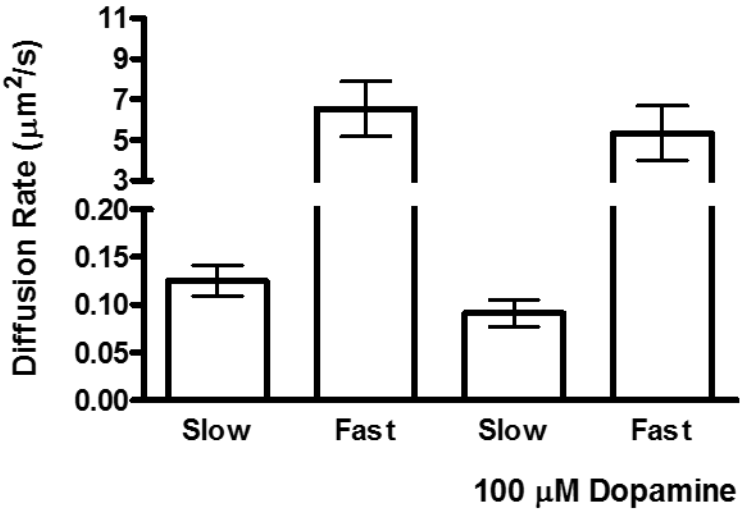

Figure 36 Calculated diffusion rates for mApple-G_γ subunit before and after treatment with 100 μM dopamine (p = 0.1195).

Two-color Fluorescent Fluctuation Measurements of DRD3 and G_γ

To examine the potential signaling consequences of dynamic interactions between DRD3 and $G_{\beta\gamma}$ complex, I co-expressed the fluorescently-tagged DRD3 and G_γ subunit. Interactions between the dopamine receptor and the G_γ subunit were assayed by acquiring simultaneous two-color FFS measurements from a diffraction limited spot centered on the plasma membrane. Two-photon fluorescence images of the two co-expressed proteins (Figure 37a-c) show similar expression patterns to what is seen with each component expressed separately (Figure 33a, 35a).

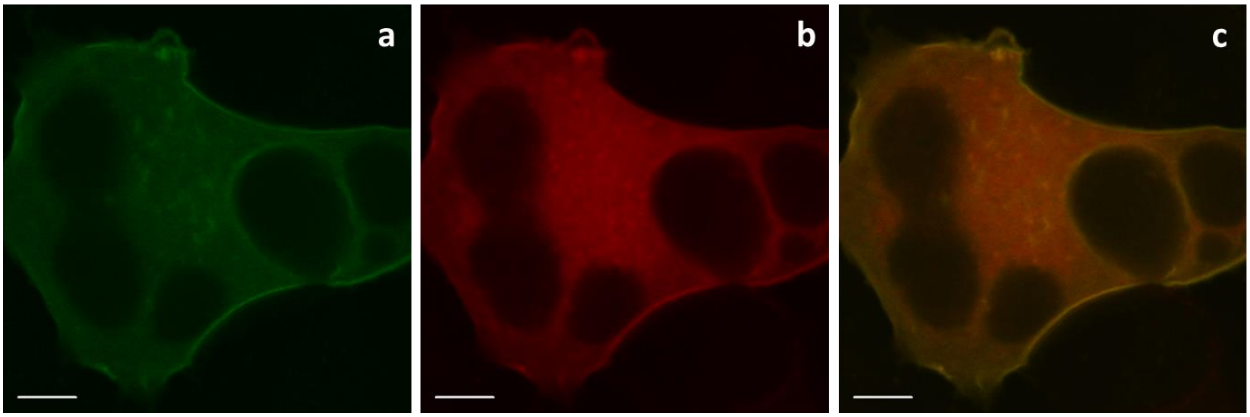

Figure 37 Fluorescence images of MIN6 cells expressing EGFP-DRD3 (a), mApple-G_{γ} (b), and their overlay (c).

Representative cross-correlation curves reveal minimal interaction between the DRD3-EGFP and G_{γ}-mApple both before and after dopamine treatment (Figure 38a,b). The cross-correlation was determined to be 0.069 ± 0.011 without dopamine and 0.074 ± 0.007 with 100 µM dopamine treatment (Figure 38c). A t-test revealed no statistical difference between the means of the cross-correlation component before and after treatment (p-value of 0.7287). Using the parallel heteromerization brightness analysis, the interacting component was found to be 0.043 ± 0.006 before, and 0.032 ± 0.003 after, 100 µM dopamine treatment (Figure 38d). Similar as for the cross-correlation component, a t-test found no statistical difference between the two means of the brightness component before and after treatment (p-value of 0.0522). This data was not consistent with the hypothesis that dissociation of the $G_{\beta\gamma}$ subunit from the DRD3 plays an important role in dopamine inhibition of insulin secretion.

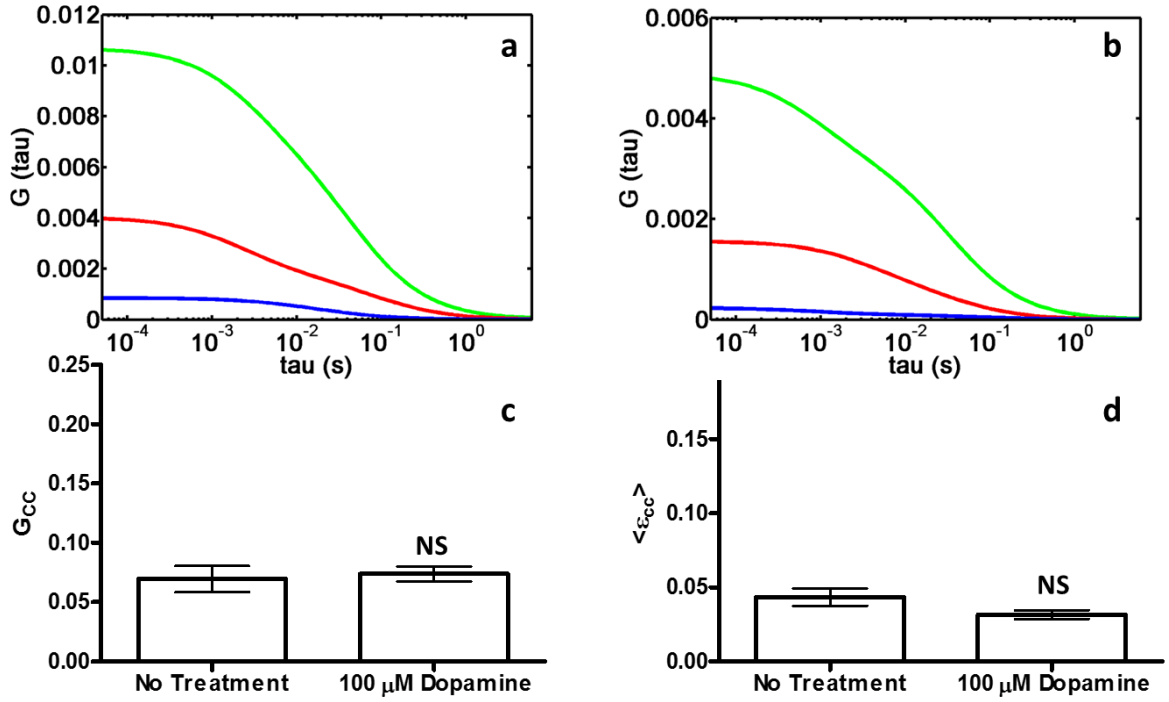

Figure 38 Autocorrelation curves of EGFP-DRD3 (green), mApple-Gγ (red), and their cross-correlation component (blue) before (a) and after (b) treatment with 100 μm dopamine. FFS cross-correlation (c) and heteromerization brightness analysis (d) before and after dopamine stimulation (p = 0.7287 and 0.0522, respectively). Scale bar is 5 μm.

Two-color Fluorescent Fluctuation Measurements of DRD3 and G_γ in the presence of G_β

Since we know that dopamine activates DRD3 in β cells, I suspected that the lack of a measured change in the interactions between DRD3-EGFP and G_γ-mApple might result from a lack of sufficient numbers of G_β subunits to form $G_{\beta\gamma}$ complexes with the overexpressed G_γ subunits. To investigate this possibility, I co-expressed a mCerulean labeled G-protein β subunit ($G_{\beta1}$) with the labeled DRD3 and G_γ subunit. Previous studies have shown proper pairing of the $G_{\gamma2}$ and $G_{\beta1}$ subunits (213–215). The mCerulean fluorescent protein is not excited by two-photon excitation at 1000 nm (Figure 39a,b), which permits the two-color FFS experiments with DRD3-EGFP and G_γ-

mApple to be performed without interference from the mCerulean fluorescence. Expression of $G_{\beta 1}$-cerulean was detected by fluorescence imaging with two-photon excitation at 850 nm (Figure 39c,d). The resulting fluorescence spectrum (232) of a region of interest along the plasma membrane (Figure 8e) reveals the mCerulean emission as a shoulder around 470 nm that is not present with EGFP alone (Figure 39e). No changes in localization of the DRD3-EGFP or G_{γ}-mApple proteins are observed after addition of the third transfected protein (Figure 39a-d).

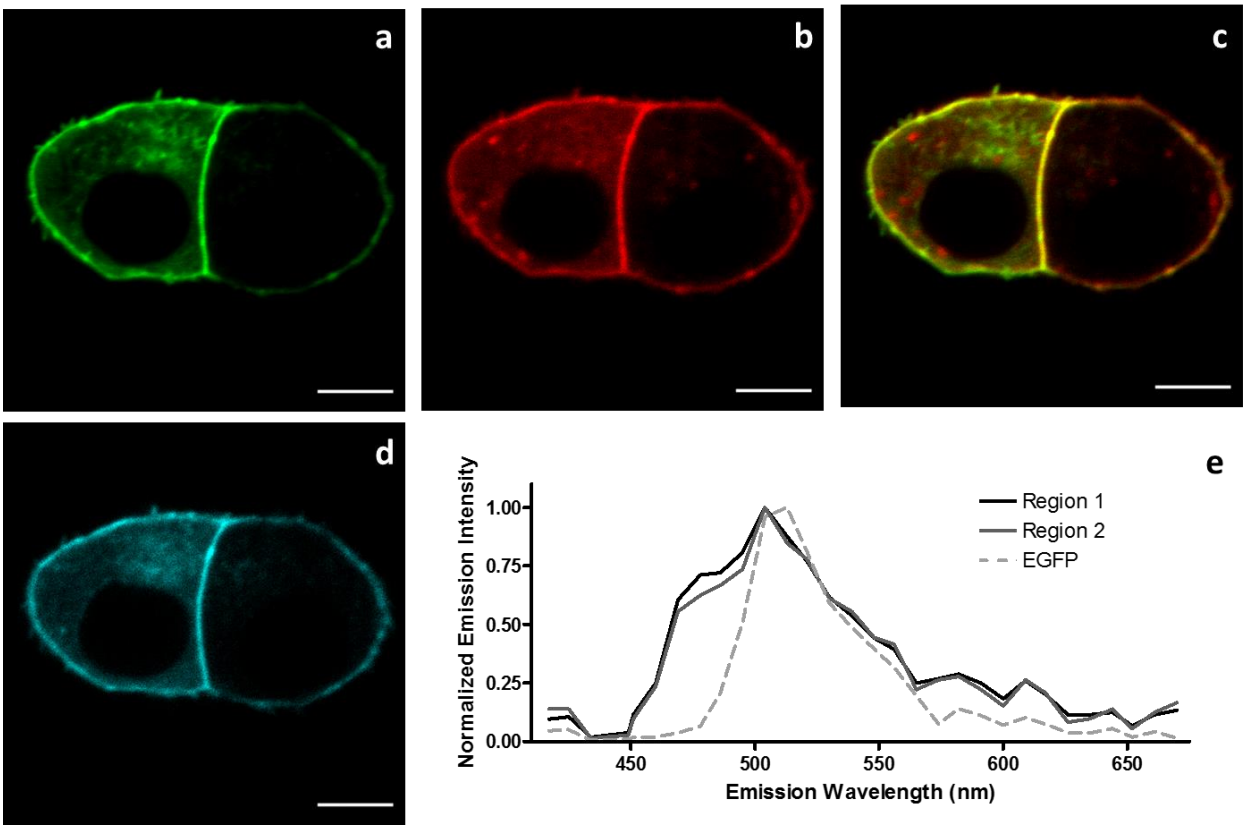

Figure 39 Fluorescence images of MIN6 cells expressing EGFP-DRD3 (a), mApple-Gγ (b), mCerulean-Gβ (c), and the overlay of EGFP-DRD3 and mApple-Gγ (d). e. Emission spectra (850 nm excitation) of the plasma membrane region of a triply-transfected cell confirms expression of mCerulean-Gβ (fluorescence in the 450-490 nm range). The emission spectrum of EGFP is shown for reference. Scale bar is 5 µm.

FFS measurements were taken from diffraction limited spots centered along the plasma membrane. The autocorrelation and cross-correlation curves were calculated (Figure 40a,b), and interactions between DRD3 and the G_γ subunit were analyzed with two-color fluorescence cross-correlation analysis (Figure 40c). Cross-correlation values were found to be 0.118 ± 0.016 before treatment and 0.065 ± 0.005 after treatment with 100µM of dopamine (p-value of 0.0026). Similarly, the heteromerization brightness component was calculated to be 0.043 ± 0.006 before and 0.026 ± 0.003 after the dopamine treatment (Figure 40d; p-value of 0.0054). Both analyses are consistent with a significant reduction in the spatial association between the DRD3 and the G_γ subunit upon dopamine treatment.

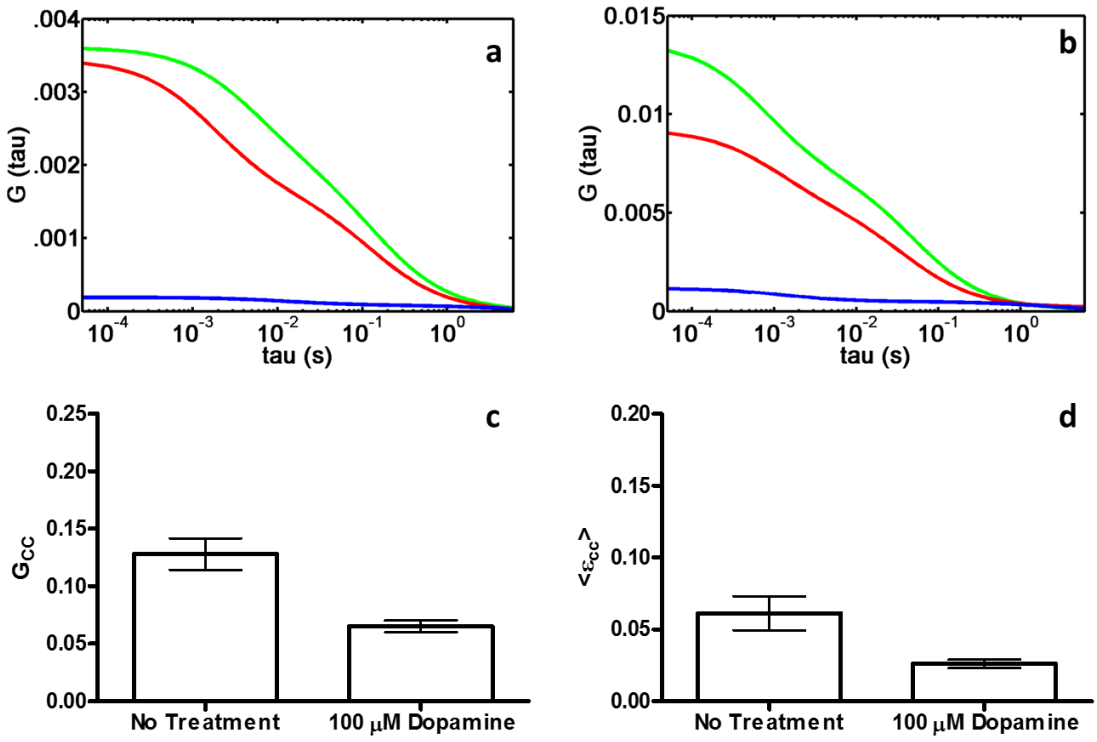

Figure 40 Autocorrelation curves of EGFP-DRD3 (green), mApple-Gγ (red), and their cross-correlation component (blue) in the presence of mCerulean-Gβ before (a) and after (b) treatment with 100 µM dopamine. FFS cross-correlation (c) and heteromerization brightness analysis (d) before and after dopamine stimulation (p = 0.0026 and 0.0054, respectively).

The data shows a low correlation and no significant dopamine-associated changes between DRD3 and the $G_{\beta\gamma}$ complex when I overexpress the fluorescently-labeled DRD3 and G_{γ} subunit (Figure 38). In this case, any $G_{\beta\gamma}$ complexes formed with the labeled G_{γ} subunit would have to be paired with the native G_{β} subunits. My data suggest that this does not permit sufficient incorporation of the labeled G_{γ} subunit into active $G_{\beta\gamma}$ complexes, as shown by relatively poor localization to the plasma membrane (Figure 37b) and low measured cross correlations (Figure 38c,d). This is consistent with previous findings that overexpression of only the G_{β} or G_{γ} subunit did not activate GIRK2 after stimulating the adenylyl cyclase receptor on oocytes (233). Upon the additional expression of the $G_{\beta 1}$ subunit, which is known to pair with the $G_{\gamma 2}$ subunit being used (213–215), I detected improved plasma membrane localization of the labeled G_{γ} subunit (Figure 39b), as well as higher heteromerization between labeled DRD3 and the $G_{\beta\gamma}$ complex (Figure 40c,d). The results suggest that it is important to overexpress all constituents of a functional complex for the extrinsic proteins to participate properly in the signal transduction pathway.

More than 40 different G-protein coupled receptors (GPCR) have been identified in the pancreatic β-cell, and it is expected that many of these receptors play important roles in the control of insulin secretion. Thus, $G_{\beta\gamma}$ complexes can associate and interact dynamically with a wide range of GPCRs, not only dopamine receptors. Additionally, the overexpressed $G_{\beta 1}$ and $G_{\gamma 2}$ can form complexes with other subunits native to the cell. This is consistent with my analysis, which yields cross-correlation amplitudes that are small compared to the autocorrelation values. This suggests that only a small number of the labeled proteins being within the interacting complexes, and is consistent

with the possibility that the labeled $G_{\beta\gamma}$ subunits are interacting with multiple GPCRs. Despite these potential obstacles, I still measured the coupling between labeled DRD3 and $G_{\beta\gamma}$ complexes (Figure 40). At baseline, there was a significant amount of heteromerization between DRD3 and the $G_{\beta\gamma}$ complex, and this interaction was reduced after stimulation by dopamine. This data is consistent with the hypothesis that DRD3 signaling depends on release of the $G_{\beta\gamma}$ subunit from the receptor following dopamine stimulation.

Two-color Fluorescent Fluctuation Measurements of DRD2 and Gγ

Previous evidence suggests that dopamine signals preferentially through DRD3 in β-cells, even though both DRD2 and DRD3 subtypes are present in the cells. Thus, I examined whether dopamine-stimulated changes between DRD2 and the G_{γ} subunit are different than those measured for DRD3. I performed FFS measurements between the DRD2 receptor and $G_{\beta\gamma}$ complex using an EGFP labeled DRD2, with the same G_{γ}-mApple and G_{β}-mCerulean. The localization of DRD2, G_{γ} subunit, and G_{β} subunit expression was predominantly on the plasma membrane with some intracellular signal, similar to the results for DRD3 (Figure 41a-d).

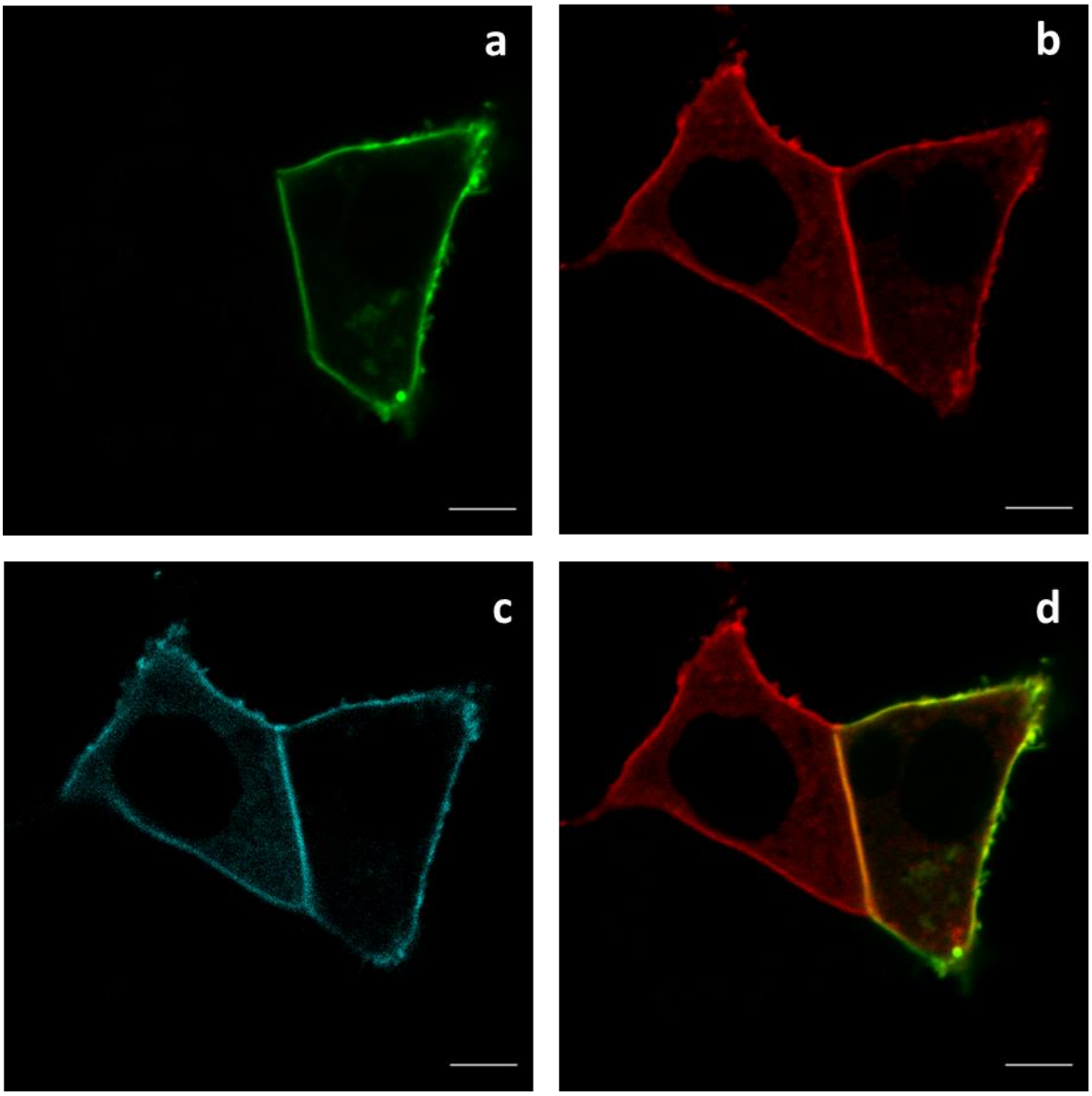

Figure 41 Fluorescence images of MIN6 cells expressing EGFP-DRD2 (a), mApple-G_{γ} (b), mCerulean-G_{β} (c), and the overlay of EGFP-DRD2 and mApple-G_{γ} (d). Scale bar is 5 µm.

FFS measurements were performed at the membrane of cells properly expressing all three labeled proteins. Autocorrelation and cross-correlation curves were computed from the measured fluctuations (Figure 42a,b). Cross-correlation values were determined to be 0.075 ± 0.008 before treatment and 0.058 ± 0.005 after

treatment with 100μM dopamine (Figure 42c; p-value of 0.0702). The heteromerization brightness components were determined to be 0.028 ± 0.003 before and 0.030 ± 0.002 after the dopamine treatment (Figure 42d; p-value of 0.6289). Unlike the results for DRD3 association, the FFS correlation between DRD2 and the G_γ subunit appears to be much less at baseline, and shows no statistically significant change upon dopamine stimulation.

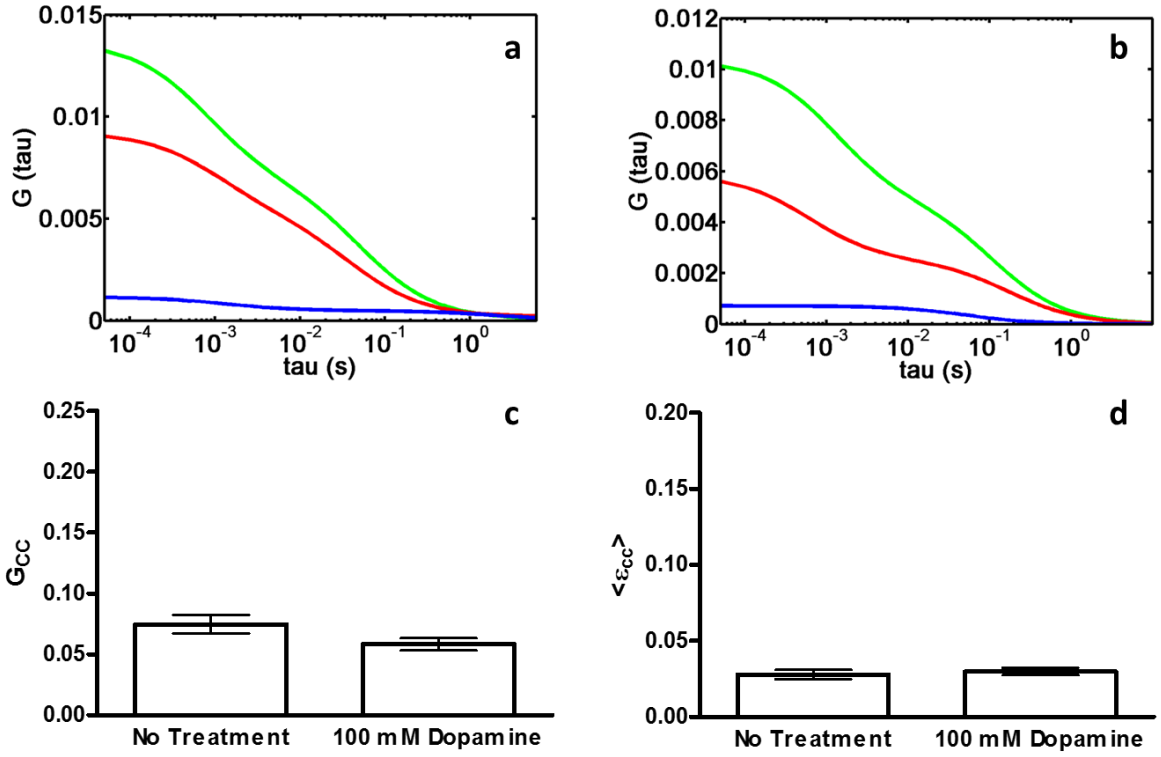

Figure 42 Autocorrelation curves of EGFP-DRD2 (green), mApple-G_γ (red), and their cross-correlation component (blue) before (e) and after (f) treatment with 100 μm dopamine. FFS cross-correlation (g) and heteromerization brightness analysis (h) before and after dopamine stimulation (p= 0.0702 and 0.6289, respectively).

Previous work showed that dopamine inhibits the amplitude and frequency of $[Ca^{2+}]_i$ oscillations in islet β-cells, leading to reduced insulin secretion (120). That work also showed that dopamine signaling in β-cells is primarily mediated by DRD3, even

though both DRD2 and DRD3 are known to be present (120). The results presented here suggest a possible solution to this dichotomy. The data shows significant heteromerization between DRD3 and the $G_{\beta\gamma}$ complex, and that this heteromerization is reduced in the presence of added dopamine (Figure 40). However, I did not find significant changes in the heteromerization between DRD2 receptor and the $G_{\beta\gamma}$ complex after dopamine treatment (Figure 42). Taken together, these data strongly support the hypothesis that the dopamine feedback loop inhibits insulin secretion primarily by stimulation of DRD3. The lack of dopamine-mediated changes in DRD2/$G_{\beta\gamma}$ complex interactions could be due to initially low levels of G-protein coupling to the DRD2. This would be consistent with the low cross-correlation and heteromerization brightness component values measured in my experiments. Another possibility could be that the DRD2 receptors are mainly sequestered away from the plasma membrane, and therefore would not be accessible to extrinsically added dopamine. This would be consistent with the findings of a previous paper that indicated the DRD2 expression was primarily within secretory granules (221). Further work would be needed to distinguish between these two possibilities, but the results presented here provide a framework for these and other future studies.

Summary

This chapter presents my study of interactions between the dopamine receptors and $G_{\beta\gamma}$ subunits using two-color FFS. Previous studies have used two photon excitation FFS cross-correlation to assay interactions between proteins labeled with EGFP and mCherry and monomeric red fluorescent protein (mRFP) (134, 217).

Because of its increased brightness over mCherry and mRFP, mApple is superior for FFS measurements (234). I showed signals from EGFP and mApple can be separated and used to measure dynamic heteromerization changes by FFS.

I next tested the hypothesis that the D3 receptor is activated by dopamine stimulation by measuring interactions between the D3 dopamine receptor and G_{γ} subunit. No changes were observed after dopamine stimulation which was inconsistent with the proposed hypothesis. To determine if overexpression of both the G_{β} and G_{γ} subunit was required to measure signaling, I additionally overexpressed the G_{β} subunit labeled with mCerulean which is not excited at 1000 nm, the excitation wavelength I used for FFS measurements. Upon the co-expression of G_{β} and G_{γ} subunits, I showed a reduction in heteromerization after dopamine treatment, confirming signaling through the D3 dopamine receptor. Next, I measured interactions between the D2 dopamine receptor and the $G_{\beta\gamma}$ complex after dopamine stimulation and showed no heteromerization changes. Thus, my results confirm the preferential signaling through the D3 dopamine receptor over the D2 dopamine receptor in the feedback pathway (120, 221).

In these studies, I utilized both fluorescence cross-correlation spectroscopy (FCCS) (141, 235) and two-component photon counting histogram (PCH) analysis (132, 236) methods to measure the interactions between dopamine receptors and their G-proteins. Previous biological studies of FFS have used only one analysis method or the other to examine the fluorescence fluctuations. Here I showed both analysis methods yield similar results, both in terms of baseline interactions and changes in heteromerization of the labeled proteins. Use of both analysis methods provides an

internally self-consistent check on the validity of the data and each separate analysis algorithm.

CHAPTER 5

GIRK INTERACTIONS WITH $G_{\beta\gamma}$ COMPLEX

Introduction

The material in this chapter focuses on the experiments I performed investigating interactions between the G-protein inwardly rectifying potassium channel (GIRK) and the $G_{\beta\gamma}$ complex. Once the D3 dopamine receptor is activated, $[Ca^{2+}]_i$ is reduced (120). Unpublished work by Dr. Jacobson and Dr. Ustione shows that hyperpolarization of the membrane after dopamine stimulation results from potassium channel activation other than the K_{ATP} channel. We hypothesize dopamine stimulation causes activation of GIRK by signaling through the $G_{\beta\gamma}$ complex of the G-proteins. In this model, movement of potassium out of the cell would result in plasma membrane hyperpolarization, causing voltage gated calcium channels to close. $[Ca^{2+}]_i$ would thus be reduced in the cell and insulin secretion inhibited. The proposed dopamine mediated negative feedback pathway is shown in figure 43. I hypothesized after dopamine stimulation, activation of GIRK channels by the $G_{\beta\gamma}$ complex would increase and therefore heteromerization would increase.

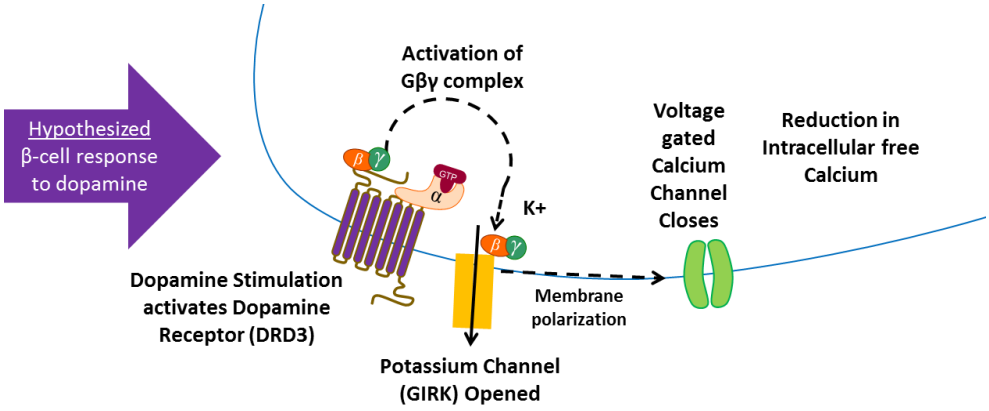

Figure 43 Proposed pathway for leading to decreased intracellular calcium and therefore decreased insulin secretion after stimulation with dopamine. Upon activation of the dopamine D3 receptor, the $G_{\beta\gamma}$ subunit activates G-protein inwardly rectifying potassium channels. The influx of potassium into the cell causes hyperpolarization of the membrane causing voltage gated calcium channels to close. The decreased calcium flux leads to a reduction in intracellular calcium, blocking insulin secretion.

GIRK channels, also known as Kir3, are members of the inwardly rectifying potassium channel family which includes Kir1-Kir7 (237). There are four GIRK subunits, GIRK1-4, also known as either Kir3.1-3.4 or KCNJ3, KCNJ6, KCNJ9, and KCNJ5, respectively. As identified by their name, GIRK channels are activated by G-proteins, specifically the $G_{\beta\gamma}$ complex. Functioning GIRK channels are tetramers of four GIRK subunits.). GIRK2 is the only subunit to form homotetramers (238, 239); however, all subunits form functional heterotetrameric channels in pairs (239–242). For example, two GIRK1 and two GIRK3 subunits form a functional GIRK channel. It has not yet been determined if functional channels are formed from three or four different type subunits (243). For the purposes in this work, GIRK3 was primarily studied due to its ability to form heterotetramers with all four other channels and the lack of splice variants found for it (240, 244, 245). By measuring GIRK3, a large number of GIRK channels can be examined with one overexpressed subunit. Most GIRK research to date has focused on

GIRK function in neural and cardiac pathways (246–248). In these pathways, multiple neurotransmitters including acetylcholine, adenosine, dopamine, serotonin, and somatostatin have been shown to activate GIRK channels through stimulation of their G-protein coupled receptors (249–252). Expression of GIRK subunits has also been shown in the pancreas and pancreatic cell lines (253–258). Iwanir determined the co-localization of all four GIRK subunits with insulin in pancreatic islets through immunolabeling and additionally, the presence of all four subunits in the insulinoma β cell line INS-1E (253).

Materials and Methods

Constructs and Cells

The turbo green fluorescent protein (tGFP) N terminus labeled GIRK3 subunit was purchased from Origene (MG205842, Rockville, MD). Multiple GIRK constructs were received from Tooraj Mirshahi at Geisinger Health System (Wilkes-Barre, PA) which are listed in Table 1 (259–261). The origination of the different subunits are varied; however, the proteins sequences are highly conserved.

Table 1 GIRK subunits with their tagged labels and origination of each sequence used in the experiments described in this chapter.

Subunit	*Label*	*Terminus*	*Origination*
GIRK1	Yellow Fluorescent Protein (YFP)	C	Human
GIRK2	Green Fluorescent Protein (GFP)	C	Mouse
GIRK4	Green Fluorescent Protein (GFP)	C	Rat
GIRK4	Cerulean Fluorescent Protein (CFP)	C	Rat
GIRK2	Human influenza hemagglutinin (HA)	C	Mouse
*GIRK3 *Origene*	EGFP	N	Mouse

In order to perform two-color FFS measurements between the EGFP labeled dopamine receptor D3 and the tGFP labeled GIRK3 subunits, a new construct of GIRK3 labeled with mApple was made with an in fusion HD kit (Clontech, Mountainview, CA). A further detailed description of the GIRK3-mApple is in Chapter 3.

Chemical transfections were performed with Effectene Transfection Reagent (Qiagen, Hilden, Germany). MIN6 cells were plated on glass bottom imaging dishes (Life Technologies, Carlsbad, CA) and incubated overnight to allow for recovery. Half a microgram of DNA was used for each plasmid and the effectene to DNA ratio was kept at 1:8. The amount of enhancer changed for the type of reaction and size of proteins involved. For EGFP-GIRK alone, 10µL, for EGFP-GIRK with the mApple labeled Gγ subunit, 20µL, and for mApple-GIRK and EGFP-DRD3, 30µL. Each 1mL effectene reaction was used to transfect one imaging dish. Typical expression incubation times were between 18-24 hours. After 48 hours, the expression levels were too high for FFS studies and cells were discarded. Electroporation transfections, used for two color measurements only, were performed using an Electro Square Porator ECM 830 (BTX, Holliston, MA) as detailed in Chapter 3.

For FFS data acquisition, the cell media was replace with Krebs-Ringer Bicarbonate buffer containing 1% BSA and 12 mM glucose. Cells were warmed with an objective heater maintained at 37 ºC. For some measurements, 100 µM of dopamine hydrochloride (Sigma-Aldrich, St. Louis, Missouri) was dissolved in the imaging buffer.

Instrumentation

Raster fluorescence images and fluctuation measurements were taken on a LSM 780 using a 40X NA 1.2 C-Aprochromat water immersion objective lens (Carl Zeiss,

Jena, Germany). Fluorescence was excited with a Chameleon Ultra Ti:Sapphire laser (Coherent, Santa Clara, CA) running at 1000nm to provide a single excitation volume for both green and red channels. Emission from GFP was collected between 500-540 nm and from mApple between 600-700 nm.

Data Analysis

Correlation curves were processed and fitted with MatLab programs and brightness analysis was performed with Java Script code in ImageJ, both described in Chapter 3.

Expression of GIRK Subunits

To verify expression, a raster fluorescence image was taken of a MIN6 cell expressing tGFP-GIRK3 (Figure 44). Two components are detectible, an intracellular component and a plasma membrane component. One hypothesis for the large intracellular component is that only a single subunit, GIRK3, was expressed. This subunit alone cannot form functional GIRK channels. Overexpressed GIRK3 can only form functional channels with native GIRK subunits in the cell. The transient transfection introduced considerably more GIRK3 subunits than the cell needs to form the necessary GIRK channels for signal transduction. When performing Z-scans, membrane location could be determined, but with increased difficulty due to the large intracellular component of the GIRK subunits.

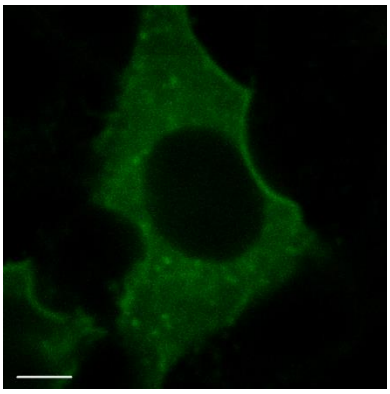

Figure 44 Two-photon excitation (1000 nm) raster fluorescence image of MIN6 cell expressing the turboGFP labeled GIRK3 subunit; A large intracellular component with a faint membrane outline can be seen to the upper right side of the cell; scale bar 5 μM

While all four GIRK subunit have been determined present in β cells, no consensus has been reached to the amounts of each subunit inherently in the cell, nor which GIRK channels are most often formed (253–258). Therefore, I decided to test the expression of each subunit transfected alone in MIN6 cells. The expression phenotypes for GIRK1, 2, and 4 are shown in figure 45. Both GIRK1 and GIRK2 have a high proportion of bright spots due to protein clustering, potentially due to endosomal compartments. However, only GIRK3 has a strong plasma membrane component that is easily distinguishable from the intracellular.

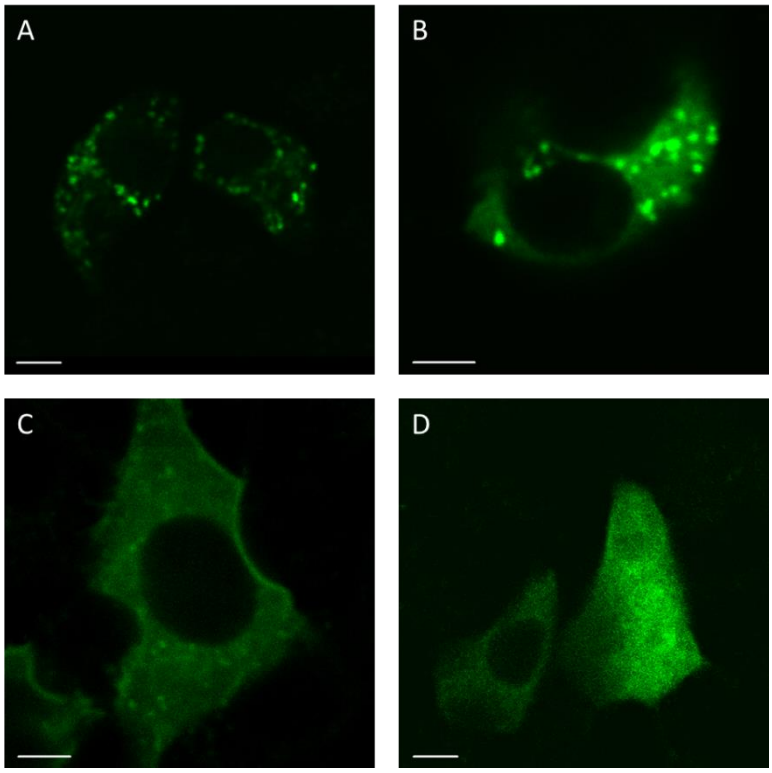

Figure 45 Representative raster fluorescence images of MIN6 cells expressing GIRK1-YFP (A), GIRK2-EGFP (B), tGFP-GIRK3 (C), and GIRK4-CFP. Both GIRK1 and GIRK 2 both exhibit clustering throughout the cytosol and no plasma membrane bound component.(A, B); tGFP-GIRK3 has small portions of membrane expression, but with a large intracellular component throughout the cell (C). GIRK4-CFP is distributed evenly throughout the cytosol with no plasma membrane component visible; scale bar 5 μM

Previous studies have shown that GIRK2 and GIRK3 form functional GIRK channels (241, 242). To increase the amount of GIRK2 in the cell for GIRK3 to pair with, I co-transfected GIRK2 labeled with an HA tag and GIRK3 labeled with a tGFP tag. Without a fluorescent label on the GIRK2 or the use of an anti-HA tag antibody, I was not able to determine which cells specifically expressed both subunits. A representative image of the co-transfection is shown in **Error! Reference source not found.**46; no cells exhibited a strong membrane component and cell rounding was present immediately when imaging started. In addition to the pairing of GIRK3 with GIRK2, I also tested the pairing of GIRK3 and GIRK4 to from functional channels at the

membrane. GIRK4 has been shown to be a critical subunit in the activation of GIRK channels in cardiac signaling (262, 263). Additionally, GIRK4 has been shown to be membrane localized when expressed alone and to support the transportation of other GIRK subunits to the membrane of oocytes (264). The co-expression of tGFP-GIRK3 and GIRK4-CFP however resulted in a large intracellular component and no clearly defined membrane region. Experiments characterizing GIRK3 at the membrane were performed as detailed in the next section. Due to the insufficient signal of GIRK3 at the membrane, only initial measurements between GIRK3 and G_{γ} were performed.

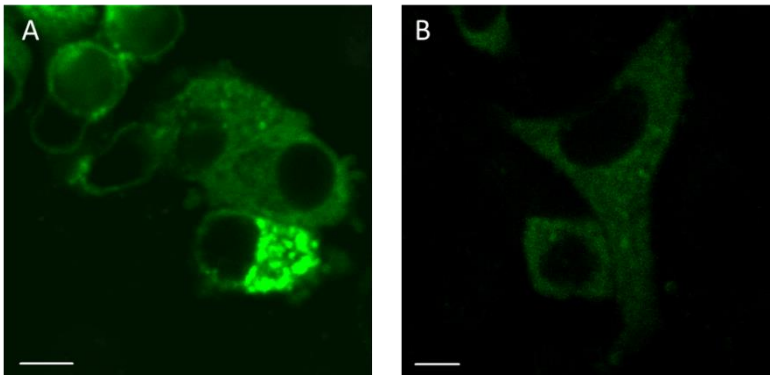

Figure 46 Representative raster fluorescence images of MIN6 cells expressing GIRK2-HA and tGFP-GIRK3 (A) and tGFP-GIRK3 and GIRK4-CFP (B); Co-expression of GIRK2-HA and tGFP-GIRK3 cells exhibit a membrane component, a large intracellular component, protein clustering, and cell rounding indicating unhealthy cells. Cells co-transfected with tGFP-GIRK3 and GIRK4-CFP result in expression throughout the cytosol with some clustering, but no plasma membrane bound component; scale bar 5 μM

Two-color FFS of Integral Membrane and Membrane Associated Proteins

Fluorescence Fluctuation Measurements of GIRK

Single color FFS measurements were taken at the membrane before and after treatment with 100μM of dopamine. As found for the dopamine receptor and $G_{\beta\gamma}$ complex, a two component model resulted in the lowest residual sum of squares, signifying it as the best fit to the data. The slow diffusion rate, representing the

membrane bound component, was determined to be 0.38 ± 0.09 $\mu m^2/s$ before and 0.21 ± 0.03 $\mu m^2/s$ after dopamine treatment. The fast intracellular component is 13.09 ± 1.51 $\mu m^2/s$ without dopamine and 11.46 ± 1.10 $\mu m^2/s$ with dopamine. A student t-test was performed and no statistical significance was determined between diffusion rates before and after dopamine treatment for either the slow or fast component as expected (p-value of 0.0752 and 0.3932, respectively).

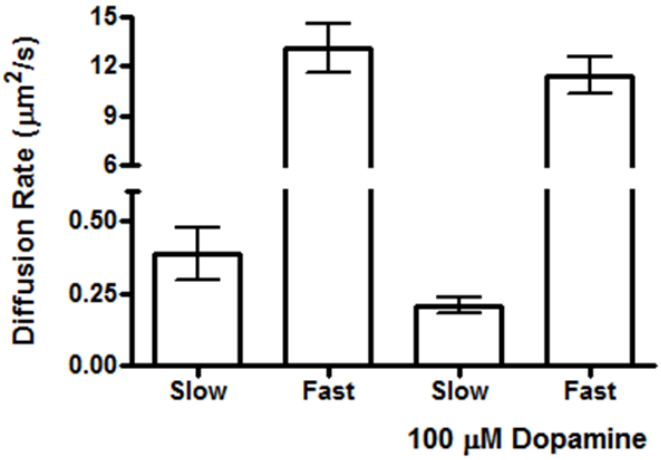

Figure 47 Calculated diffusion rates from two component fitting of tGFP-GIRK3 before and after treatment with 100μM dopamine. The slow diffusion rate represents the membrane bound component whereas the fast diffusion rate is due to the intracellular component. Unpaired t-test, p-value of 0.0752 and 0.3932 for the slow and fast diffusion rates, respectively.

Two-color FFS measurements between GIRK3 and G_γ subunit

To test the relationship between a GIRK channel including the GIRK3 subunit and the $G_{\beta\gamma}$ complex, tGFP-GIRK3 and mApple-G_γ were co-transfected into MIN6 cells. A representative raster fluorescence image is shown in figure 48. The mApple-G_γ is membrane bound while the tGFP-GIRK3 shows both a membrane and intracellular component. Two color FFS measurements were taken at the cell membrane and the autocorrelations and cross-correlation curves calculated. In my hypothesis, the $G_{\beta\gamma}$

complex activates GIRK channels so that an influx of K^+ enters the cell. If correct, heteromerization between the GIRK and $G_{\beta\gamma}$ complex would increase after dopamine treatment.

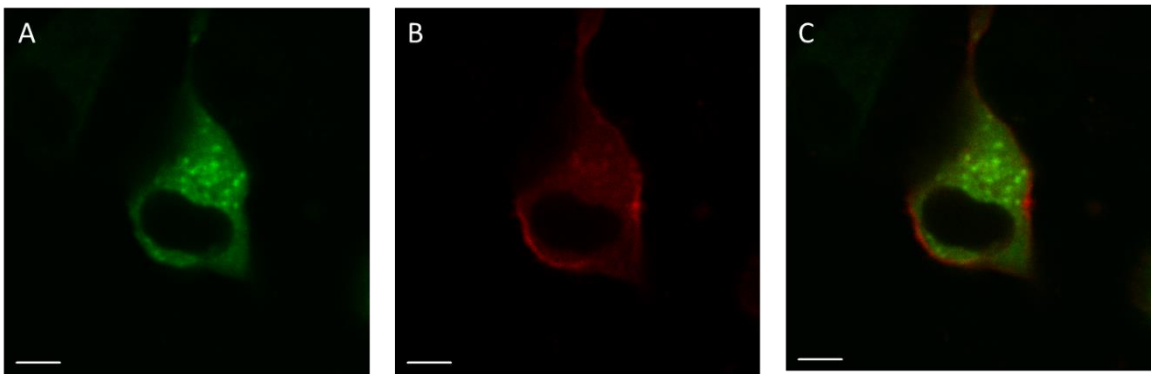

Figure 48 Representative raster fluorescence images of MIN6 cells co-transfected with tGFP-GIRK3 (A) and mApple-G_γ (B); merged (C). The expression of both labeled proteins is not altered by the co-transfection; scale bar 5 µM

Figure 49 shows two representative autocorrelation and cross-correlation curves between the labeled proteins for before (A) and after (B) dopamine. The horizontal slope and zero y-intercept show no correlation before or after treatment. Quantification of the cross-correlation (C) before and after dopamine treatment resulted in a G_{cc} of 0.046 ± 0.010 and 0.052 ± 0.013, respectively. An unpaired t-test resulted in a p-value of 0.7110 indicating no statistical significance between the means of the cross-correlation values. The heteromerization brightness component (D) results were in agreement with the cross-correlation results with a brightness component of 0.035 ± 0.007 and 0.031 ± 0.009, for no treatment and with 100µM dopamine treatment respectively. An unpaired t-test again resulted in no measurable statistical difference between the two means with a p-value of 0.7518.

These interaction analyses show no interaction between the GIRK3 and G_{γ} subunit. My data measuring interactions between the D3 dopamine receptor and $G_{\beta\gamma}$ complexes, in Chapter 4, suggest the G_{γ} subunit is not sufficiently incorporated with the G_{β} subunit unless both are overexpressed. To measure interaction between the $G_{\beta\gamma}$ complex and GIRK channel, both the G_{γ} subunit and G_{β} subunit may need to be transfected into the cell.

I selected GIRK3 for FFS measurements because it can form tetramers with all three other GIRK subunits to form functional channels allowing me to measure interactions between the $G_{\beta\gamma}$ complex and multiple GIRK channels in one experiment (240, 244, 245). If the $G_{\beta\gamma}$ complex signals to a GIRK channel not comprised of a GIRK3 subunit, no interaction will be measured before or after dopamine treatment. Furthermore, based on previous dopamine receptor studies, I hypothesize the dopamine receptor signals to a GIRK channel through the $G_{\beta\gamma}$ complex (250, 265, 266). If a different potassium channel (or calcium channel) is activated by the $G_{\beta\gamma}$ complex no heteromerization between any GIRK subunit and the $G_{\beta\gamma}$ complex would be measured.

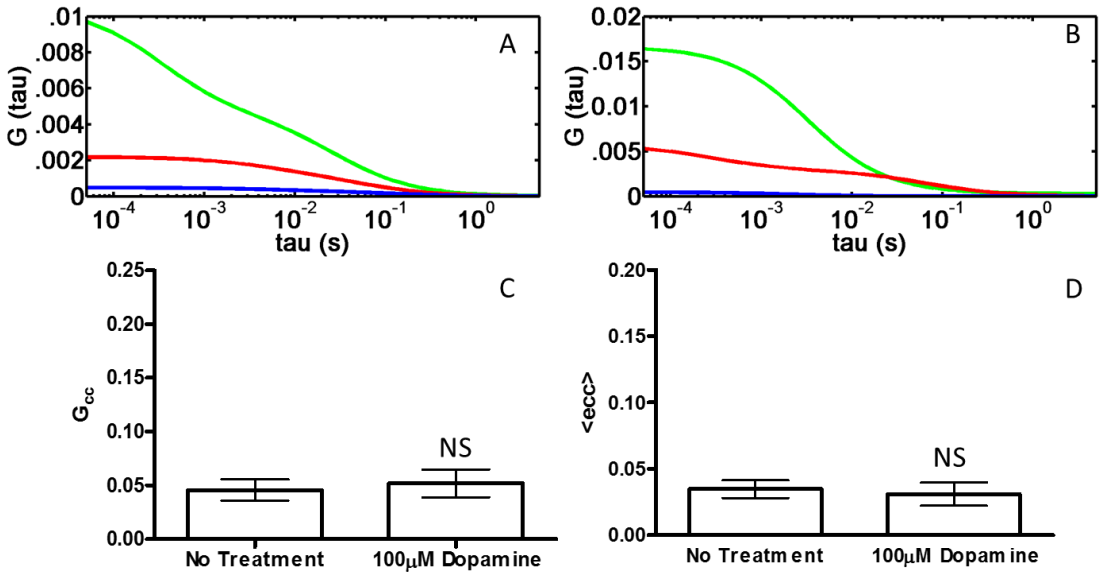

Figure 49 Autocorrelation curves of tGFP-GIRK3 (green), mApple-G_γ (red), and their cross-correlation component (blue) before (a) and after (b) treatment with 100 μM dopamine. FFS cross-correlation (c) and heteromerization brightness analysis (d) before and after dopamine stimulation (p = 0.7110 and 0.7518, respectively).

Two-color FFS measurements between GIRK3 and Dopamine Receptor D3

Recent literature has shown the co-localization of GPCRs with their target proteins to allow for quick and efficient signal transduction (267, 268). Relationships between the receptor and target protein can be difficult to detect with many standard protein interaction techniques since the proteins are not strongly bound to each other. FFS provides a method to study *in situ* the relationship between the D3 dopamine receptor and GIRK channels. To test the proximity of the D3 receptor and GIRK3 subunit, the EGFP labeled D3 dopamine receptor and mApple-GIRK3 were co-transfected into MIN6 cells. The goal of this experiment was to take FFS measurements to determine if the two proteins diffused together on the membrane for rapid signal transduction from the D3 receptor to the GIRK channel. If the two proteins diffuse

together, an increase in the correlation and brightness component between the two proteins would be observed, compared to that seen for two non-interacting membrane proteins. Figure 50 shows raster fluorescence images of MIN6 cells transfected with both labeled proteins. Cells with both expressed proteins show unhealthy vesicles and exhibited cell rounding. Changes in the amount of DNA used to transfect the cells, electroporation versus chemical transfections, and shorter incubation times after transfection before imaging did not increase the number of healthy cells. Cells that expressed only one plasmid had varying expression levels and proper attachment to the bottom of the glass dishes. Experiments between the D3 receptor and GIRK channel were not taken due to the inability to obtain properly expressing and healthy cells.

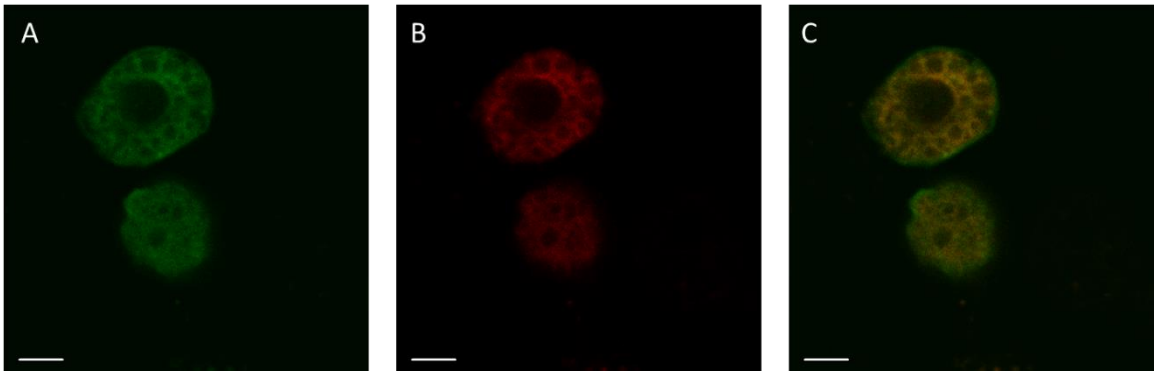

Figure 50 Representative raster fluorescence images of MIN6 cells co-transfected with EGFP-DRD3 (A) and mApple-GIRK3 (B); merged (C). The expression of both labeled proteins is altered by co-transfection. Cells exhibited cell rounding and protein clustering not present when expressed independently; scale bar 5 μM

Conclusion and Future Directions

GIRK Channel Membrane Trafficking Difficulties

Without clear expression of the tGFP-GIRK3 at the membrane, it is likely that improper trafficking of the channel is occurring. An intracellular component is expected to be present since GIRK3 is only a subunit of GIRK channels and cannot form

functional channels alone; the large amount of intracellular component was unanticipated. The intrinsic GIRK subunits within the cell have not been knocked down for these measurements and therefore the introduced tGFP-GIRK3 subunit was expected to form functional channels with the intrinsic subunits. In the oocyte model, Mirshahi et al. showed GIRK1 did not traffic to the membrane on its own, but needed the additional expression of GIRK4 to form functional GIRK channels at the membrane (264). The co-transfection of GIRK3 and GIRK4 however resulted in intracellular components of the two proteins, no large plasma membrane component. Co-transfections of GIRK2 and GIRK3, two subunits well studied to form functional tetramer channels, also showed no increased membrane localization of the channel subunits compared to GIRK3 alone (241, 242). To properly measure the interactions of GIRK at the membrane, it is essential for proper membrane localization to occur. Future experiments should begin with determining which GIRK subunits are properly trafficked to the membrane alone and with other subunit pairings. Reverse transcriptase polymerase chain reaction (RT-PCR) can be used to detect RNA expression of the GIRK subunits in MIN6 cells (253). Western and coimmunoprecipitation assays can then be used to detect pairings between subunits as previously performed for neural GIRK channels (241, 242). While GIRK1 and GIRK2 are known to pair with GIRK3 in the cell to form functional GIRK channels, there is reported variability with the current levels when the proteins are overexpressed into cells (241, 242, 269–271). The knowledge that splice variants exist for GIRK2 could be the result of this variability and therefore should be looked into when testing the co-expression with GIRK3 (240, 244, 245). Last, the GIRK1, GIRK2, and GIRK4 subunits obtained from Geisinger Health

System have all been co-expressed together in previously reported studies, but not with the GIRK3 subunit used here which was obtained separately. GIRK3 subunits from different originations should be tested to determine if the GIRK3 obtained does not properly couple with other GIRK subunits to form functioning channels.

Lack of Activation Measured between GIRK Channel and D3 Receptor

In measurements between the dopamine receptor and $G_{\beta\gamma}$ complex, it was necessary to express the G_{β} and G_{γ} subunits to obtain a signal. Thus, it is probable that to measure interaction between the GIRK channels and $G_{\beta\gamma}$ complex, both subunits in the $G_{\beta\gamma}$ complex must be expressed.

When measuring the heteromerization between GIRK3 and G_{γ} subunit, it was expected to find an increased cross-correlation and heteromerization brightness component after dopamine treatment, indicating that the $G_{\beta\gamma}$ complex activates the GIRK channel. The GIRK channel is G-protein gated and previous studies have shown activation of GIRK channels by the dopamine receptors (250, 265, 266). The lack of measured signaling could be the result of GIRKs not comprised of the GIRK3 subunit being activated by the dopamine receptor. GIRK3 was selected as it can form functional subunits with many different combinations of GIRKS, thus by selecting it a broad variety of channels could be sampled. GIRK1, GIRK2, and GIRK4 are all present in the β cell and comprise a minimum of four GIRK channels, not including splice variants, which are not sampled by labeling GIRK3 and thus should be studied further.

Expression Difficulties between GIRK Channel and D3 Receptor

Co-transfections of the mApple labeled GIRK3 and EGFP labeled D3 dopamine receptor did not produce healthy cells for which to take FFS measurements. Varying the

amount of DNA used in electroporations and reducing the time after transfections for the protein to be produced in the cell did not alter the expression levels. As explained in chapter 3, electroporation transfections are preferred to chemical transfections for a variety of reasons helpful in FFS experiments. To further test for proper expression of both plasmids in healthy cells, chemical transfections were also performed with unsatisfactory results. I expect proper membrane localization of the labeled GIRK subunits after the proper GIRK subunit pairings are known, from western and coimmunoprecipitation assays. However, if proper membrane localization does not occur when co-expressing subunits that form functional GIRK channels on MIN6 cells, subunits originating from the same animal should be tested. Once proper membrane trafficking of the GIRK subunits is achieved, co-expression of the D3 receptor and GIRK subunit(s) should be performed. If cells are healthy and expression is plasma membrane localized, measurements between the D3 dopamine receptor and GIRK channel should be performed to determine if the GPCR and proposed target channel are in close proximity on the membrane.

CHAPTER 6

CONCLUSION AND FUTURE DIRECTIONS

Conclusion

The goal of this work was to use fluorescence fluctuation spectroscopy (FFS) to identify the signaling mechanism of the dopamine mediated negative feedback pathway in pancreatic β cells. Previous studies have shown that islets can convert L-dopa to dopamine and then co-secrete dopamine with insulin (120, 121, 221). During glucose stimulated insulin secretion (GSIS), dopamine decreases intracellular calcium fluctuations in islets , which inhibits insulin secretion (120, 121, 221). The D2 dopamine receptor has been reported to be the receptor initiating the dopamine mediated negative feedback pathway (121, 221). However, both the D2 and D3 dopamine receptors have been found in β cells. Under a DRD3 selective inhibitor, the effect of dopamine on GSIS was ameliorated (120). but islets treated with a DRD2 selective inhibitor still showed dopamine modulation of GSIS (120). Thus, we hypothesized the dopamine mediated negative feedback pathway is initiated by the D3 receptor and not the D2 receptor.

To determine the mechanism of the different signaling by the D3 and D2 dopamine receptors and their heterotrimeric G-proteins, I used fluorescence fluctuation spectroscopy (FFS) to study protein interactions. To label the receptors and heterotrimeric G-proteins, I used EGFP and mApple fluorescent protein. mCherry and mRFP had previously been used alongside EGFP in two-color, two-photon FFS studies; however, mApple had not. In my initial work, I characterized the mApple fluorescent

protein to confirm its utility for FFS studies. Due to the relation between fluorophore brightness and the signal-to-noise ratio in FFS, I hypothesized that mApple would be a superior choice for FFS studies. I showed the diffusion rates of mApple in solution and in the cell were comparable to previously reported fluorescent protein diffusion rates (134, 216–218). Furthermore, I showed a 2.5 fold increase in measured heteromerization between unlinked and linked EGFP and mApple control constructs. These experiments confirmed that mApple could be used to label proteins for single component FFS studies and be paired effectively with EGFP for two component studies.

Having established the utility of mApple in FFS experiments, I next measured the diffusion rates of the D3 dopamine receptor and G_{γ} subunit by FFS to establish both membrane proteins followed previously measured behavior for diffusion. I fit the measured autocorrelation curve with multiple diffusion models including single-component, single-component with triplet fraction, and two-component. A two-component model fit to the data yielded the smallest sum of least squares of the residuals. Based on comparison with previous studies, I attributed the slower diffusion component represents the plasma membrane bound portion of the protein and the faster component represents the intracellular portion (176, 190, 193, 272). I measured the diffusion rates before and after treatment with 100 µM of dopamine and found no statistically significant difference in diffusion rates before and after treatment. This finding is expected since the proteins are not internalized after treatment, but stay on the plasma membrane. Furthermore, the determined diffusion rates are in agreement with other reports for transmembrane and inner-leaflet proteins (194, 205–208).

To test the hypothesis that the D3 dopamine receptor is activated after dopamine treatment, I measured the heteromerization between the D3 receptor and G_{γ} subunit in MIN6 cells. The $G_{\beta\gamma}$ complex is a dimer of the G_{β} and G_{γ} subunits, therefore I initially only labeled the G_{γ} subunit. I hypothesized I would measure a decrease heteromerization between the D3 receptor and G_{γ} subunit after dopamine treatment, indicating a ligand was bound to the D3 receptor and the heterotrimeric G-proteins were activated. However, my results showed very little heteromerization between the two proteins either before or after dopamine treatment.

We suspected that maybe both the G_{γ} and G_{β} subunits needed to be overexpressed in order to detect signaling changes, so I simultaneously transfected a G_{β} subunit labeled with mCerulean. mCerulean is not excited at the FFS excitation wavelength of 1000nm and therefore its presence does not interfere with two-color measurements with EGFP and mApple. I confirmed the presence and location of all three fluorescent proteins by spectral imaging. Using this data, I could verify the localization of the G_{β} and G_{γ} subunits and D3 dopamine receptor on the plasma membrane prior to FFS measurements. After overexpressing all three proteins, I measured a reduction in heteromerization between the D3 dopamine receptor and G_{γ} subunit indicating the D3 receptor was activated by dopamine. This result not only confirms the D3 receptor is activated after dopamine treatment, but also shows the requirement to express both subunits of the $G_{\beta\gamma}$ complex to properly measure signaling by a G-protein coupled receptor (GPCR).

To determine whether the D2 receptor is similarly activated by dopamine, I overexpressed both the G_{β} and G_{γ} subunits and D2 dopamine receptor in MIN6 cells.

Similar to the D3 receptor, I expected to observe a decrease in heteromerization between the D2 receptor and G_{γ} complex after dopamine treatment if the D2 receptor is activated. I found low heteromerization before and after treatment, indicating the D2 receptor is not activated by dopamine during GSIS. This result agrees with a previous study which determined preferential signaling of D3 dopamine receptor over D2 receptor to inhibit GSIS (120). This result also agrees with previous studies which suggest the D2 receptor is localized to insulin granules (121, 221).

To investigate the proposed activation of GIRK in the dopamine mediated negative feedback pathway, I measured heteromerization interactions between GIRK3 and the G_{γ} subunit. Because the GIRK channel is formed from the tetramerization of GIRK subunits, I chose to first measure interactions with the GIRK3 subunit due to its ability to form functional channels with all other subunits and thus testing a broad range of GIRK channels by labeling a single subunit (240, 244, 245). Overexpressing the protein resulted in a large intracellular component. This was expected as the GIRK3 subunit cannot form functional channels on its own. By overexpressing the protein, it appears that more GIRK3 subunits are formed than the cell can use in the production of GIRK channels. Single component measurements at the plasma membrane were performed to determine the plasma membrane diffusion rate. A two-component diffusion model gave the best fit, with the expected diffusion rates for membrane proteins, for the autocorrelation curves of GIRK3 (194, 205–208). Similar to what was found with the D3 receptor and G_{γ} subunit measurements, no statistical difference was found in the diffusion rate of GIRK3 before and after dopamine treatment.

To investigate whether D3 activation causes increased heteromerization between the $G_{\beta\gamma}$ complex and GIRK channels, I performed FFS measurements between the G_{γ} subunit and GIRK3. I hypothesized that if a GIRK channel composed of the GIRK3 subunit was activated by the $G_{\beta\gamma}$ complex, I would measure an increase in heteromerization after dopamine stimulation between the G_{γ} subunit and GIRK3. FFS measurements showed no heteromerization between the two proteins either before or after dopamine stimulation. Measurements with both the G_{β} and G_{γ} subunits present were not tested and are discussed further below in future experiments.

One explanation of the fast reaction of GPCR signaling is the close proximity of GPCRs and their downstream targets (267, 268). To test this theory with the dopamine receptor and GIRK channels, I sought to perform two-color FFS measurements between GIRK3 and the D3 dopamine receptor. If the two proteins are in a complex, I hypothesize they will have a heteromerization constant higher than two unlinked proteins. However, transfected cells that expressed both proteins exhibited cell rounding and improper membrane protein localization of the labeled proteins, suggesting that the cells are unhealthy. Therefore, no FFS measurements were performed between the D3 dopamine receptor and GIRK channel.

Concurrent to taking two-color FFS measurements between the D3 dopamine receptor and the GIRK3 subunit, we hypothesized that improper trafficking of the GIRK3 receptor might be occurring. Thus, I expressed the other 3 GIRK components with fluorescent tags into MIN6 cells independently. All GIRK subunits had large intracellular components, including the GIRK2 subunit which is able to form homotetramer GIRK channels (238, 239). Additionally, I co-expressed GIRK3 with GIRK2 and GIRK4 which

are both known to form functional GIRK channels with GIRK3. Unfortunately, none of these other transfections improved the plasma membrane localization.

Future Directions

Studying Interactions between DRD3 and GIRK Channel

I hypothesized activation of the dopamine receptor initiates the heterotrimeric G-proteins to activate a GIRK channel which hyperpolarizes the membrane causing voltage gated calcium channels to close. This hypothesis was developed following results from unpublished patch-clamp studies by Dr. Jacobson and Dr. Ustione which showed that hyperpolarization of the membrane after dopamine stimulation results from potassium channel activation other than the K_{ATP} channel. Additionally, previous neural studies have shown activation of dopamine receptors signals to GIRK channels to open (265, 266, 273). However, the change in intracellular calcium could be due to direct inactivation of calcium channels by the $G_{\beta\gamma}$ complex (274). If the $G_{\beta\gamma}$ complex does inactivate calcium channels, no increase in heteromerization between labeled GIRK subunits and $G_{\beta\gamma}$ complex would be observed after dopamine stimulation. The following proposed future studies which include the GIRK channel in this dissertation are based on the hypothesis that the $G_{\beta\gamma}$ complex activates GIRK channels directly.

Above, I described the difficulties in measuring interactions between the GIRK channel and the DRD3 and $G_{\beta\gamma}$ complex. To examine the potential interactions between the D3 receptor and GIRK channels, proper plasma membrane localization of GIRK subunits must first be achieved. First, I would determine which GIRK subunits tetramerize to form channels inherently in MIN6 β cells. I propose using western and

coimmunoprecipitation assays to detect interactions between subunits. These methods have been previously used to determine pairings of GIRK channels in neurons (241, 242). After identifying which GIRK channels are formed in MIN6 β cells, specific pairs of GIRK subunits can be co-expressed in the cell to facilitate incorporation of these subunits in GIRK channels localized to the plasma membrane. For example, if GIRK1 and GIRK2 channels are discovered to be most prominent in β cells, then GIRK1 and GIRK2 should be co-expressed for future experiments.

One possible explanation for improper plasma membrane trafficking of the GIRK subunits is the lack of conserved regions between the subunits due to the multiple species of origin: mouse, rat, and human. In oocytes, expression of subunits from different species has not inhibited the formation of functional channels at the plasma membrane, thus it was originally assumed this would also be the case for expression in MIN6 cells (259–261). Furthermore, the GIRK3 subunit tested here has not been previously paired to form functional channels with the other GIRK subunits tested (259–261). The GIRK3 described in this dissertation could be improperly folding and therefore not interacting with other GIRK subunits properly, be they inherent to the cell or also transfected. Furthermore, the spacing between the turboGFP (tGFP) label and GIRK3 could be interfering with the folding and trafficking of the GIRK3 subunit. To determine if this is the case, the mApple-GIRK3, which I constructed for measurements between the GIRK3 and D3 dopamine receptor, could be co-expressed with the other GIRK subunits previously shown to localize to the plasma membrane (259–261).

To measure activation of the D3 receptor through the decreased heteromerizaiton of the receptor and heterotrimeric G-proteins, I had to overexpress

both the G_β and G_γ subunits. In measuring interactions between the proposed downstream target, GIRK, and the $G_{\beta\gamma}$ complex, which I hypothesize activates the GIRK channels, I only overexpressed GIRK3 and the G_γ subunit. It is reasonable to assume that expression of both the G_β and G_γ subunits are necessary to properly measure signaling by the $G_{\beta\gamma}$ complex to a downstream target.

Assuming GIRK is the downstream target signaled to by the $G_{\beta\gamma}$ complex, activation of GIRK channels would result in hyperpolarization of the membrane which causes voltage gated calcium channels to close. For efficient signal transduction, all three proteins might be in close proximity on the membrane. It would be interesting to determine if voltage gated calcium channels and GIRK channels are located in close proximity to dopamine receptors. If all three proteins are determined to be in close proximity to each other, they could also be located with other GPCRs which control potassium and calcium channels in response to other stimuli in the β cell too (53, 72, 103, 104). Alternatively, none of the three could be located in close proximity to each other since other stimuli control ion channel opening and closing also. A third potential outcome could be the close proximity of the downstream target protein, GIRK, and the D3 receptor, not proteins like the calcium channel involved in further downstream signaling. The relationship of all three proteins: D3 dopamine receptor, GIRK channel, and voltage gated calcium channel, can be measured between two proteins at a time through FFS. I would begin measuring the heteromerization between the D3 receptor and GIRK channel. If the two are in close proximity to each other, I would then measure the heteromerization between the GIRK channel and voltage gated calcium channel.

Studying Interactions in Primary Cells

Many animal models have been used to study diabetes, for example, the D3 receptor knock out mouse line. As a control experiment, signaling of receptor activation should be performed in primary β cells and the results compared to those reported in MIN6 cells. Primary cells from different animals can behave differently and therefore a broader range of results may occur in comparison to studies using cell lines. I performed initial primary cell studies by isolating islets from murine models, dispersing the cells, and then electroporating MIN6 cells with the D3 dopamine receptor and G_{γ} subunit constructs. Due to the fragility of primary cells, they cannot be electroporated with the same protocol as primary islets. I found reducing the voltage to 180V, for a single 5ms pulse resulted in the highest percentage of transfected cells. Also, harvesting islets is laborious and results in small amounts of cells. For efficient electroporations, a minimum cell mixture volume of 40µL at 10^8 cells/ml is required, usually requiring two murine pancreases for one electroporation cuvette. Thus, obtaining enough cells for efficient transfections will be difficult. Additionally, islets are composed of multiple cell types including α and δ cells which may exhibit different responses to dopamine. For murine primary cells, the majority of the islet is composed of β cells and thus statistically most measurements should be from β cells. Post study staining for insulin is one way to confirm measurements are only from β cells. However, this requires precise knowledge of exactly which cell each FFS measurement was taken from.

Having established the preference of signaling through the D3 receptor, it would be interesting to study the protein signaling pathway in the D3 knock out mouse line.

Unpublished data from Dr. Ustione shows islets lacking the D3 receptor secrete more insulin, but are still sensitive to dopamine. To further understand this occurrence, a two-color FFS study between the D2 receptor and $G_{\beta\gamma}$ complex in dispersed β cells from the D3 knock out mouse line could be performed. Additionally, this occurrence could be studied through the use of CRISPR or RNAi to knock-down the D3 receptor. It may be that the D2 receptor compensates for the long-term absolute lack of the D3 receptor. If this is the case, I would expect to observe a decrease in heteromerization between the D2 receptor and $G_{\beta\gamma}$ complex after dopamine stimulation.

Two Color SpIDA

Spatial intensity distribution analysis (SpIDA) allows protein interaction to be determined from raster images of cells by using spatial correlations between multiple pixels rather that temporal fluctuations from a single point measurement. The analysis measures changes in the fluorescent signal between pixels to determine a quantal brightness value of the fluorescent tag. A dimer would have twice the quantal brightness of a monomer. Two-color SpIDA is currently being developed and will determine protein heteromerization from cell images. It will be interesting to see if the same results from FFS are obtained from two-color SpIDA measurements. FFS requires a stable average fluorescence count to perform measurements and therefore slow moving proteins must be bleached before measurements. These proteins could be involved in signaling that is undetectable by FFS. For SpIDA measurements however, no bleaching occurs as differences in fluctuations are determined from changes in pixels. Furthermore, signaling by the $G_{\beta\gamma}$ complex is difficult to measure by FFS due to its promiscuity with other GPCRs. Heteromerization between the $G_{\beta\gamma}$ complex and the receptor or target

protein must be great enough to overcome the noise of other $G_{\beta\gamma}$ complexes fluorescently labeled, but signaling in other pathways. SpIDA measures heteromerization only through histogram analysis of raster images and could measure interactions by the $G_{\beta\gamma}$ complex graphically rather than over time as with FFS.

An advantage of SpIDA is that it can be performed on images taken of fixed cells. This is especially helpful in primary cells which are not as robust as cell lines and require staining for confirmation that measurements are performed on β cells and no other cell types in the islet. Thus, staining of βcells for insulin could be performed prior to heteromerization measurements so that β cells were easily distinguishable. While care must be taken to not alter protein localization or structure during fixation and staining, staining of endogenous protein would eliminate the potential toxicity of transfections which can alter cell functions.

Because it can be used on intrinsic proteins, two color SpIDA could be very advantageous to studying interactions with the GIRK channel. When overexpressing the GIRK plasmids, I showed lower plasma membrane localization than found when I overexpressed other membrane proteins. With SpIDA, dyes can be used to label the endogenous proteins of interest within the cell. Thus, endogenous GIRK channels could be fluorescently tagged by staining and their interactions with other proteins measured by two color SpIDA.

Significance

In this dissertation, I applied fluorescence fluctuation spectroscopy to study protein signaling at the cell membrane. Through changes in measured heteromerization between the D3 receptor and $G_{\beta\gamma}$ complex, which were not found between the D2 receptor and $G_{\beta\gamma}$ complex, I confirmed the preferential signaling of the D3 receptor in the dopamine mediated feedback pathway. I showed the changes in heteromerization between a GPCR and heterotrimeric G-proteins during activation. Currently, 293 non-odorant GPCRs have been found in islets, all of them signaling through heterotrimeric G-proteins (53). The G-proteins I overexpressed in the cell formed $G_{\beta\gamma}$ complexes used in signaling other pathways. Thus, my data is significant because I was able to measure the changes in heteromerization between the D3 dopamine receptor over other signaling by $G_{\beta\gamma}$ complexes occurring in the cell. Additionally, I used two fluctuation analysis methods, cross-correlation and brightness analysis, to confirm my results. This is the first time both methods have been used concurrently together to solve a biological problem.

The results of this dissertation are beneficial for creating treatments for patients developing type II diabetes. As a pre-diabetic patient's insulin resistance increases, β cells compensate by increasing insulin secretion. The increased stress to produce more insulin leads to β cells death and hyperglycemia. Intervention to decrease insulin secretion at the time of insufficient regulation and production of insulin by β cells would prevent cell death. This dissertation work suggests only the stimulation of D3 receptors is necessary to decrease insulin secretion of the pancreas.

REFERENCES

1. Northwestern State University, and Bossier Parish Community College. 2015. Anatomy and Physiology Modules. BPCC/NSU Title III Coop. Proj. .

2. Widmaier, E.P., H. Raff, and K.T. Strang. 2008. Vander's Human Physiology. 11th ed. New York: McGraw-Hill Company Inc.

3. Ganong, W. 2005. Digestion and Absorption. In: Review of Medical Physiology. . pp. 384 – 393.

4. Miller, R.E. 1981. Pancreatic neuroendocrinology: peripheral neural mechanisms in the regulation of the Islets of Langerhans. Endocr. Rev. 2: 471–94.

5. Schaser, K.D., G. Puhl, B. Vollmar, M.D. Menger, J.F. Stover, K. Kohler, P. Neuhaus, and U. Settmacher. 2005. In vivo imaging of human pancreatic microcirculation and pancreatic tissue injury in clinical pancreas transplantation. Am J Transpl. 5: 341–350.

6. Whitcomb, D.C., and M.E. Lowe. 2007. Human Pancreatic Digestive Enzymes. Dig. Dis. Sci. 52: 1–17.

7. Henderson, J.R., and M.C. Moss. 1985. A morphometric study of the endocrine and exocrine capillaries of the pancreas. Q. J. Exp. Physiol. 70: 347–356.

8. Winzell, M.S., and B. Ahrén. 2007. G-protein-coupled receptors and islet function-implications for treatment of type 2 diabetes. Pharmacol. Ther. 116: 437–48.

9. Cabrera, O., D.M. Berman, N.S. Kenyon, C. Ricordi, P.-O. Berggren, and A. Caicedo. 2006. The unique cytoarchitecture of human pancreatic islets has implications for islet cell function. Proc. Natl. Acad. Sci. U. S. A. 103: 2334–9.

10. Kim, A., K. Miller, J. Jo, G. Kilimnik, P. Wojcik, and M. Hara. 2010. Islet architecture: A comparative study. Islets. 1: 129–36.

11. Wang, P., N.M. Fiaschi-Taesch, R.C. Vasavada, D.K. Scott, A. García-Ocaña, and A.F. Stewart. 2015. Diabetes mellitus—advances and challenges in human β-cell proliferation. Nat. Rev. Endocrinol. 11: 201–212.

12. Brissova, M., M.J. Fowler, W.E. Nicholson, A. Chu, B. Hirshberg, D.M. Harlan, and A.C. Powers. 2005. Assessment of human pancreatic islet architecture and composition by laser scanning confocal microscopy. J. Histochem. Cytochem. 53: 1087–97.

13. Steiner, D.J., A. Kim, K. Miller, and M. Hara. 2010. Pancreatic islet plasticity: interspecies comparison of islet architecture and composition. Islets. 2: 135–45.

14. Kilimnik, G., J. Jo, V. Periwal, M.C. Zielinski, and M. Hara. 2012. Quantification of islet size and architecture. Islets. 4: 167–72.

15. Santos, R.M., L.M. Rosario, A. Nadal, J. Garcia-Sancho, B. Soria, and M. Valdeolmillos. 1991. Widespread synchronous [Ca2+]i oscillations due to bursting electrical activity in single pancreatic islets. Pflügers Arch. Eur. J. Physiol. 418: 417–22.

16. Benninger, R.K.P., M. Zhang, W.S. Head, L.S. Satin, and D.W. Piston. 2008. Gap junction coupling and calcium waves in the pancreatic islet. Biophys. J. 95: 5048–61.

17. Benninger, R.K.P., T. Hutchens, W.S. Head, M.J. McCaughey, M. Zhang, S.J. Le Marchand, L.S. Satin, and D.W. Piston. 2014. Intrinsic Islet Heterogeneity and Gap Junction Coupling Determine Spatiotemporal Ca2+ Wave Dynamics. Biophys. J. 107: 2723–2733.

18. Serre-Beinier, V., C. Mas, A. Calabrese, D. Caton, J. Bauquis, D. Caille, A. Charollais, V. Cirulli, and P. Meda. 2002. Connexins and secretion. Biol. Cell. 94: 477–92.

19. Ravier, M. a, M. Güldenagel, A. Charollais, A. Gjinovci, D. Caille, G. Söhl, C.B. Wollheim, K. Willecke, J. Henquin, and P. Meda. 2005. Loss of connexin36 channels alters beta-cell coupling, islet synchronization of glucose-induced Ca2+ and insulin oscillations, and basal insulin release. Diabetes. 54: 1798–807.

20. Chowdhury, A., O. Dyachok, A. Tengholm, S. Sandler, and P. Bergsten. 2013. Functional differences between aggregated and dispersed insulin-producing cells. Diabetologia. 56: 1557–68.

21. Dunbar, J.C., and M.F. Walsh. 1982. Glucagon and insulin secretion by dispersed islet cells: possible paracrine relationships. Horm. Res. 16: 257–67.

22. Shieh, J.C., and J.C. Dunbar. 1987. Insulin, glucagon and somatostatin secretion by cultured islets from normal and diabetic hamsters. Acta Diabetol. Lat. 24: 287–97.

23. Ahrén, B. 2000. Autonomic regulation of islet hormone secretion--implications for health and disease. Diabetologia. 43: 393–410.

24. Brunicardi, F.C., D.M. Shavelle, and D.K. Andersen. 1995. Neural regulation of the endocrine pancreas. Int. J. Pancreatol. 18: 177–95.

25. Holst, J.J., C. Sottimano, M. Olesen, S. Lindkaer, and O. V Nielsen. 1981. Nervous control of gastro-pancreatic somatostatin secretion in pigs. Peptides. 2 Suppl 2: 215–21.

26. Ahrén, B., and G.J. Taborsky. 1986. The mechanism of vagal nerve stimulation of glucagon and insulin secretion in the dog. Endocrinology. 118: 1551–7.

27. Ahrén, B., T.L. Paquette, and G.J. Taborsky. 1986. Effect and mechanism of vagal nerve stimulation on somatostatin secretion in dogs. Am. J. Physiol. 250: E212–7.

28. Karlsson, S., and B. Ahrén. 1993. Muscarinic receptor subtypes in carbachol-stimulated insulin and glucagon secretion in the mouse. J. Auton. Pharmacol. 13: 439–446.

29. Patel, D.G. 1984. Role of parasympathetic nervous system in glucagon response to insulin-induced hypoglycemia in normal and diabetic rats. Metabolism. 33: 1123–1127.

30. Ahren, B., N. Wierup, and F. Sundler. 2006. Neuropeptides and the Regulation of Islet Function. Diabetes. 55: S98–S107.

31. Woods, S.C., and D. Porte. 1974. Neural control of the endocrine pancreas. Physiol. Rev. 54: 596–619.

32. Karlsson, S., U. Myrsén, A. Nieuwenhuizen, F. Sundler, and B. Ahrén. 1997.

Presynaptic sympathetic mechanism in the insulinostatic effect of epinephrine in mouse pancreatic islets. Am. J. Physiol. 272: R1371–8.

33. Ackerman, E., L.C. Gatewood, J.W. Rosevear, and G.D. Molnar. 1965. Model studies of blood-glucose regulation. Bull. Math. Biophys. 27: Suppl:21–37.

34. Aronoff, S.L., K. Berkowitz, B. Shreiner, and L. Want. 2004. Glucose Metabolism and Regulation: Beyond Insulin and Glucagon. Diabetes Spectr. 17: 183–190.

35. Guo, X., H. Li, H. Xu, S. Woo, H. Dong, F. Lu, A.J. Lange, and C. Wu. 2012. Glycolysis in the control of blood glucose homeostasis. Acta Pharm. Sin. B. 2: 358–367.

36. Müller, W.A., G.R. Faloona, E. Aguilar-Parada, and R.H. Unger. 1970. Abnormal alpha-cell function in diabetes. Response to carbohydrate and protein ingestion. N. Engl. J. Med. 283: 109–15.

37. Chiang, J.L., M.S. Kirkman, L.M.B. Laffel, and A.L. Peters. 2014. Type 1 Diabetes Through the Life Span: A Position Statement of the American Diabetes Association. Diabetes Care. 37: 2034–2054.

38. van Belle, T.L., K.T. Coppieters, and M.G. von Herrath. 2011. Type 1 diabetes: etiology, immunology, and therapeutic strategies. Physiol. Rev. 91: 79–118.

39. Lin, Y., and Z. Sun. 2010. Current views on type 2 diabetes. J. Endocrinol. 204: 1–11.

40. Olokoba, A.B., O.A. Obateru, and L.B. Olokoba. 2012. Type 2 diabetes mellitus: A review of current trends. Oman Med. J. 27: 269–273.

41. Stumvoll, M., B.J. Goldstein, and T.W. van Haeften. 2005. Type 2 diabetes: principles of pathogenesis and therapy. Lancet (London, England). 365: 1333–46.

42. DeFronzo, R.A., R.C. Bonadonna, and E. Ferrannini. 1992. Pathogenesis of NIDDM. A balanced overview. Diabetes Care. 15: 318–68.

43. Harrigan, R.A., M.S. Nathan, and P. Beattie. 2001. Oral agents for the treatment of type 2 diabetes mellitus: pharmacology, toxicity, and treatment. Ann. Emerg. Med. 38: 68–78.

44. Saltiel, A.R., and J.M. Olefsky. 1996. Thiazolidinediones in the Treatment of Insulin Resistance and Type II Diabetes. Diabetes. 45: 1661–1669.

45. Evans, D.M. 2002. Dipeptidyl peptidase IV inhibitors. IDrugs. 5: 577–85.

46. Lebovitz, H.E. 1997. ALPHA-GLUCOSIDASE INHIBITORS. Endocrinol. Metab. Clin. North Am. 26: 539–551.

47. Idris, I., and R. Donnelly. 2009. Sodium-glucose co-transporter-2 inhibitors: an emerging new class of oral antidiabetic drug. Diabetes, Obes. Metab. 11: 79–88.

48. Fredriksson, R., M.C. Lagerström, L.-G. Lundin, and H.B. Schiöth. 2003. The G-protein-coupled receptors in the human genome form five main families. Phylogenetic analysis, paralogon groups, and fingerprints. Mol. Pharmacol. 63: 1256–1272.

49. Kroeze, W.K., J. Douglas, and B.L. Roth. 2003. G-protein-coupled receptors at a glance. Cell Sci. a Glance. 116: 4867–4869.

50. Katritch, V., V. Cherezov, and R.C. Stevens. 2013. Structure-function of the G protein-coupled receptor superfamily. Annu Rev Pharmacol Toxicol. 53: 531–556.

51. Lagerström, M.C., and H.B. Schiöth. 2008. Structural diversity of G protein-coupled receptors and significance for drug discovery. Nat. Rev. Drug Discov. 7: 339–357.

52. Wheatley, M., D. Wootten, M. Conner, J. Simms, R. Kendrick, R. Logan, D. Poyner, and J. Barwell. 2012. Lifting the lid on GPCRs: the role of extracellular loops. Br. J. Pharmacol. 165: 1688–1703.

53. Amisten, S., A. Salehi, P. Rorsman, P.M. Jones, and S.J. Persaud. 2013. An atlas and functional analysis of G-protein coupled receptors in human islets of Langerhans. Pharmacol. Ther. 139: 359–91.

54. Zhang, Z., J. Wu, J. Yu, and J. Xiao. 2012. A brief review on the evolution of GPCR: conservation and diversification. Open J. Genet. 2: 11–17.

55. Ji, T.H., M. Grossmann, and I. Ji. 1998. G protein-coupled receptors. I. Diversity of receptor-ligand interactions. J. Biol. Chem. 273: 17299–302.

56. Perez, D.M., and S.S. Karnik. 2005. Multiple signaling states of G-protein-coupled receptors. Pharmacol. Rev. 57: 147–61.

57. Robert, J. 2015. G-Protein-Coupled Receptors. In: Textbook of Cell Signalling in Cancer: An Educational Approach. Switzerland: Springer International Publishing. pp. 77–92.

58. Kobilka, B.K. 2007. G protein coupled receptor structure and activation. Biochim. Biophys. Acta. 1768: 794–807.

59. Deupi, X., and B. Kobilka. 2007. Activation of G Protein-Coupled Receptors. Adv. Protein Chem. 74: 137–166.

60. Schmidt, C.J., T.C. Thomas, M. a Levine, and E.J. Neer. 1992. Specificity of G protein beta and gamma subunit interactions. J. Biol. Chem. 267: 13807–10.

61. Dupré, D.J., M. Robitaille, R.V. Rebois, and T.E. Hébert. 2009. The Role of Gβγ Subunits in the Organization, Assembly, and Function of GPCR Signaling Complexes. Annu. Rev. Pharmacol. Toxicol. 49: 31–56.

62. Belmonte, S.L., and B.C. Blaxall. 2011. G protein coupled receptor kinases as therapeutic targets in cardiovascular disease. Circ. Res. 109: 309–19.

63. Simon, M.I., M.P. Strathmann, and N. Gautam. 1991. Diversity of G proteins in signal transduction. Science. 252: 802–8.

64. Oldham, W.M., and H.E. Hamm. 2008. Heterotrimeric G protein activation by G-protein-coupled receptors. Nat. Rev. Mol. Cell Biol. 9: 60–71.

65. Smotrys, J.E., and M.E. Linder. 2004. PALMITOYLATION OF INTRACELLULAR SIGNALING PROTEINS: Regulation and Function. Annu. Rev. Biochem. 73: 559–587.

66. Jennings, B.C., and M.E. Linder. 2010. Regulation of g proteins by covalent modification. Handb. Cell Signaling, 2/e. 2: 1629–1633.

67. Lambright, D.G., J. Sondek, A. Bohm, N.P. Skiba, H.E. Hamm, and P.B. Sigler. 1996. The 2.0 A crystal structure of a heterotrimeric G protein. Nature. 379: 311–9.

68. Sondek, J., A. Bohm, D.G. Lambright, H.E. Hamm, and P.B. Sigler. 1996. Crystal structure of a G-protein beta gamma dimer at 2.1A resolution. Nature. 379: 369–74.

69. Wall, M. a, D.E. Coleman, E. Lee, J. a Iñiguez-Lluhi, B. a Posner, a G. Gilman, and S.R. Sprang. 1995. The structure of the G protein heterotrimer Gi alpha 1 beta 1 gamma 2. Cell. 83: 1047–58.

70. Clapham, D.E., and E.J. Neer. 1997. G PROTEIN βγ SUBUNITS. Annu. Rev. Pharmacol. Toxicol. 37: 167–203.

71. McCudden, C.R., M.D. Hains, R.J. Kimple, D.P. Siderovski, and F.S. Willard. 2005. G-protein signaling: back to the future. Cell. Mol. Life Sci. 62: 551–577.

72. Regard, J.B., H. Kataoka, D.A. Cano, E. Camerer, L. Yin, Y. Zheng, T.S. Scanlan, M. Hebrok, and S.R. Coughlin. 2007. Probing cell type–specific functions of Gi in vivo identifies GPCR regulators of insulin secretion. J. Clin. Invest. 117.

73. Dalley, J.W., and B.J. Everitt. 2009. Dopamine receptors in the learning, memory and drug reward circuitry. Semin. Cell Dev. Biol. 20: 403–410.

74. Demarest, K.T., and K.E. Moore. 1979. Comparison of dopamine synthesis regulation in the terminals of nigrostriatal, mesolimbic, tuberoinfundibular and tuberohypophyseal neurons. J. Neural Transm. 46: 263–77.

75. Moore, R.Y., and F.E. Bloom. 1978. Central catecholamine neuron systems: anatomy and physiology of the dopamine systems. Annu. Rev. Neurosci. 1: 129–69.

76. Tzschentke, T.M. 2001. Pharmacology and behavioral pharmacology of the mesocortical dopamine system. Prog. Neurobiol. 63: 241–320.

77. Fitzgerald, P., and T.G. Dinan. 2008. Prolactin and dopamine: what is the connection? A review article. J. Psychopharmacol. 22: 12–9.

78. Levant, B. 1997. The D3 dopamine receptor: neurobiology and potential clinical relevance. Pharmacol. Rev. 49: 231–252.

79. Wolf, E., K. Mitchell, M. Logue, C. Baldwin, A. Reardon, A. Aiello, S. Galea, K. Koenen, M. Uddin, D. Wildman, and M. Miller. 2014. The Dopamine D3 Receptor Gene and Posttraumatic Stress Disorder. J. Trauma. Stress. 27: 379–87.

80. Furuyashiki, T. 2012. Roles of Dopamine and Inflammation-Related Molecules in Behavioral Alterations Caused by Repeated Stress. J. Pharmacol. Sci. 120: 63–69.

81. Zhang, F., H. Fan, Y. Xu, K. Zhang, X. Huang, Y. Zhu, M. Sui, G. Sun, K. Feng, B. Xu, X. Zhang, Z. Su, C. Peng, and P. Liu. 2011. Converging evidence implicates the dopamine D3 receptor gene in vulnerability to schizophrenia. Am. J. Med. Genet. Part B Neuropsychiatr. Genet. 156: 613–619.

82. de Krom, M., W.G. Staal, R. a. Ophoff, J. Hendriks, J. Buitelaar, B. Franke, M. V. de Jonge, P. Bolton, D. Collier, S. Curran, H. van Engeland, and J.M. van Ree. 2009. A Common Variant in DRD3 Receptor Is Associated with Autism Spectrum Disorder. Biol. Psychiatry. 65: 625–630.

83. Agrawal, A., L. Wetherill, K.K. Bucholz, J. Kramer, S. Kuperman, M.T. Lynskey, J.I. Nurnberger, M. Schuckit, J. a. Tischfield, H.J. Edenberg, T. Foroud, and L.J. Bierut. 2013. Genetic influences on craving for alcohol. Addict. Behav. 38: 1501–1508.

84. Wei, J., C. Chu, Y. Wang, Y. Yang, Q. Wang, T. Li, L. Zhang, and X. Ma. 2012. Association study of 45 candidate genes in nicotine dependence in Han Chinese. Addict. Behav. 37: 622–626.

85. Bernheimer, H., W. Birkmayer, O. Hornykiewicz, K. Jellinger, and F. Seitelberger. 1973. Brain dopamine and the syndromes of Parkinson and Huntington. Clinical, morphological and neurochemical correlations. J. Neurol. Sci. 20: 415–55.

86. Kish, S.J., K. Shannak, and O. Hornykiewicz. 1988. Uneven pattern of dopamine loss in the striatum of patients with idiopathic Parkinson's disease. Pathophysiologic and clinical implications. N. Engl. J. Med. 318: 876–80.

87. Dikeos, D.G., G.N. Papadimitriou, D. Avramopoulos, G. Karadima, E.G. Daskalopoulou, D. Souery, J. Mendlewicz, D. Vassilopoulos, and C.N. Stefanis.

1999. Association between the dopamine D3 receptor gene locus (DRD3) and unipolar affective disorder. Psychiatr. Genet. 9: 189–195.

88. Retz, W., M. Rösler, T. Supprian, P. Retz-Junginger, and J. Thome. 2003. Dopamine D3 receptor gene polymorphism and violent behavior: Relation to impulsiveness and ADHD-related psychopathology. J. Neural Transm. 110: 561–572.

89. Light, K.J., P.R. Joyce, S.E. Luty, R.T. Mulder, C.M. a Frampton, L.R.M. Joyce, A.L. Miller, and M. a Kennedy. 2006. Preliminary evidence for an association between a dopamine D3 receptor gene variant and obsessive-compulsive personality disorder in patients with major depression. Am. J. Med. Genet. B. Neuropsychiatr. Genet. 141B: 409–413.

90. Hood, S.D., J.P. Potokar, S.J.C. Davies, D. a Hince, K. Morris, K.M. Seddon, D.J. Nutt, and S. V Argyropoulos. 2010. Dopaminergic challenges in social anxiety disorder: evidence for dopamine D3 desensitisation following successful treatment with serotonergic antidepressants. J. Psychopharmacol. 24: 709–716.

91. Goridis, C., and H. Rohrer. 2002. Specification of catecholaminergic and serotonergic neurons. Nat. Rev. Neurosci. 3: 531–541.

92. Purves, D., G. Augustine, and D. Fitzpatrick. 2001. Neuroscience: The Biogenic Amines. 2nd Editio. Sunderland (MA): Sinauer Associates.

93. Beaulieu, J., and R.R. Gainetdinov. 2011. The Physiology , Signaling , and Pharmacology of Dopamine Receptors. 63: 182–217.

94. Liu, Y.F., O. Civelli, D.K. Grandy, and P.R. Albert. 1992. Differential sensitivity of the short and long human dopamine D2 receptor subtypes to protein kinase C. J. Neurochem. 59: 2311–7.

95. Giros, B., M.P. Martres, C. Pilon, P. Sokoloff, and J.C. Schwartz. 1991. Shorter variants of the D3 dopamine receptor produced through various patterns of alternative splicing. Biochem. Biophys. Res. Commun. 176: 1584–92.

96. Wong, A.H.C., and H.H.M. Van Tol. 2003. The dopamine D4 receptors and mechanisms of antipsychotic atypicality. Prog. Neuropsychopharmacol. Biol. Psychiatry. 27: 1091–9.

97. Wong, A.H.C., C.E. Buckle, and H.H.M. Van Tol. 2000. Polymorphisms in dopamine receptors: What do they tell us? Eur. J. Pharmacol. 410: 183–203.

98. Chien, E.Y.T., W. Liu, Q. Zhao, V. Katritch, G.W. Han, M.A. Hanson, L. Shi, A.H. Newman, J.A. Javitch, V. Cherezov, and R.C. Stevens. 2010. Structure of the human dopamine D3 receptor in complex with a D2/D3 selective antagonist. Science. 330: 1091–1095.

99. Livingstone, C.D., P.G. Strange, and L.H. Naylor. 1992. Molecular modelling of D2-like dopamine receptors. Biochem. J. 287 (Pt 1): 277–82.

100. Robinson, S.W., K.R. Jarvie, and M.G. Caron. 1994. High affinity agonist binding to the dopamine D3 receptor: chimeric receptors delineate a role for intracellular domains. Mol. Pharmacol. 46: 352–356.

101. Zhang, W., and F.P. Bymaster. 1999. The in vivo effects of olanzapine and other antipsychotic agents on receptor occupancy and antagonism of dopamine D1, D2, D3, 5HT2A and muscarinic receptors. Psychopharmacology (Berl). 141: 267–78.

102. Schotte, A., P.F. Janssen, W. Gommeren, W.H. Luyten, P. Van Gompel, A.S. Lesage, K. De Loore, and J.E. Leysen. 1996. Risperidone compared with new and reference antipsychotic drugs: in vitro and in vivo receptor binding. Psychopharmacology (Berl). 124: 57–73.

103. García-Tornadú, I., A.M. Ornstein, A. Chamson-Reig, M.B. Wheeler, D.J. Hill, E. Arany, M. Rubinstein, and D. Becu-Villalobos. 2010. Disruption of the dopamine D2 receptor impairs insulin secretion and causes glucose intolerance. Endocrinology. 151: 1441–1450.

104. Itoh, M., B.L. Furman, and J.E. Gerich. 1982. Dopaminergic suppression of pancreatic somatostatin secretion. Acta Endocrinol. (Copenh). 101: 56–61.

105. Lomize, A., M. Lomize, and I. Pogozheva. 2013. Orientations of Proteins in Membranes: 3pbl Dopamine Receptor. .

106. Komatsu, M., M. Takei, H. Ishii, and Y. Sato. 2013. Glucose-stimulated insulin secretion: A newer perspective. J. Diabetes Investig. 4: 511–6.

107. Falck, B., and B. Hellman. 1963. Evidence for the presence of biogenic amines in

pancreatic islets. Experientia. 19: 139–140.

108. Ericson, L.E., R. Hhkanson, and I. Lundquist. 1977. Accumulation of Dopamine in Mouse Pancreatic B-Cells Following Injection of L-DOPA. Localization to Secretory Granules and Inhibition of Insulin Secretion. Diabetologia. 13: 117–124.

109. Feldman, J.M., A.E. Boyd, and H.E. Lebovitz. 1971. Structural determinants of catecholamine action on in vitro insulin release. J. Pharmacol. Exp. Ther. 176: 611–21.

110. von Dorsche, H.H., R. Krause, and P. Fehrmann. 1977. Occurrence of biogenic amines in the pancreatic islets of sand rats (Psammomys obesus). Endokrinologie. 69: 365–8.

111. Quickel, K.E., J.M. Feldman, and H.E. Lebovitz. 1971. Inhibition of insulin secretion by serotonin and dopamine: species variation. Endocrinology. 89: 1295–1302.

112. Leblanc, H., G.C. Lachelin, S. Abu-Fadil, and S.S. Yen. 1977. The effect of dopamine infusion on insulin and glucagon secretion in man. J. Clin. Endocrinol. Metab. 44: 196–8.

113. Zern, R.T., L.B. Foster, J.A. Blalock, and J.M. Feldman. 1979. Characteristics of the dopaminergic and noradrenergic systems of the pancreatic islets. Diabetes. 28: 185–9.

114. Lundquist, I., G. Panagiotidis, and a Stenström. 1991. Effect of L-dopa administration on islet monoamine oxidase activity and glucose-induced insulin release in the mouse. Pancreas. 6: 522–7.

115. Ahren, B., and I. Lundquist. 1985. Effects of L-Dopa-Induced Dopamine Accumultion on 45Ca+2 Efflux and Insulin Secretion in Isolated Rat Islets. Pharmacology. 30: 71–82.

116. Rodriguez-Diaz, R., M.H. Abdulreda, A.L. Formoso, I. Gans, C. Ricordi, P.-O. Berggren, and A. Caicedo. 2011. Innervation Patterns of Autonomic Axons in the Human Endocrine Pancreas. Cell Metab. 14: 45–54.

117. Goldstein, D.S., G. Eisenhofer, and I.J. Kopin. 2003. Sources and significance of

plasma levels of catechols and their metabolites in humans. J. Pharmacol. Exp. Ther. 305: 800–811.

118. Grouzmann, E., and F. Lamine. 2013. Determination of catecholamines in plasma and urine. Best Pract. Res. Clin. Endocrinol. Metab. 27: 713–723.

119. Eldrup, E. 2004. Significance and origin of DOPA, DOPAC, and dopamine-sulphate in plasma, tissues and cerebrospinal fluid. Dan. Med. Bull. 51: 34–62.

120. Ustione, A., and D.W. Piston. 2012. Dopamine synthesis and D3 receptor activation in pancreatic β-cells regulates insulin secretion and intracellular [Ca(2+)] oscillations. Mol. Endocrinol. 26: 1928–40.

121. Simpson, N., A. Maffei, M. Freeby, S. Burroughs, Z. Freyberg, J. Javitch, R.L. Leibel, and P.E. Harris. 2012. Dopamine-mediated autocrine inhibitory circuit regulating human insulin secretion in vitro. Mol. Endocrinol. 26: 1757–72.

122. Phizicky, E.M., and S. Fields. 1995. Protein-protein interactions: methods for detection and analysis. Microbiol. Rev. 59: 94–123.

123. Doupnik, C.A. 2008. GPCR-Kir channel signaling complexes: defining rules of engagement. J. Recept. Signal Transduct. Res. 28: 83–91.

124. Brückner, A., C. Polge, N. Lentze, D. Auerbach, and U. Schlattner. 2009. Yeast Two-Hybrid, a Powerful Tool for Systems Biology. Int. J. Mol. Sci. 10: 2763–2788.

125. Chien, C.T., P.L. Bartel, R. Sternglanz, and S. Fields. 1991. The two-hybrid system: a method to identify and clone genes for proteins that interact with a protein of interest. Proc. Natl. Acad. Sci. 88: 9578–9582.

126. Broussard, J.A., B. Rappaz, D.J. Webb, and C.M. Brown. 2013. Fluorescence resonance energy transfer microscopy as demonstrated by measuring the activation of the serine/threonine kinase Akt. Nat. Protoc. 8: 265–281.

127. Rowland, C.E., C.W. Brown, I.L. Medintz, and J.B. Delehanty. 2015. Intracellular FRET-based probes: a review. Methods Appl. Fluoresc. 3: 042006.

128. Frommer, W.B., M.W. Davidson, and R.E. Campbell. 2009. Genetically encoded biosensors based on engineered fluorescent proteins. Chem. Soc. Rev. 38: 2833.

129. Didenko, V. V. 2001. DNA probes using fluorescence resonance energy transfer (FRET): designs and applications. Biotechniques. 31: 1106–16, 1118, 1120–1.

130. Piston, D.W., and G.-J. Kremers. 2007. Fluorescent protein FRET: the good, the bad and the ugly. Trends Biochem. Sci. 32: 407–14.

131. Schwille, P., F.J. Meyer-Almes, and R. Rigler. 1997. Dual-color fluorescence cross-correlation spectroscopy for multicomponent diffusional analysis in solution. Biophys. J. 72: 1878–1886.

132. Chen, Y., M. Tekmen, L. Hillesheim, J. Skinner, B. Wu, and J.D. Müller. 2005. Dual-color photon-counting histogram. Biophys. J. 88: 2177–92.

133. Chen, Y., L.-N. Wei, and J.D. Müller. 2005. Unraveling protein-protein interactions in living cells with fluorescence fluctuation brightness analysis. Biophys. J. 88: 4366–77.

134. Hillesheim, L.N., Y. Chen, and J.D. Müller. 2006. Dual-color photon counting histogram analysis of mRFP1 and EGFP in living cells. Biophys. J. 91: 4273–84.

135. Van Orden, A., K. Fogarty, and J. Jung. 2004. Fluorescence fluctuation spectroscopy: a coming of age story. Appl. Spectrosc. 58: 122A–137A.

136. Elson, E.L., and D. Magde. 1974. Fluorescence correlation spectroscopy. I. Conceptual basis and theory. Biopolymers. 13: 1–27.

137. Magde, D., E.L. Elson, and W.W. Webb. 1974. Fluorescence Correlation Spectroscopy. II. An Experimental Realization. Biopolymers. 13: 29–61.

138. Magde, D., W.W. Webb, and E.L. Elson. 1978. Fluorescence correlation spectroscopy. III. Uniform translation and laminar flow. Biopolymers. 17: 361–376.

139. Rigler, R., U. Mets, J. Widengren, and P. Kask. 1993. Fluorescence correlation spectroscopy with high count rate and low background: analysis of translational diffusion. Eur. Biophys. J. 22: 169–175.

140. Rigler, R., J. Widengren, and Ü. Mets. 1993. Interactions and Kinetics of Single

Molecules as Observed by Fluorescence Correlation Spectroscopy. In: Fluorescence Spectroscopy. Berlin, Heidelberg: Springer Berlin Heidelberg. pp. 13–24.

141. Kettling, U., A. Koltermann, P. Schwille, and M. Eigen. 1998. Real-time enzyme kinetics monitored by dual-color fluorescence cross-correlation spectroscopy. Proc. Natl. Acad. Sci. U. S. A. 95: 1416–1420.

142. Winkler, T., U. Kettling, A. Koltermann, and M. Eigen. 1999. Confocal fluorescence coincidence analysis: an approach to ultra high-throughput screening. Proc. Natl. Acad. Sci. U. S. A. 96: 1375–8.

143. Schwille, P., U. Haupts, S. Maiti, and W.W. Webb. 1999. Molecular dynamics in living cells observed by fluorescence correlation spectroscopy with one- and two-photon excitation. Biophys. J. 77: 2251–65.

144. Weidemann, T., M. Wachsmuth, M. Tewes, K. Rippe, and J. Langowski. 2002. Analysis of Ligand Binding by Two-Colour Fluorescence Cross-Correlation Spectroscopy. Single Mol. 3: 49–61.

145. Denk, W., J.H. Strickler, and W.W. Webb. 1990. Two-photon laser scanning fluorescence microscopy. Science. 248: 73–6.

146. Schwille, P., U. Haupts, S. Maiti, and W.W. Webb. 1999. Molecular dynamics in living cells observed by fluorescence correlation spectroscopy with one- and two-photon excitation. Biophys. J. 77: 2251–65.

147. Kask, P., K. Palo, D. Ullmann, and K. Gall. 1999. Fluorescence-intensity distribution analysis and its application in biomolecular detection technology. Proc. Natl. Acad. Sci. 96: 13756–13761.

148. Chen, Y., J.D. Müller, P.T. So, and E. Gratton. 1999. The photon counting histogram in fluorescence fluctuation spectroscopy. Biophys. J. 77: 553–67.

149. Müller, J.D. 2004. Cumulant analysis in fluorescence fluctuation spectroscopy. Biophys. J. 86: 3981–92.

150. Wu, B., and J.D. Müller. 2005. Time-integrated fluorescence cumulant analysis in fluorescence fluctuation spectroscopy. Biophys. J. 89: 2721–35.

151. Wu, B., and J.D. Müller. 2008. Time-integrated fluorescence cumulant analysis in fluorescence fluctuation spectroscopy. Biophys. J. 89.

152. Petersen, N.O., P.L. Höddelius, P.W. Wiseman, O. Seger, and K.E. Magnusson. 1993. Quantitation of membrane receptor distributions by image correlation spectroscopy: concept and application. Biophys. J. 65: 1135–46.

153. Digman, M.A., M. Stakic, and E. Gratton. 2013. Raster Image Correlation Spectroscopy and Number and Brightness Analysis. 1st ed. Elsevier Inc.

154. Gröner, N., J. Capoulade, C. Cremer, and M. Wachsmuth. 2010. Measuring and imaging diffusion with multiple scan speed image correlation spectroscopy. Opt. Express. 18: 21225–37.

155. Srinivasan, V.J., T.H. Ko, M. Wojtkowski, M. Carvalho, A. Clermont, S.E. Bursell, Q.H. Song, J. Lem, J.S. Duker, J.S. Schuman, and J.G. Fujimoto. 2006. Noninvasive volumetric imaging and morphometry of the rodent retina with high-speed, ultrahigh-resolution optical coherence tomography. Invest Ophthalmol Vis Sci. 47: 5522–5528.

156. Digman, M. a, C.M. Brown, P. Sengupta, P.W. Wiseman, A.R. Horwitz, and E. Gratton. 2005. Measuring fast dynamics in solutions and cells with a laser scanning microscope. Biophys. J. 89: 1317–27.

157. Petersen, N.O. 1986. Scanning fluorescence correlation spectroscopy. I. Theory and simulation of aggregation measurements. Biophys J. 49: 809–815.

158. Petrásek, Z., J. Ries, and P. Schwille. 2010. Scanning FCS for the characterization of protein dynamics in live cells. Methods Enzymol. 472: 317–43.

159. Dörlich, R.M., Q. Chen, P. Niklas Hedde, V. Schuster, M. Hippler, J. Wesslowski, G. Davidson, and G.U. Nienhaus. 2015. Dual-color dual-focus line-scanning FCS for quantitative analysis of receptor-ligand interactions in living specimens. Sci. Rep. 5: 10149.

160. Sanchez, S.A., M.A. Tricerri, and E. Gratton. 2012. Laurdan generalized polarization fluctuations measures membrane packing micro-heterogeneity in vivo. Proc. Natl. Acad. Sci. U. S. A. 109: 7314–9.

161. Lakowicz, J.R. 2006. Principles of Fluorescence Spectroscopy. Boston, MA: Springer US.

162. Gell, C., V. Bormuth, G.J. Brouhard, D.N. Cohen, S. Diez, C.T. Friel, J. Helenius, B. Nitzsche, H. Petzold, J. Ribbe, E. Schäffer, J.H. Stear, A. Trushko, V. Varga, P.O. Widlund, M. Zanic, and J. Howard. 2010. Single Molecule Fluorescence Techniques. In: Handbook of Single Molecule Fluorescence Spectroscopy. Oxford: Oxford University Press.

163. Shi, X., and T. Wohland. 2010. Fluoresccence Correlation Spectroscopy. In: Diaspro A, editor. Nannoscopy and Multidimensional Optical Fluorescent Microscopy. Chapman and Hall. pp. 1–34.

164. Webb, W.W. 2001. Fluorescence correlation spectroscopy: inception, biophysical experimentations, and prospectus. Appl. Opt. 40: 3969.

165. Krichevsky, O., and G. Bonnet. 2002. Fluorescence correlation spectroscopy: the technique and its applications. Reports Prog. Phys. 65: 251–297.

166. Bacia, K., S.A. Kim, and P. Schwille. 2006. Fluorescence cross-correlation spectroscopy in living cells. Nat. Methods. 3: 83–89.

167. Müller, J.D., Y. Chen, and E. Gratton. 2000. Resolving heterogeneity on the single molecular level with the photon-counting histogram. Biophys. J. 78: 474–86.

168. Piston, D.W. 1999. Imaging living cells and tissues by two-photon excitation microscopy. Trends Cell Biol. 9: 66–9.

169. So, P.T.C., C.Y. Dong, B.R. Masters, and K.M. Berland. 2000. Two-Photon Excitation Fluorescence Microscopy. Annu. Rev. Biomed. Eng. 2: 399–429.

170. Dragoo, T., and M.W. Davidson. 34-Channel QUASAR Detection Unit. Zeiss Educ. Microsc. Digit. Imaging. .

171. Carl Zeiss. 2010. Zeiss LSM 780 Operating Manual. : 1–736.

172. Shaner, N.C., P.A. Steinbach, and R.Y. Tsien. 2005. A guide to choosing

fluorescent proteins. Nat. Methods. 2: 905–9.

173. Boukari, H., R. Nossal, and D.L. Sackett. 2003. Stability of drug-induced tubulin rings by fluorescence correlation spectroscopy. Biochemistry. 42: 1292–300.

174. Pack, C.G., G. Nishimura, M. Tamura, K. Aoki, H. Taguchi, M. Yoshida, and M. Kinjo. 1999. Analysis of interaction between chaperonin GroEL and its substrate using fluorescence correlation spectroscopy. Cytometry. 36: 247–53.

175. Altan-Bonnet, N., and G. Altan-Bonnet. 2009. Fluorescence correlation spectroscopy in living cells: A practical approach. In: Current Protocols in Cell Biology. Hoboken, NJ, USA: John Wiley & Sons, Inc. pp. 1–15.

176. García-Sáez, A.J., and P. Schwille. 2008. Fluorescence correlation spectroscopy for the study of membrane dynamics and protein/lipid interactions. Methods. 46: 116–22.

177. Kahya, N., D. Scherfeld, K. Bacia, B. Poolman, and P. Schwille. 2003. Probing Lipid Mobility of Raft-exhibiting Model Membranes by Fluorescence Correlation Spectroscopy. J. Biol. Chem. 278: 28109–28115.

178. Palmer, A.G., and N.L. Thompson. 1989. Fluorescence correlation spectroscopy for detecting submicroscopic clusters of fluorescent molecules in membranes. Chem. Phys. Lipids. 50: 253–70.

179. Koltermann, A., U. Kettling, J. Stephan, T. Winkler, and M. Eigen. 2001. Dual-Color Confocal Fluorescence Spectroscopy and its Application in Biotechnology. . pp. 187–203.

180. Rigler, R., Z. Földes-Papp, F.J. Meyer-Almes, C. Sammet, M. Völcker, and A. Schnetz. 1998. Fluorescence cross-correlation: a new concept for polymerase chain reaction. J. Biotechnol. 63: 97–109.

181. Berland, K.M. 2004. Detection of specific DNA sequences using dual-color two-photon fluorescence correlation spectroscopy. J. Biotechnol. 108: 127–36.

182. Sasaki, A., and M. Kinjo. 2010. Fluorescence Cross-Correlation Spectroscopy for Real-Time Monitoring of Exogenous DNA Behavior in Living Cells. .

183. Foo, Y.H., N. Naredi-Rainer, D.C. Lamb, S. Ahmed, and T. Wohland. 2012. Factors affecting the quantification of biomolecular interactions by fluorescence cross-correlation spectroscopy. Biophys. J. 102: 1174–83.

184. Herrick-Davis, K., E. Grinde, T. Lindsley, A. Cowan, and J.E. Mazurkiewicz. 2012. Oligomer Size of the Serotonin 5-Hydroxytryptamine 2C (5-HT2C) Receptor Revealed by Fluorescence Correlation Spectroscopy with Photon Counting Histogram Analysis: EVIDENCE FOR HOMODIMERS WITHOUT MONOMERS OR TETRAMERS. J. Biol. Chem. 287: 23604–23614.

185. Wong, K., S.J. Briddon, N.D. Holliday, and I.D. Kerr. 2016. Plasma membrane dynamics and tetrameric organisation of ABCG2 transporters in mammalian cells revealed by single particle imaging techniques. Biochim. Biophys. Acta - Mol. Cell Res. 1863: 19–29.

186. Barbeau, A., J.L. Swift, A.G. Godin, Y. De Koninck, P.W. Wiseman, and J.-M. Beaulieu. 2013. Spatial intensity distribution analysis (SpIDA): a new tool for receptor tyrosine kinase activation and transactivation quantification. Methods Cell Biol. 117: 1–19.

187. Wiseman, P.W., a. G. Godin, J.L. Swift, S. Costantino, a. Ribeiro-da-Silva, Y. De Koninck, and J. Beaulieu. 2012. Spatial intensity distribution Analysis (SpIDA): A fluorescence microscopy based method to measure receptor oligomerization in cells. Microsc. Microanal. 18: 128–129.

188. Godin, A.G., S. Costantino, L.-E. Lorenzo, J.L. Swift, M. Sergeev, A. Ribeiro-da-Silva, Y. De Koninck, and P.W. Wiseman. 2011. Revealing protein oligomerization and densities in situ using spatial intensity distribution analysis. Proc. Natl. Acad. Sci. U. S. A. 108: 7010–5.

189. Mueller, J.D., M. Tekmen, L. Hillesheim, W. Yang, and Y. Chen. 2004. Dual-Color Fluorescence Fluctuation Spectoscopy in vitro and in vivo. In: Periasamy A, PTC So, editors. SPIE. . pp. 136–145.

190. Nübling, G.S., J. Levin, B. Bader, S. Lorenzl, A. Hillmer, T. Högen, F. Kamp, and A. Giese. 2014. Modelling Ser129 phosphorylation inhibits membrane binding of pore-forming alpha-synuclein oligomers. PLoS One. 9: e98906.

191. Högen, T., J. Levin, F. Schmidt, M. Caruana, N. Vassallo, H. Kretzschmar, K. Bötzel, F. Kamp, and A. Giese. 2012. Two different binding modes of α-synuclein to lipid vesicles depending on its aggregation state. Biophys. J. 102: 1646–55.

192. Lamb, D.C. Fundamentals of Fluctuation Spectroscopy IV: Photon Counting Histogram Analysis. .

193. Malchus, N. 2011. Fluorescence correlation spectroscopy: detecting and interpreting the mobility of transmembrane proteins in vivo. Curr. Protoc. Toxicol. Chapter 2: Unit2.19.

194. Kenworthy, A.K., B.J. Nichols, C.L. Remmert, G.M. Hendrix, M. Kumar, J. Zimmerberg, and J. Lippincott-Schwartz. 2004. Dynamics of putative raft-associated proteins at the cell surface. J. Cell Biol. 165: 735–46.

195. Miyazaki, J., K. Araki, E. Yamato, H. Ikegami, T. Asano, Y. Shibasaki, Y. Oka, and K. Yamamura. 1990. Establishment of a pancreatic beta cell line that retains glucose-inducible insulin secretion: special reference to expression of glucose transporter isoforms. Endocrinology. 127: 126–32.

196. Ishihara, H., T. Asano, K. Tsukuda, H. Katagiri, K. Inukai, M. Anai, M. Kikuchi, Y. Yazaki, J.I. Miyazaki, and Y. Oka. 1993. Pancreatic beta cell line MIN6 exhibits characteristics of glucose metabolism and glucose-stimulated insulin secretion similar to those of normal islets. Diabetologia. 36: 1139–45.

197. Cheng, K., V. Delghingaro-Augusto, C.J. Nolan, N. Turner, N. Hallahan, S. Andrikopoulos, and J.E. Gunton. 2012. High Passage MIN6 Cells Have Impaired Insulin Secretion with Impaired Glucose and Lipid Oxidation. PLoS One. 7: e40868.

198. Kim, T.K., and J.H. Eberwine. 2010. Mammalian cell transfection: the present and the future. Anal. Bioanal. Chem. 397: 3173–3178.

199. Midoux, P., C. Pichon, J.-J. Yaouanc, and P.-A. Jaffrès. 2009. Chemical vectors for gene delivery: a current review on polymers, peptides and lipids containing histidine or imidazole as nucleic acids carriers. Br. J. Pharmacol. 157: 166–78.

200. Arnold, A.-S., V. Laporte, S. Dumont, A. Appert-Collin, P. Erbacher, G. Coupin, R. Levy, P. Poindron, and J.-P. Gies. 2006. Comparing reagents for efficient transfection of human primary myoblasts: FuGENE 6, Effectene and ExGen 500. Fundam. Clin. Pharmacol. 20: 81–9.

201. Mazia, D., G. Schatten, and W. Sale. 1975. Adhesion of cells to surfaces coated with polylysine. Applications to electron microscopy. J. Cell Biol. 66: 198–200.

202. Mehier-Humbert, S., and R.H. Guy. 2005. Physical methods for gene transfer: improving the kinetics of gene delivery into cells. Adv. Drug Deliv. Rev. 57: 733–53.

203. Sbalzarini, I.F., and P. Koumoutsakos. 2005. Feature point tracking and trajectory analysis for video imaging in cell biology. J. Struct. Biol. 151: 182–95.

204. Reits, E.A., and J.J. Neefjes. 2001. From fixed to FRAP: measuring protein mobility and activity in living cells. Nat. Cell Biol. 3: E145–7.

205. Weidemann, T., R. Worch, K. Kurgonaite, M. Hintersteiner, C. Bökel, and P. Schwille. 2011. Single cell analysis of ligand binding and complex formation of interleukin-4 receptor subunits. Biophys. J. 101: 2360–2369.

206. Calebiro, D., F. Rieken, J. Wagner, T. Sungkaworn, U. Zabel, A. Borzi, E. Cocucci, A. Zurn, and M.J. Lohse. 2013. Single-molecule analysis of fluorescently labeled G-protein-coupled receptors reveals complexes with distinct dynamics and organization. Proc. Natl. Acad. Sci. 110: 743–748.

207. Hartel, A.J.W., M. Glogger, G. Guigas, N.G. Jones, S.F. Fenz, M. Weiss, and M. Engstler. 2015. The molecular size of the extra-membrane domain influences the diffusion of the GPI-anchored VSG on the trypanosome plasma membrane. Sci. Rep. 5: 10394.

208. Honigmann, A., V. Mueller, H. Ta, A. Schoenle, E. Sezgin, S.W. Hell, and C. Eggeling. 2014. Scanning STED-FCS reveals spatiotemporal heterogeneity of lipid interaction in the plasma membrane of living cells. Nat. Commun. 5: 5412.

209. Weisshart, K., V. Jüngel, and S.J. Briddon. 2004. The LSM 510 META - ConfoCor 2 system: an integrated imaging and spectroscopic platform for single-molecule detection. Curr. Pharm. Biotechnol. 5: 135–54.

210. Berland, K.M., P.T. So, and E. Gratton. 1995. Two-photon fluorescence correlation spectroscopy: method and application to the intracellular environment. Biophys. J. 68: 694–701.

211. Jeanneteau, F., J. Diaz, P. Sokoloff, and N. Griffon. 2004. Interactions of GIPC with dopamine D2, D3 but not D4 receptors define a novel mode of regulation of G protein-coupled receptors. Mol. Biol. Cell. 15: 696–705.

212. Weill, C., B. Ilien, M. Goeldner, and J.L. Galzi. 1999. Fluorescent muscarinic EGFP-hM1 chimeric receptors: design, ligand binding and functional properties. J. Recept. Signal Transduct. Res. 19: 423–36.

213. Ruiz-Velasco, V., and S.R. Ikeda. 2001. Functional expression and FRET analysis of green fluorescent proteins fused to G-protein subunits in rat sympathetic neurons. J. Physiol. 537: 679–92.

214. Hynes, T.R., E. Yost, S. Mervine, and C.H. Berlot. 2008. Multicolor BiFC analysis of competition among G protein β and γ subunit interactions. Methods. 45: 207–213.

215. Ruiz-Velasco, V., and S.R. Ikeda. 2000. Multiple G-protein betagamma combinations produce voltage-dependent inhibition of N-type calcium channels in rat superior cervical ganglion neurons. J. Neurosci. 20: 2183–91.

216. Chen, Y., J.D. Müller, Q. Ruan, and E. Gratton. 2002. Molecular brightness characterization of EGFP in vivo by fluorescence fluctuation spectroscopy. Biophys. J. 82: 133–144.

217. Wu, B., Y. Chen, and J.D. Müller. 2009. Fluorescence fluctuation spectroscopy of mCherry in living cells. Biophys. J. 96: 2391–404.

218. Schenk, A., S. Ivanchenko, C. Röcker, J. Wiedenmann, and G.U. Nienhaus. 2004. Photodynamics of red fluorescent proteins studied by fluorescence correlation spectroscopy. Biophys. J. 86: 384–94.

219. Lin, W.-C., L. Iversen, H.-L. Tu, C. Rhodes, S.M. Christensen, J.S. Iwig, S.D. Hansen, W.Y.C. Huang, and J.T. Groves. 2014. H-Ras forms dimers on membrane surfaces via a protein-protein interface. Proc. Natl. Acad. Sci. U. S. A. 111: 2996–3001.

220. Karnoub, A.E., and R.A. Weinberg. 2008. Ras oncogenes: split personalities. Nat. Rev. Mol. Cell Biol. 9: 517–31.

221. Rubí, B., S. Ljubicic, S. Pournourmohammadi, S. Carobbio, M. Armanet, C. Bartley, and P. Maechler. 2005. Dopamine D2-like receptors are expressed in pancreatic beta cells and mediate inhibition of insulin secretion. J. Biol. Chem. 280: 36824–32.

222. Sadaie, W., Y. Harada, M. Matsuda, and K. Aoki. 2014. Quantitative in vivo fluorescence cross-correlation analyses highlight the importance of competitive effects in the regulation of protein-protein interactions. Mol. Cell. Biol. 34: 3272–90.

223. Comar, W.D., S.M. Schubert, B. Jastrzebska, K. Palczewski, and A.W. Smith. 2014. Time-resolved fluorescence spectroscopy measures clustering and mobility of a G protein-coupled receptor opsin in live cell membranes. J. Am. Chem. Soc. 136: 8342–9.

224. Lundius, E.G., V. Vukojevic, E. Hertz, N. Stroth, A. Cederlund, M. Hiraiwa, L. Terenius, and P. Svenningsson. 2014. GPR37 Protein trafficking to the plasma membrane regulated by prosaposin and GM1 gangliosides promotes cell viability. J. Biol. Chem. 289: 4660–4673.

225. Basit, H., S.G. Lopez, and T.E. Keyes. 2014. Fluorescence correlation and lifetime correlation spectroscopy applied to the study of supported lipid bilayer models of the cell membrane. Methods. 68: 286–299.

226. Perike, S., N. Özkucur, P. Sharma, W. Staroske, R. Bläsche, K. Barth, and R.H.W. Funk. 2014. Phospho-NHE3 forms membrane patches and interacts with beta-actin to sense and maintain constant direction during cell migration. Exp. Cell Res. 324: 13–29.

227. Thaler, C., S. V. Koushik, P.S. Blank, and S.S. Vogel. 2005. Quantitative multiphoton spectral imaging and its use for measuring resonance energy transfer. Biophys. J. 89: 2736–2749.

228. Weidemann, T., and P. Schwille. 2013. Dual-Color Fluorescence Cross-Correlation Spectroscopy with Continuous Laser Excitation in a Confocal Setup. In: Tetin SY, editor. Methods in Enzymology: Fluorescence Fluctuation Spectroscopy (FFS), Part A. New York: Elsevier. pp. 43–70.

229. Clapham, D.E., and E.J. Neer. 1993. New roles for G-protein βγ-dimers in transmembrane signalling. Nature. 365: 403–406.

230. Lei, Q., M.B. Jones, E.M. Talley, a. D. Schrier, W.E. McIntire, J.C. Garrison, and D. a. Bayliss. 2000. Activation and inhibition of G protein-coupled inwardly rectifying potassium (Kir3) channels by G protein beta gamma subunits. Proc. Natl. Acad. Sci. 97: 9771–9776.

231. Ruiz-Velasco, V., and S.R. Ikeda. 2001. Functional expression and FRET analysis of green fluorescent proteins fused to G-protein subunits in rat sympathetic neurons. J. Physiol. 537: 679–92.

232. Zimmermann, T., J. Rietdorf, and R. Pepperkok. 2003. Spectral imaging and its applications in live cell microscopy. FEBS Lett. 546: 87–92.

233. Rebois, R.V., M. Robitaille, C. Galés, D.J. Dupré, A. Baragli, P. Trieu, N. Ethier, M. Bouvier, and T.E. Hébert. 2006. Heterotrimeric G proteins form stable complexes with adenylyl cyclase and Kir3.1 channels in living cells. J. Cell Sci. 119: 2807–18.

234. Shaner, N.C., M.Z. Lin, M.R. McKeown, P.A. Steinbach, K.L. Hazelwood, M.W. Davidson, and R.Y. Tsien. 2008. Improving the photostability of bright monomeric orange and red fluorescent proteins. Nat. Methods. 5: 545–551.

235. Koltermann, a, U. Kettling, J. Bieschke, T. Winkler, and M. Eigen. 1998. Rapid assay processing by integration of dual-color fluorescence cross-correlation spectroscopy: high throughput screening for enzyme activity. Proc. Natl. Acad. Sci. U. S. A. 95: 1421–1426.

236. Chen, Y., J.D. Müller, P.T. So, and E. Gratton. 1999. The photon counting histogram in fluorescence fluctuation spectroscopy. Biophys. J. 77: 553–67.

237. Hibino, H., A. Inanobe, K. Furutani, S. Murakami, I. Findlay, and Y. Kurachi. 2010. Inwardly rectifying potassium channels: their structure, function, and physiological roles. Physiol. Rev. 90: 291–366.

238. Wang, W., M.R. Whorton, and R. MacKinnon. 2014. Quantitative analysis of mammalian GIRK2 channel regulation by G proteins, the signaling lipid PIP2 and Na+ in a reconstituted system. Elife. 3: e03671.

239. Kofuji, P., N. Davidson, and H.A. Lester. 1995. Evidence that neuronal G-protein-gated inwardly rectifying K+ channels are activated by G beta gamma subunits and function as heteromultimers. Proc. Natl. Acad. Sci. U. S. A. 92: 6542–6.

240. Lesage, F., E. Guillemare, M. Fink, F. Duprat, C. Heurteaux, M. Fosset, G. Romey, J. Barhanin, and M. Lazdunski. 1995. Molecular properties of neuronal G-protein-activated inwardly rectifying K+ channels. J. Biol. Chem. 270: 28660–7.

241. Jelacic, T.M., S.M. Sims, and D.E. Clapham. 1999. Functional expression and characterization of G-protein-gated inwardly rectifying K+ channels containing GIRK3. J. Membr. Biol. 169: 123–9.

242. Jelacic, T.M., M.E. Kennedy, K. Wickman, and D.E. Clapham. 2000. Functional and biochemical evidence for G-protein-gated inwardly rectifying K+ (GIRK) channels composed of GIRK2 and GIRK3. J. Biol. Chem. 275: 36211–6.

243. Lüscher, C., and P.A. Slesinger. 2010. Emerging roles for G protein-gated inwardly rectifying potassium (GIRK) channels in health and disease. Nat. Rev. Neurosci. 11: 301–315.

244. Nelson, C.S., J.L. Marino, and C.N. Allen. 1997. Cloning and characterization of Kir3.1 (GIRK1) C-terminal alternative splice variants. Brain Res. Mol. Brain Res. 46: 185–96.

245. Isomoto, S., C. Kondo, N. Takahashi, S. Matsumoto, M. Yamada, T. Takumi, Y. Horio, and Y. Kurachi. 1996. A novel ubiquitously distributed isoform of GIRK2 (GIRK2B) enhances GIRK1 expression of the G-protein-gated K+ current in Xenopus oocytes. Biochem. Biophys. Res. Commun. 218: 286–91.

246. Logothetis, D.E., R. Mahajan, S.K. Adney, J. Ha, T. Kawano, X.-Y. Meng, and M. Cui. 2015. Unifying Mechanism of Controlling Kir3 Channel Activity by G Proteins and Phosphoinositides. In: International Review of Neurobiology. Elsevier Inc. pp. 1–26.

247. de Velasco, E.M.F., N. McCall, and K. Wickman. 2015. GIRK Channel Plasticity and Implications for Drug Addiction. In: Structure to Function of G protein-gated inwardly rectifying (GIRK) Channels. Elsevier Inc. pp. 201–238.

248. Nagi, K., and G. Pineyro. 2014. Kir3 channel signaling complexes: focus on opioid receptor signaling. Front. Cell. Neurosci. 8: 186.

249. Wang, X., B. Liang, L. Skibsbye, S.-P. Olesen, M. Grunnet, and T. Jespersen.

2013. GIRK channel activation via adenosine or muscarinic receptors has similar effects on rat atrial electrophysiology. J. Cardiovasc. Pharmacol. 62: 192–8.

250. Pillai, G., N.A. Brown, G. McAllister, G. Milligan, and G.R. Seabrook. 1998. Human D2 and D4 dopamine receptors couple through betagamma G-protein subunits to inwardly rectifying K+ channels (GIRK1) in a Xenopus oocyte expression system: selective antagonism by L-741,626 and L-745,870 respectively. Neuropharmacology. 37: 983–987.

251. Jaén, C., and C. a Doupnik. 2005. Neuronal Kir3.1/Kir3.2a channels coupled to serotonin 1A and muscarinic m2 receptors are differentially modulated by the “short” RGS3 isoform. Neuropharmacology. 49: 465–76.

252. Kreienkamp, H.J., H.H. Hönck, and D. Richter. 1997. Coupling of rat somatostatin receptor subtypes to a G-protein gated inwardly rectifying potassium channel (GIRK1). FEBS Lett. 419: 92–4.

253. Iwanir, S., and E. Reuveny. 2008. Adrenaline-induced hyperpolarization of mouse pancreatic islet cells is mediated by G protein-gated inwardly rectifying potassium (GIRK) channels. Pflugers Arch. 456: 1097–108.

254. Bond, C.T., C. Ammälä, R. Ashfield, T.A. Blair, F. Gribble, R.N. Khan, K. Lee, P. Proks, I.C. Rowe, and H. Sakura. 1995. Cloning and functional expression of the cDNA encoding an inwardly-rectifying potassium channel expressed in pancreatic beta-cells and in the brain. FEBS Lett. 367: 61–6.

255. Stoffel, M., Y. Tokuyama, J.B. Trabb, M.S. German, M.L. Tsaar, L.Y. Jan, K.S. Polonsky, and G.I. Bell. 1995. Cloning of rat KATP-2 channel and decreased expression in pancreatic islets of male Zucker diabetic fatty rats. Biochem. Biophys. Res. Commun. 212: 894–9.

256. Tsaur, M.L., S. Menzel, F.P. Lai, R. Espinosa, P. Concannon, R.S. Spielman, C.L. Hanis, N.J. Cox, M.M. Le Beau, and M.S. German. 1995. Isolation of a cDNA clone encoding a KATP channel-like protein expressed in insulin-secreting cells, localization of the human gene to chromosome band 21q22.1, and linkage studies with NIDDM. Diabetes. 44: 592–6.

257. Zhao, Y., Q. Fang, S.G. Straub, and G.W.G. Sharp. 2008. Both Gi and Go heterotrimeric G proteins are required to exert the full effect of norepinephrine on the beta-cell K ATP channel. J. Biol. Chem. 283: 5306–16.

258. Ferrer, J., C.G. Nichols, E.N. Makhina, L. Salkoff, J. Bernstein, D. Gerhard, J. Wasson, S. Ramanadham, and A. Permutt. 1995. Pancreatic islet cells express a family of inwardly rectifying K+ channel subunits which interact to form G-protein-activated channels. J. Biol. Chem. 270: 26086–91.

259. Mirshahi, T., and D.E. Logothetis. 2004. Molecular determinants responsible for differential cellular distribution of G protein-gated inwardly rectifying K+ channels. J. Biol. Chem. 279: 11890–7.

260. Peng, L., T. Mirshahi, H. Zhang, J.P. Hirsch, and D.E. Logothetis. 2003. Critical determinants of the G protein gamma subunits in the Gbetagamma stimulation of G protein-activated inwardly rectifying potassium (GIRK) channel activity. J. Biol. Chem. 278: 50203–11.

261. Mirshahi, T., V. Mittal, H. Zhang, M.E. Linder, and D.E. Logothetis. 2002. Distinct sites on G protein beta gamma subunits regulate different effector functions. J. Biol. Chem. 277: 36345–50.

262. Wickman, K., J. Nemec, S.J. Gendler, and D.E. Clapham. 1998. Abnormal Heart Rate Regulation in GIRK4 Knockout Mice. Neuron. 20: 103–114.

263. Krapivinsky, G., M.E. Kennedy, J. Nemec, I. Medina, L. Krapivinsky, and D.E. Clapham. 1998. Gbeta-gamma binding to GIRK4 subunit is critical for G protein-gated K+ channel activation. J. Biol. Chem. 273: 16946–16952.

264. Mirshahi, T., D.E. Logothetis, and M. Sassaroli. 2001. Localization and Quantification of GFP-Tagged Ion Channels Expressed in Xenopus Oocytes. In: Ion Channel Localization. New Jersey: Humana Press. pp. 215–232.

265. Kuzhikandathil, E. V, and G.S. Oxford. 2000. Dominant-negative mutants identify a role for GIRK channels in D3 dopamine receptor-mediated regulation of spontaneous secretory activity. J. Gen. Physiol. 115: 697–706.

266. Kuzhikandathil, E. V, W. Yu, and G.S. Oxford. 1998. Human dopamine D3 and D2L receptors couple to inward rectifier potassium channels in mammalian cell lines. Mol. Cell. Neurosci. 12: 390–402.

267. Ostrom, R.S. 2002. New determinants of receptor-effector coupling: trafficking and compartmentation in membrane microdomains. Mol. Pharmacol. 61: 473–6.

268. Marinissen, M.J., and J.S. Gutkind. 2001. G-protein-coupled receptors and signaling networks: emerging paradigms. Trends Pharmacol. Sci. 22: 368–76.

269. Wischmeyer, E., F. Döring, E. Wischmeyer, A. Spauschus, A. Thomzig, R. Veh, and A. Karschin. 1997. Subunit interactions in the assembly of neuronal Kir3.0 inwardly rectifying K+ channels. Mol. Cell. Neurosci. 9: 194–206.

270. Ma, D., N. Zerangue, K. Raab-Graham, S.R. Fried, Y.N. Jan, and L.Y. Jan. 2002. Diverse trafficking patterns due to multiple traffic motifs in G protein-activated inwardly rectifying potassium channels from brain and heart. Neuron. 33: 715–29.

271. Lunn, M.-L., R. Nassirpour, C. Arrabit, J. Tan, I. McLeod, C.M. Arias, P.E. Sawchenko, J.R. Yates, and P. a Slesinger. 2007. A unique sorting nexin regulates trafficking of potassium channels via a PDZ domain interaction. Nat. Neurosci. 10: 1249–59.

272. Kilpatrick, L.E., S.J. Briddon, and N.D. Holliday. 2012. Fluorescence correlation spectroscopy, combined with bimolecular fluorescence complementation, reveals the effects of β-arrestin complexes and endocytic targeting on the membrane mobility of neuropeptide Y receptors. Biochim. Biophys. Acta. 1823: 1068–81.

273. Westrich, L., and E. V Kuzhikandathil. 2007. The tolerance property of human D3 dopamine receptor is determined by specific amino acid residues in the second cytoplasmic loop. Biochim. Biophys. Acta. 1773: 1747–58.

274. Yatani, A., J. Codina, Y. Imoto, J.P. Reeves, L. Birnbaumer, and A.M. Brown. 1987. A G protein directly regulates mammalian cardiac calcium channels. Science. 238: 1288–92.